

C | A | U

Kiel University
Christian-Albrechts-Universität zu Kiel

Faculty of Engineering

Wireless Communications
Kiel University
Prof. Dr.-Ing. Dirk Manteuffel

Modal analysis methods for small antenna design

Eugen Safin

Volume 2



1. Gutachter Prof. Dr.-Ing. Dirk Manteuffel
2. Gutachter Prof. Dr.-Ing. Pavel Hazdra
3. Gutachter Prof. Dr.-Ing. Gerhard Schmidt
4. Gutachter Prof. Dr.-Ing. Ludger Klinkenbusch
5. Gutachter Prof. Dr.-Ing. Michael Höft

Datum der mündlichen Prüfung: 15.12.2016

Modal analysis methods for small antenna design

Dissertation

zur Erlangung des akademischen Grades Doktor der Ingenieurwissenschaften
(Dr.-Ing.) der Technischen Fakultät der Christian Albrechts-Universität zu
Kiel

Eugen Safin

Kiel

17.03.2016

Hiermit versichere ich, dass ich die Doktorarbeit

Modal Analysis Methods for Small Antenna Design

selbständig und ohne unzulässige fremde Hilfe angefertigt habe und dass ich alle von anderen Autoren wörtlich übernommenen Stellen, wie auch die sich an die Gedankengänge anderer Autoren eng anlehnenden Ausführungen meiner Arbeit, besonders gekennzeichnet und die entsprechenden Quellen angegeben habe. Weiterhin wurde die Arbeit ausschließlich der Christian-Albrechts-Universität zu Kiel im Rahmen eines Prüfungsverfahrens vorgelegt, jedoch wurden Teile in Form von Beiträgen in Fachzeitschriften und Tagungsbänden veröffentlicht bzw. zur Veröffentlichung eingereicht (siehe Abschnitt zu Publikationen). Diese Arbeit ist unter Einhaltung der Regeln guter wissenschaftlicher Praxis der Deutschen Forschungsgemeinschaft entstanden.

Eugen Safin

Abstract

The Theory of Characteristic Modes (TCM) has proved itself well in antenna design even in the recent years. A large number of applications has been presented by other authors, in which the TCM has been utilized. In this dissertation, the common theory is extended with new numerical techniques suitable for the design of small antennas. Eigenvalue tracking as a fundamental numerical problem, which arises from the early mode analysis, is discussed. The degenerated mode effect is presented and an explanation is given as to where it comes from and how it affects the tracking concept. A new algorithm is presented to generate differential eigenvalue curves and to compensate for the degenerated mode effect.

The modal source reconstruction is an additional technique, which is used to predict the mode contribution from a simplified structure. This technique allows utilization of the TCM with other not Method of Moments based solver under the assumption that the simplified structures carries almost the same chassis modes as the real structure. Furthermore, the lumped impedance matching networks are treated in the mode analysis. The influence of such lumped networks on the characteristic modes is investigated and the modal efficiency is defined. The definition of the modal admittances and impedances are given and evaluated for inductive and capacitive coupling elements. Equivalent circuit models are presented and evaluated for these types of coupling elements for generic examples.

The problem of a useful interpretation of the dielectric modes and their eigenvalue are discussed and evaluated for dielectric resonator antennas (DRAs). Conditions are given where the eigenvalue of the dielectric modes determines the natural resonance of modes. A cylindrical DRA is used to validate the proposed interpretation of modes. Finally, the combined mode excitation concept is presented and evaluated for small terminals. This concept is used as a basis to integrate antennas into a hand held device. The experiences are used to develop the proposed concept further and to integrate the antennas into the rear-view mirror of a vehicle.

Zusammenfassung

Die Antennenentwicklung auf Basis der Theorie der Charakteristischen Moden (TCM) hat sich vor allem in den letzten Jahren rasant weiterentwickelt. Das Konzept der modalen Zerlegung hat sich bereits für eine Vielzahl von Anwendungen bewehrt. In dem Hauptfokus dieser Dissertation ist die theoretische und numerische Erweiterung der Theorie, welche für die Entwicklung von kleinen Antennen besonders geeignet sind. Das Problem der Eigenwertverfolgung ist ein seit langem bekanntes Problem, welches bis heute nicht ausreichend gelöst ist. Das Problem der entarteten Moden wird präsentiert und es wird ausführlich erklärt, woher das Problem kommt und wie dieser die Verfolgung der Moden beeinflusst. Aufbauend auf diese Voruntersuchung wird ein neues Verfahren präsentiert, welches das Problem der entarteten Moden kompensiert und die Verfolgung der Eigenwerte entscheiden verbessert.

Die Vorhersage der modalen Stromverteilung auf Basis des modalen Fernfeldes ist eine neue Methode, um nicht Momenten basierte Solver in die TCM einzubeziehen. Dieses Konzept basiert auf der Annahme, dass eine vereinfachte Struktur die gleichen Moden unterstützt, wie das komplexere Model, mit allen darin enthaltenen Details. Weiterhin werden konzentrierte Anpassnetzwerke in die Modenberechnung einbezogen, um so den Einfluss der reaktiven Komponenten zu beurteilen. Die modale Effizienz wird eingeführt, für den Fall, dass verlustbehaftete Elemente im Netzwerk enthalten sind. Dieses wird für einige ausgewählte Beispiele validiert. Darauffolgend wird die modale Admittanz und Impedanz eingeführt, diskutiert und angewendet auf die

so genannten induktiven und kapazitiven Koppelemente. Äquivalente Ersatzschaltungen werden entwickelt und für einige in der Antennentechnik übliche Beispiele validiert.

Das Problem der sinnvollen Interpretation der dielektrischen Moden wird aufgegriffen und diskutiert. Es werden Bedingungen genannt, wann eine sinnvolle Interpretation der Mode möglich ist. Dies wird am Beispiel einer zylindrischen dielektrischen Resonator-Antenne erläutert und es werden die natürlichen Resonanzen der Moden mit der in der Fachliteratur bekannten zylindrischen Moden verglichen. Abschließend wird ein neues Konzept der kombinierten Anregung der Moden präsentiert und speziell für die Antennenintegration in kleine mobile Plattformen diskutiert. Dieses Konzept wird für ein kleines mobiles Endgerät aufgebaut und messtechnisch verifiziert. Aufbauend auf dieser Antennenentwicklung wird das hier präsentierte Konzept weiterentwickelt und es werden mehrere Antennen in einem Innenspiegel eines Autos integriert.

Danksagung

Die vorliegende Arbeit entstand während meiner Tätigkeit als wissenschaftlicher Mitarbeiter in der Arbeitsgruppe für Funkkommunikation der Christian-Albrechts-Universität zu Kiel.

An dieser Stelle möchte ich mich ganz besonders bei Herrn Prof. Dr.-Ing. Dirk Manteuffel bedanken, der mir die Möglichkeit gegeben hat, in dem spannenden Feld der numerischen Antennenberechnung zu forschen und zu promovieren. Ich bin dankbar für die viele Diskussionen, den fachlichen Rat und die Freiheit in der Ausgestaltung der Forschungsschwerpunkte.

Ein großes Dankeschön geht an die gesamte Arbeitsgruppe Funkkommunikation für die gute Zusammenarbeit. Ganz besonders möchte ich mich bei meinen Kollegen Robert Ledig (geb. Martens), Markus Grimm, D.Sc. (Tech.) Risto Valkonen, Yi Chen, Florian Marx und Thade Wunderlich (geb. Hademik) für die gemeinsame Zeit bedanken. Hierbei seien besonders die fachlichen Diskussionen hervorzuheben, die zum Gelingen dieser Arbeit beigetragen haben.

Darüber hinaus möchte ich mich bei meinen Freunden und meiner Familie für die offenen Ohren und den Rat in allen Lebenslagen bedanken.

Content

List of Author's Publications and Contributions.....	I
List of Abbreviations	XIII
1 Introduction.....	1
1.1 Background.....	1
1.2 Objective of this work	3
1.3 Content and Organization of the thesis.....	3
2 Surface Integral Equation.....	7
2.1 Electric Field Integral Equation (EFIE).....	8
2.2 Magnetic Field Integral Equation (MFIE).....	10
3 Method of Moments.....	13
3.1 The RWG Basis Function.....	14
3.2 Testing Procedure	15
3.3 PHMCTW Formulation for Dielectric and Magnetic Bodies.....	17
3.4 Efficient Numerical Evaluation of the Integral Equations.....	20
4 The Theory of Characteristic Modes	23
4.1 The Generalized Eigenvalue Problem for PEC Modes	25
4.2 On the Property of the Characteristic Modes	26
4.3 The Generalized Eigenvalue Problem for Dielectric and Magnetic Modes	29
4.4 Characteristic Mode Computation.....	30
4.5 Characteristic Basis Function (CBF).....	31

4.6	Examples.....	32
4.6.1	Dipole	33
4.6.2	Rectangular Plate	34
5	Eigenvalue Tracking	39
5.1	Definition of the Tracking Problem.....	40
5.2	Correlation Based Eigenvalue Tracking	41
5.2.1	Eigenvector Correlation.....	44
5.2.2	Far Field Correlation.....	45
5.2.3	Surface Current Correlation.....	45
5.3	Correlation-Based Eigenvalue Tracking – Example.....	47
5.4	Degenerated Modes	50
5.5	Orthogonalization-Based Eigenvalue Tracking	54
5.6	Orthogonalization-Based Eigenvalue Tracking – Example.....	57
5.6.1	Rectangular Plate	58
5.6.2	Fractal Antenna over an Infinite Size Ground Plane	59
6	Source Reconstruction	61
6.1	Far Field Calculation	62
6.2	Correlation of the Characteristic Modes	63
6.3	Reconstruction of the Modal Sources	64
6.3.1	Scalar Method.....	65
6.3.2	Matrix Method.....	67
6.4	Examples.....	68
6.4.1	Plane Wave	70
6.4.2	iPhone 4	71
7	Characteristic Admittance and Impedance	75
7.1	Characteristic Admittance.....	76
7.2	Approximation of the Remaining Admittance with an Ideal Transmission Line	79
7.2.1	Capacitive Coupling Elements (CCE)	80

7.2.2	Inductive Coupling Elements (ICE)	84
7.3	Approximation of the Loaded Remaining Admittance.....	86
7.3.1	Loaded Capacitive Coupling Element	87
7.3.2	Loaded Inductive Coupling Element.....	88
7.4	Characteristic Impedance	89
7.5	Manipulation of the Characteristic Impedance with Reactive Elements	91
8 Reactive Loading in the TCM.....		95
8.1	Resonance Manipulation due to Reactance Distribution.....	96
8.2	Eigenvalue Manipulation by Reactive Loading	101
8.2.1	Combined Excitation of Modes to Increase the Impedance Bandwidth of an Antenna.....	101
8.2.2	Selective Excitation of Modes by Decoupled Antenna Ports	104
8.3	Impedance Matching Network	109
8.4	Modal Efficiency	111
8.5	Example.....	113
9 Characteristic Modes for Dielectric Bodies.....		119
9.1	Dielectric Characteristic Modes Computation.....	119
9.2	Problem of the Physical Interpretation of the Eigenvalue	121
9.3	Validation of the Dielectric Characteristic Modes with DRA.....	124
9.4	Influence of a Plastic Chassis on the Characteristic Modes of a Handheld Device.	128
10 Application on the TCM.....		131
10.1	2-Port Antenna Concept for Small Terminal.....	132
10.2	2-Port Antenna Concept for Automotive Application.....	138
11 Conclusion		141
Appendix A.....		143
A1	Integral Equation	143

Appendix B	149
B1 Barycentric Subdivision.....	149
B2 Singularity Extraction.....	151
B3 Analytic Integration over the Singularity	153
Appendix C	159
C1 Matrix Calculation for the EFIE	159
C2 Matrix Calculation for the MFIE	161
C3 Excitation Vector Calculation for the EFIE and MFIE	163
Bibliography	165

List of Author's Publications and Contributions

The dissertation contains textual materials and figures from the below listed author's publications. The relevant publications are criticized in the text and in the caption of the respective figures. The use of those materials requires the permission of *IEEE*.

- I. **E. Safin, R. Martens, and D. Manteuffel, "Modal Source Reconstruction Based on Radiated Far-Field for Antenna Design," *Antennas and Propagation (EUCAP), Proceedings of the 6th European Conference on, Prague, Czech Republic, pp. 1645-1649, 26-30 March 2012.***

The author was responsible of developing the idea, the calculation of the characteristic modes and content of the paper. Mr. Martens and Prof. Manteuffel supervised the work.

- II. **E. Safin and D. Manteuffel, "Resonance Behavior of Characteristic Modes Due to the Presence of Dielectric Objects," *Antennas and Propagation (EUCAP), Proceedings of the 7th European Conference on, Gothenburg, Sweden, 8-11 April 2013.***

The author was responsible of developing the idea, the numerical evaluation and content of the paper. Prof. Manteuffel supervised the work.

- III. E. Safin and D. Manteuffel, "Reconstruction of Characteristic Modes an Antenna Based on the Radiated Far Field," *Antennas and Propagation, IEEE Transaction on*, Volume 61, Issue 6, pp. 2964-2971, June 2013.**

The author derived the idea and he was responsible for the numerical evaluation of the proposed method for complex structures. Prof. Manteuffel supervised the work.

- IV. E. Safin, R. Martens, M. Capek, J. Eichler, P. Hazdra, and D. Manteuffel, "Discussion and Evaluation of Modal and Radiation Q-Factors for MIMO Antennas Based on Theory of Characteristic Modes," *COST IC 1102, 3. WG Meeting & Technical Workshop 2012, Thessaloniki, June 2013.***

The author and Mr. Martens initiated the STSM (Short Term Scientific Mission) with the University of Prague. This research has been supported by Prof. Manteuffel and Prof. Hazdra. Mr. Safin and Mr. Capek calculated the modal Q-factor with two different equations and described the impact on the Theory of Characteristic Modes. The calculation of the characteristic modes has been executed by Mr. Safin and Mr. Capek. Mr. Eichler was responsible for the mesh generation of generic structures. Mr. Martens supported this work with his knowledge of the selective characteristic mode excitation.

- V. E. Safin and D. Manteuffel, "Influence of the Impedance Matching on the Characteristic Wave Modes," *Antennas and Propagation (EUCAP), Proceedings of the 8th European Conference on, The***

Hague, Netherlands, pp. 1323-1327, 6-11 April, 2014.

The author was responsible of developing the idea, the calculation of the characteristic modes, the optimization and content of the paper. Prof. Manteuffel supervised the work.

- VI. E. Safin and D. Manteuffel, "Manipulation of Characteristic Wave Modes by Impedance Loading," *Antennas and Propagation, IEEE Transaction on*, Volume 63, Issue 4, pp. 1756-1764, April 2015.**

The author derived the idea from V and developed a new optimization method for the Theory of Characteristic Modes. Prof. Manteuffel supervised the work.

- VII. E. Safin, R. Valkonen, and D. Manteuffel, "Reconfigurable LTE MIMO Automotive Antenna System Based on the Characteristic Mode Analysis," *Antennas and Propagation (EUCAP), Proceedings of the 9th European Conference on*, Lisbon, Portugal, 12-17 April, 2015.**

The author developed the antenna concept and evaluated the performance with the Theory of Characteristic Modes. Mr. Valkonen was helping in the design of the reconfigurable impedance matching network and the verification. Prof. Manteuffel supervised the work.

- VIII. E. Safin and D. Manteuffel, "Advanced Eigenvalue Tracking," *Antennas and Propagation, IEEE Transaction on*, Volume 64, Issue 7, pp. 2628-2636, July 2016.**

The author derived the idea from V and developed a new optimi-

zation method for the Theory of Characteristic Modes. Prof. Manteuffel supervised the work.

In addition, other related publications authored or co-authored by the author of this thesis are given in the reference list as [Mar11a, Mar11b and Mar11c].

Notation Remarks

Through the paper a clear notation is used to clarify the usage of the equations to the reader. All scalar values are denoted with italic letters. The vectors and matrixes are denoted with bold and capital letters. Any italic subscript letter denotes a count index which is typically used within a summation. The regular subscript is used to specify the quantity.

The entire work assumes a time harmonic dependence of the form $e^{j\omega t}$ for the electromagnetic fields and the surface currents. The integral equations are treated in frequency domain only.

List of Constants

ϵ_0	$8.8541878176 \times 10^{-12}$ [As/Vm]
μ_0	$4\pi \times 10^{-7}$ [Vs/Am]
π	3.14159265 [1]
Z_{F0}	376.730 [Ω]

List of Latin Symbols

$A_{m,n}^{\pm}$	Area of a Plus and Minus Triangle of the m-th/n-th Edge Element [m ²]
A	Area of a triangular patch [m ²]
A_i	Area of a sub-triangle [m ²]
\mathbf{A}	Vector Potential [Vs/m]
a_n	Weighting of the Characteristic Modes [$A\sqrt{\Omega}$]
b_n	Normalized Weighting of the Characteristic Modes [1]
C_i	Capacitance over the i -th Edge Element [F]
d	Distance [m]
$\mathbf{E}_{\alpha,\beta}$	Electric Field of an Arbitrary Source (α or β) [V/m]
\mathbf{E}_{inc}	Incoming Electric Field [V/m]
\mathbf{E}_n	Modal Far Field [$\sqrt{\Omega}$ /m]
\mathbf{E}_S	Scattering Electric Field [V/m]
$\mathbf{E}_{\text{total}}$	Total Far Field [V/m]
f	Frequency [Hz]
\mathbf{f}_{RWG}	RWG Basis Function [1]
G	Green's Function [1/m]

\mathbf{H}_{inc}	Incoming Magnetic Field [A/m]
\mathbf{H}_S	Scattering Magnetic Field [A/m]
I_m [A/m]	Surface Current at a Specific Position (m -th Edge Element)
I_n	Modal Surface Current at a Specific Position [$1/m\sqrt{\Omega}$]
\mathbf{I}	Current Vector [A/m]
\mathbf{I}_e	Electric Current Vector [A/m]
\mathbf{I}_m	Magnetic Current Vector [V/m]
\mathbf{J}	Electric Surface Current [A/m]
\mathbf{J}_n	Electric Characteristic Modes [$1/m\sqrt{\Omega}$]
k_0	Scalar Wave Number of the Free Space [1/m]
k_i	Scalar Wave Number of the i -th Medium [1/m]
\mathbf{K}_i	K -operator of the i -th Medium [m^2]
l	Length [m]
$l_{m,n}$	Edge Length of the m -th/ n -th RWG Basis Function [m]
L	Length of the CCE and ICE [m]
L_i	Inductance over the i -th Edge Element [H]
\mathbf{L}	Impedance Matrix Operator [Ωm]
\mathbf{M}	Magnetic Surface Current [V/m]
\mathbf{M}_n	Magnetic Characteristic Mode [$1/m\sqrt{\Omega}$]
P	Power [W]

P_{rad}	Radiated Power in Free Space [W]
P_{react}	Reactive Power [W]
P_n	Power of the n -th Characteristic Mode [1]
\mathbf{r}	Observation Point [m]
\mathbf{r}'	Source Point [m]
\mathbf{R}	Real Part of the Impedance Matrix [Ωm^2]
S	Surface [m]
\mathbf{T}	System Matrix for Dielectric and Magnetic Bodies [Ωm^2]
\mathbf{V}	Excitation Vector [Vm]
\mathbf{V}_e	Electric Excitation Vector [Vm]
\mathbf{V}_{CBF}	Excitation Vector of the CBF [$\text{A}\sqrt{\Omega}$]
\mathbf{V}_m	Magnetic Excitation Vector [Am]
V_n	Entry of the Excitation Vector \mathbf{V} [Vm]
\mathbf{W}_n	n -th Characteristic Mode for Dielectric Bodies [$1/\text{m}\sqrt{\Omega}$]
\mathbf{X}	Imaginary Part of the Impedance Matrix [Ωm^2]
Y_{in}	Input Admittance [S]
Y_{Rest}	Remaining Admittance [S]
Y_n	Modal Admittance [S]
\mathbf{Y}_i	Admittance Matrix of the i -th Medium [Sm^2]
Z_0	Reference Impedance of a Transmission Line [Ω]
Z_{in}	Input Impedance [Ω]

Z_{Rest}	Remaining Impedance [Ω]
Z_n	Modal Impedance [Ω]
\mathbf{Z}	Impedance Matrix [Ωm^2]
\mathbf{Z}_{CBF}	Impedance Matrix of the CBF [1]
$Z_{n,m}$	Entry of the Impedance Matrix \mathbf{Z} [Ωm^2]

List of Greek Symbols

α_{CFIE}	Weighting Constant for the CFIE
δ	Kroneker-Delta Function [1]
ϵ_0	Permittivity of the Free Space [As/Vm]
ϵ_i	Complex Permittivity if the i -th Medium [As/Vm]
ϵ_r	Relative Permittivity [1]
λ_n	Eigenvalue [1]
μ_0	Permeability of the Free Space [Vs/Am]
μ_i	Complex Permeability of the i -th Medium [Vs/Am]
μ_r	Relative Permeability [1]
$\rho_{\alpha,\beta}$	Complex Envelope Correlation Between Two Ports (α and β) [1]
$\rho_{\text{RWG},m}$	Charge Density of the m -th RWG Basis Function [1/sm]
$\rho_{m,n}^{\pm}$	Rho Plus and Minus Vector of the m -th/ n -th RWG Basis Function [m]
σ_i	Electric Conductivity of the i -th Medium [S/m]
$\sigma_{m,i}$	Magnetic Conductivity of the i -th Medium [Ω /m]
ϕ	Scalar Potential [V]

ω	Angular Frequency [1/s]
Ω	Solid Angle in the MFIE [1]

List of Mathematic Operations

$\mathbf{r} \cdot \mathbf{r}$	Scalar Multiplication between two Vectors
$\mathbf{r} \times \mathbf{r}$	Cross Product of two Vertexes in 3D Space
$ \mathbf{r} $	Norm of a Vector
$\mathbf{A} \cdot \mathbf{r}$	Matrix Multiplication with a Vector
\mathbf{A}^{-1}	Matrix Inversion
∇A	Gradient of a Scalar Function A
$\nabla \cdot \mathbf{A}$	Divergence of a Vector Function \mathbf{A}
$\nabla \times \mathbf{A}$	Curl Operator of a Vector Function \mathbf{A}
$\langle \mathbf{A}^*, \mathbf{B} \rangle$	Testing of the Complex Vector Function \mathbf{B} with \mathbf{A}
$\{\mathbf{A}, \mathbf{B}\}$	Envelope Correlation between the Far Field \mathbf{A} and \mathbf{B}
\mathbf{A}^T	Transpose of a Vector or Matrix
\mathbf{A}^H	Hermitian of a Vector of Matrix

List of Abbreviations

CBF	Characteristic Basis Function
CCE	Capacitive Coupling Element
CPU	Central Processor Unit
DRA	Dielectric Resonator Antenna
EFIE	Electric Field Integral Equation
FDTD	Finite Difference Time Domain
IEEE	Institute of Electrical and Electronics Engineers
IFA	Inverted 'F'-Antenna
LTE	Long Term Evolution
MIMO	Multiple-Input-Multiple-Out
MFIE	Magnetic Field Integral Equation
MoM	Method of Moments
PEC	Perfectly Electric Conductor
PCB	Printed Circuit Board
PD	Power Divider
PMCHWT	Poggio-Miller-Chan-Harrington-Wu-Tsai Formulation
PS	Phase Shifter

RWG	Rao-Wilton-Glisson Basis Function
SIE	Surface Integral Equation
SMD	Surface Mounted Device
SVD	Singular Value Decomposition
TCM	Theory of Characteristic Modes
UWB	Ultra-Wide-Band Antenna
VIE	Volume Integral Equation

Chapter 1

Introduction

1.1 Background

The small antenna design (e.g. mobile phones) and the automotive antenna integration (e.g. antennas in vehicles) are the focus of current research projects. The demands of consumer industries for more compact antennas which are able to operate in a large number of operation frequency bands, have increased in recent years. Under these circumstances, antenna design becomes more and more difficult, since the user prefers a well-shaped device with a non-visible antenna. In addition, the high data rates of mobile communications need to serve, e.g. LTE (Long Term Evolution), LTE-Advanced or the IEEE 802.11 Standard. These standards include use of more than one antenna for communications between the mobile device and the base station. The so-called MIMO (Multiple-Input-Multiple-Output) antenna design concept shows promising approaches to serve these needs for the consumer industry.

The demands and the restrictions affect the realization of a MIMO system due to the physical size and shape of the chassis [Gca08, Shu13, Zha13, Mie13].

1. Introduction

The most critical point in the integration of a MIMO system into a small volume is the electromagnetic coupling between the antennas. A reduction in the electromagnetic coupling (i.e. mutual coupling) is a key aspect in the antenna design for MIMO. Initial investigations into this phenomenon [Man01, Vai02] show that the metallic chassis is an important radiator. The understanding of the underlying radiation mechanism is required to enable optimization of the antenna system. Therefore, the shape and size of the chassis are important parameters and have to be taken into account for the MIMO antenna design. A basic concept to reduce the mutual coupling has been presented in e.g. [Kar04]. The author inserts a slit into the chassis to reduce the mutual coupling between two feeding ports. This concept is far from practical realization, as the entire space on the chassis is required for other phone components. A slit or other large modifications of the chassis are unacceptable for the final prototype and, hence, the industrial fabrication.

Since the last decade the Theory of Characteristic Modes (TCM) has been proved well in MIMO antenna design, as already demonstrated in certain publications [Max10, Mar11a, Mar11b, Mar12, Kre12, Had15]. The antenna design with the TCM exploits the chassis wave modes, which can exist in principle. These chassis wave modes can be excited either selectively, or in combination with a set of coupling elements. The selective excitation concept leads to a reduction in the mutual coupling effect on a small handheld device [Mar14]. Based on this idea, certain applications can be found in literature. These applications are motivated by the fundamental theory which shows advantages compared with common mode decomposition methods, e.g. Multipole Expansion [Bla07] or analytic expansion method with the Bessel Function of the first kind [Jam89, Bal89, Bal05].

1.2 Objective of this work

In this thesis, the TCM is extended with new concepts suitable for small antenna design. The concepts presented in this work can aid understanding of the radiation mechanism of a given antenna system and optimize the performance to a certain degree. Furthermore, this work discusses the numerical evaluation of the TCM. The different numerical techniques are discussed and evaluated for generic examples. New modal parameters are introduced, which are suitable to quantify the performance of an antenna system.

The main scientific merits of this thesis are:

- Numerical evaluation of the Method of Moments impedance matrix with different techniques.
- Characteristic Mode computation with available program libraries.
- Source reconstruction to enable the use of other numerical methods (e.g. FDTD) for the TCM.
- Advanced eigenvalue tracking over a wide frequency range.
- Characteristic Modes under the influence of an impedance matching network.
- Decomposition of the input admittance impedance with modal admittances and impedances.
- Discussion of the dielectric Characteristic Mode Theory for antenna design.
- Application of the TCM to the combined mode excitation.

1.3 Content and Organization of the thesis

In this thesis, new methods and concepts of the Theory of Characteristic Modes

1. Introduction

are presented for small antenna design. The numerical techniques and the theoretical investigations are the main focus of this work. The main scientific contribution is based on the publications [I - VIII]. The thesis summarizes the content of the author's publications.

Chapters 2,3 and 4 review the basic equations and techniques required for this thesis. In Chapter 2, the basic surface integral equations are explained, with their advantages and disadvantages. In Chapter 3, the Method of Moments and the RWG basis function are explained in brief. Hereinafter, the basic theory of the characteristic modes is summarized, as it is required for the fundamental understanding of this work.

Chapter 5 explains the problem to track the eigenvalues over a wide frequency range. The available tracking algorithms are reviewed and their limitations are discussed. The problem to track the degenerated modes is investigated and a new method is presented to improve the tracking of modes with crossing eigenvalue curves. This method is published in [VIII].

In Chapter 6, the reconstruction of the modal sources is presented, which allows for the mode analysis with other not Method of Moment based EM software. The envelope correlation is used as a measurement to determine the mode contribution on a simplified structure. This concept is discussed and evaluated for the popular iPhone4 to demonstrate the capability. This numerical technique has been published earlier in [I and III].

In Chapter 7, the modal admittance and impedance decomposition technique is presented, which provide an explanation of how the impedance matching can be understood with the Theory of Characteristic Modes. A simplified equivalent circuit model is given to represent the admittance and impedance

that remain from the modal decomposition. The inductive and capacitive coupling elements are used to validate the decomposition method and the equivalent circuit model for generic examples.

Chapter 8 treats the lumped lossy impedance matching networks and their influence on the characteristic modes. The impedance matching network is included into the characteristic mode computation and the modified eigenvalues are calculated and compared with the initial system. The modal efficiency is defined if lossy components are included within the network. These results are published in [II].

In Chapter 9, the dielectric modes are investigated. The problem of the useful interpretation of the eigenvalues is discussed, and the conditions are presented wherein the eigenvalues indicate the natural resonance of the dielectric modes. Furthermore, the dielectric modes are compared with dielectric resonator antenna modes, which are available in literature. Similarities are discussed and the resonance frequencies are compared.

The application of the Theory of Characteristic Modes is in focus of Chapter 10. The combined mode excitation is developed for a small antenna terminal. A 2-port MIMO system is evaluated, fabricated and tested for a mobile terminal chassis. This antenna concept is developed further for the antenna integration into a rearview mirror of a vehicle. Finally, a conclusion is given in Chapter 11.

Chapter 2

Surface Integral Equation

The scattering of closed and composite bodies is a problem in the electromagnetic field theory, which arose in the 1960s. The radar application of that time required the knowledge of the radar cross-section of moving objects for clear detection [Bow69, Cri68]. Although computer science was at its beginning, many efforts were made to calculate the radar cross-sections of basic geometric objects analytically, e.g., perfectly conducting sphere [Mie1908], cone [Bai56] or elliptic disk [Bjö91]. The evaluation of more complex geometries requires advanced numerical methods. One well-proved method is based on the well-known equivalence principle, first derived by Huygens [Bal89, Bla07]. A virtual surface is used to derive equivalent electric and magnetic surface currents, which radiate in free space. The equivalent surface currents are found to generate the scattering field of interest, which is used to calculate the radar cross-section in a further step.

The initial investigations focused on perfectly electric conductors (PEC) placed in free space. In this special case, the virtual surface can be chosen to be the real surface of the body and the equivalent surface current is equal to the real surface current that exists on the PEC body. In a more general case,

2. Surface Integral Equation

where the body is made out of dielectric material or composite materials, the equivalent surface current is an abstract source distribution required to derive the scattering field of interest.

A large number of formulations exists, but most of these are suitable only for specific problems. The widely-used electric field integral equation (EFIE) is the most stable formulation for planar structures and, with some limitations, for closed PEC bodies. Apart from the commonly used EFIE, the so-called magnetic field integral equation (MFIE) is used for closed PEC bodies. In the following sections, the two basic formulations are explained in brief, as they are required for the calculation of the Characteristic Modes with the Method of Moments (MoM) in this work [Wat02, Har68].

2.1 Electric Field Integral Equation (EFIE)

The electromagnetic scattering of a PEC body can be described by the extinction theorem [Bal89]. Fig. 2-1 illustrates the principle of the extinction theorem. In order to derive the principle behind this formulation, let us assume that an incident electric field \mathbf{E}_{inc} , e.g., an incoming plane wave, excites the closed PEC body. The boundary condition of the PEC body enforces the tangential component of the electric field on the surface to vanish. Therefore, a second electric field \mathbf{E}_S , in addition to the \mathbf{E}_{inc} , exists, to compensate for the tangential component of the total electric field on the surface S . This electric field \mathbf{E}_S is generated by the surface current distribution \mathbf{J} on a virtual arbitrary surface S placed in free space (ϵ_0, μ_0).

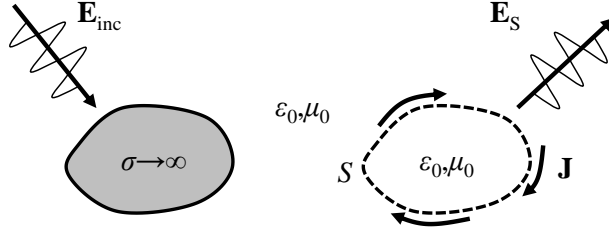


Fig. 2-1 Equivalent surface principle for the EFIE.

The boundary condition on the surface S is:

$$[\mathbf{E}_{\text{inc}} + \mathbf{E}_S]_{\text{tan}} = 0, \quad (2.1)$$

where the subscript “tan” denotes the tangential component.

The scattering field \mathbf{E}_S is calculated by the magnetic vector potential \mathbf{A} and the scalar electric potential ϕ with

$$\mathbf{E}_S(\mathbf{r}) = -j\omega\mathbf{A}(\mathbf{r}) - \text{grad}(\phi(\mathbf{r})), \quad (2.2)$$

where ω is the angular frequency.

The vector potential \mathbf{A} can be calculated with:

$$\mathbf{A}(\mathbf{r}) = \mu \iint_S \mathbf{J}(\mathbf{r}') \frac{e^{-jk|\mathbf{r}-\mathbf{r}'|}}{4\pi|\mathbf{r}-\mathbf{r}'|} dS' \quad (2.3)$$

and the scalar potential ϕ with:

$$\phi(\mathbf{r}) = \frac{-1}{j\omega\epsilon} \iint_S \nabla \cdot \mathbf{J}(\mathbf{r}') \frac{e^{-jk|\mathbf{r}-\mathbf{r}'|}}{4\pi|\mathbf{r}-\mathbf{r}'|} dS'. \quad (2.4)$$

In (2.3) and (2.4), \mathbf{r}' is related to the source on the surface S and \mathbf{r} is related to the observation point in free space. The term

2. Surface Integral Equation

$$G(\mathbf{r}, \mathbf{r}') = \frac{e^{-jk|\mathbf{r}-\mathbf{r}'|}}{4\pi|\mathbf{r}-\mathbf{r}'|} \quad (2.5)$$

in (2.3) and in (2.4) is called the Green's function of the free space. Applying the boundary condition (2.1) with (2.2), the EFIE formulation can be derived:

$$\begin{aligned} \mathbf{E}_{\text{inc}}(\mathbf{r}) &= j\omega\mu \iint_S \mathbf{J}(\mathbf{r}') \frac{e^{-jk|\mathbf{r}-\mathbf{r}'|}}{4\pi|\mathbf{r}-\mathbf{r}'|} dS' \\ &+ \nabla \left(\frac{-1}{j\omega\epsilon} \iint_S \nabla \cdot \mathbf{J}(\mathbf{r}') \frac{e^{-jk|\mathbf{r}-\mathbf{r}'|}}{4\pi|\mathbf{r}-\mathbf{r}'|} dS' \right) \\ &= \mathbf{L}(\mathbf{J}) . \end{aligned} \quad (2.6)$$

This formulation is widely used in the TCM, since the EFIE is generally known to be robust for planar structures. A more detailed and general derivation of the EFIE (and the MFIE) can be found in Appendix A1. However, this formulation has a convergence problem for low frequencies. This effect is called the low-frequency break down [Wat02, Nai09], and it gives the lower bound for this formulation. In case of closed PEC bodies, the EFIE can have an additional convergence issue, which is known as the internal resonance problem [Wat02, Pet90]. Internal fields can exist from the theoretical point of view and these vanish at the closed surface S . A unique solution in this case cannot be found. Special techniques are required to avoid this internal resonance problem. Some solutions for this problem are available in [Can91, Hel93, Pra01, Rao90].

2.2 Magnetic Field Integral Equation (MFIE)

The principle behind the magnetic field integral equation (MFIE) is similar to the EFIE as described in chapter 2.1. The magnetic field is used to set up the boundary condition on the surface of the closed PEC body:

$$\mathbf{n} \times [\mathbf{H}_{\text{inc}} + \mathbf{H}_s] = \mathbf{J}. \quad (2.7)$$

This condition is used to derive the general valid MFIE (also known as the NxMFIE) formulation:

$$\mathbf{n} \times \mathbf{H}_{\text{inc}}(\mathbf{r}) = \frac{\Omega}{4\pi} \mathbf{J}(\mathbf{r}) - \mathbf{n} \times \iint_s \mathbf{J}(\mathbf{r}') \times \nabla' \left(\frac{e^{-jk|\mathbf{r}-\mathbf{r}'|}}{4\pi|\mathbf{r}-\mathbf{r}'|} \right) dS'. \quad (2.8)$$

In (2.8), Ω is the solid angle, which is typically set $\Omega=2\pi$. More detailed information can be found in [Erg05].

The formulation (2.8) does not reveal the so-called “low frequency breakdown,” as is the case for the EFIE. The frequency dependence is concentrated in the gradient of the Green’s function in (2.8). Therefore, this formulation is suitable for very low frequency. The disadvantage lies in the internal resonance problem, which has a high influence on the convergence of the numerical solution. Further, the MFIE requires a higher mesh density compared to the EFIE to achieve similar results. Additional information can be found in [Wat02] and the Appendix A1.

2. Surface Integral Equation

Chapter 3

Method of Moments

The Method of Moments (MoM) is a favorite technique to calculate characteristic modes numerically. It implies a matrix that can be evaluated with different numerical methods for different integral equations. The entities of the matrix describes the coupling between the small portions of the scattering surface. If the EFIE is used, the entries of the matrix are the mutual impedance, and the overall matrix is called the impedance matrix of the body. This impedance matrix links the unknown current with the impressed voltage on the surface. In order to solve the MoM, the unknown quantity — here the surface current — is expanded with a limited set of basis functions. The superposition of the weighted basis functions gives the surface current of interest. The choice of the basis function is essential for the MoM and the convergence speed of the solution. The complexity of the numerical evaluation of the integral terms can be reduced significantly, if the basis function is chosen well. Two fundamental types of basis functions exist, which are widely used in the electromagnetic field theory: the Dirac- and the pulse function [Bla07].

In the past few decades, the so-called Rao-Wilton-Glisson (RWG) basis function [Rao80, Rao82] has proved itself for the SIE and the TCM. The RWG

3. Method of Moments

basis function is a triangular pulse function which models the surface current with a set of dipoles placed tangentially on the surface. Owing to the simplicity of the RWG basis function, it is widely used in the TCM computation. Moreover, the tetrahedral basis function [Sch84] can be used for the VIE and the characteristic mode computation as an alternative. More exotic basis functions are the roof-top basis function [Ser99], the polynomial basis function [Jor04] or the linear-linear basis function [Ozg07]. These exotic basis functions and the tetrahedral basis function are complex, and require more computational efforts. For these reasons, they are not popular in the TCM and, so, are not discussed in this work.

3.1 The RWG Basis Function

The RWG basis function was first introduced by Rao [Rao80] in 1980. The triangular pulse function is a divergence conforming basis function suitable for the surface integral formulations (EFIE, MFIE and PMCHWT: please see Chapter 3.3). The surface current is modeled as a combination of dipoles lying planar on the entire surface. The combination of two triangles can be understood as a single dipole orientated from the A_m^+ triangle to the A_m^- triangle. Each triangle of the RWG function represents a constant surface charge density. Two triangles, which have different charges, assume a constant surface current flow between adjacent vertices across the length l_m . The ρ_m^\pm vector is used to set up the surface current flow as denoted in Fig. 3-1.

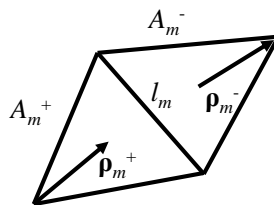


Fig. 3-1 The m -th RWG basis function. This figure is based on the idea in © [Rao80] 1980.

The m -th RWG basis function is defined with

$$\mathbf{f}_{\text{RWG},m}(\mathbf{r}) = \begin{cases} \frac{l_m}{2A_m^+} \boldsymbol{\rho}_m^+ & \mathbf{r} \in A_m^+ \\ \frac{l_m}{2A_m^-} \boldsymbol{\rho}_m^- & \mathbf{r} \in A_m^- \\ 0 & \text{else} \end{cases} \quad (3.1)$$

The divergence of (3.1) is constant over the respective triangles, and is:

$$\nabla \cdot \mathbf{f}_{\text{RWG},m}(\mathbf{r}) = \begin{cases} \frac{l_m}{A_m^+} & \mathbf{r} \in A_m^+ \\ -\frac{l_m}{A_m^-} & \mathbf{r} \in A_m^- \\ 0 & \text{else} \end{cases} \quad (3.2)$$

From (3.2) the charge density ρ_{RWG} can be defined with:

$$\rho_{\text{RWG},m} = \frac{1}{j\omega} \nabla \cdot \mathbf{f}_{\text{RWG},m}(\mathbf{r}). \quad (3.3)$$

The divergence conforming property of the RWG basis function makes this function suitable for the EIFE formulation, as explained in [Mak02] in detail. Alternative formulations (e.g. MFIE) can be used in combination with the RWG basis function with some limitations. Prior investigations show that the surface has to be meshed with a higher RWG density compared with the robust EFIE formulation.

3.2 Testing Procedure

The testing of the integral equations is essential for the convergence speed of the MoM solution. The main premise of the testing procedure is to derive scalar values out of the vector terms, e.g. in (2.6), which are used to fill the MoM

3. Method of Moments

matrix. The choice of the testing function is not limited in general. However, two concepts are used in the praxis. First of all, the so-called Point-Matching can be used to derive simplified terms, which can be evaluated numerically with less effort. For that, the Dirac Function is used as the testing function. The disadvantage of the Point-Matching is the lower accuracy of the integral terms and the slow convergence of the solution. Hereafter, the Galerkin-Procedure is widely used in the literature to evaluate the matrix elements numerically. In this procedure, the RWG basis function $\mathbf{f}_{\text{RWG},n}$ is used to test the integral terms. This procedure has the advantage of attaining a high accuracy of the solution. Moreover, this testing scheme gives a symmetric MoM matrix, which is important for the TCM. The symmetry of the matrix is a key point in the TCM and the way in which the characteristic modes are interpreted for the antenna design. For these reasons, this testing procedure is preferred for the TCM analysis, rather than the Point-Matching.

The testing scheme for the impedance matrix entities $Z_{n,m}$ with the Galarkin-Procedure for the EFIE is:

$$Z_{n,m} = \left\langle \mathbf{f}_{\text{RWG},n}, \mathbf{L}(\mathbf{f}_{\text{RWG},m}) \right\rangle = \iint_S \mathbf{f}_{\text{RWG},n} \cdot \mathbf{L}(\mathbf{f}_{\text{RWG},m}) dS \quad (3.4)$$

where \mathbf{L} represents the surface integral equation, with the EFIE as denoted in (2.6).

In the same manner, the excitation vector \mathbf{V} can be calculated with:

$$V_n = \left\langle \mathbf{f}_{\text{RWG},n}, \mathbf{E}_{\text{inc}} \right\rangle. \quad (3.5)$$

The combination of (3.4) and (3.5) leads to the matrix formulation of the scattering problem

$$\underbrace{\begin{bmatrix} \langle \mathbf{f}_{\text{RWG},1}, \mathbf{E}_{\text{inc}} \rangle \\ \langle \mathbf{f}_{\text{RWG},2}, \mathbf{E}_{\text{inc}} \rangle \\ \vdots \end{bmatrix}}_{\mathbf{V}} = \underbrace{\begin{bmatrix} \langle \mathbf{f}_{\text{RWG},1}, \mathbf{L}(\mathbf{f}_{\text{RWG},1}) \rangle & \langle \mathbf{f}_{\text{RWG},1}, \mathbf{L}(\mathbf{f}_{\text{RWG},2}) \rangle & \cdots \\ \langle \mathbf{f}_{\text{RWG},2}, \mathbf{L}(\mathbf{f}_{\text{RWG},1}) \rangle & \ddots & \\ \vdots & & \ddots \end{bmatrix}}_{\mathbf{Z}} \cdot \underbrace{\begin{bmatrix} I_1 \\ I_2 \\ \vdots \end{bmatrix}}_{\mathbf{I}}, \quad (3.6)$$

which is typically summarized into:

$$\mathbf{V} = \mathbf{Z} \cdot \mathbf{I}. \quad (3.7)$$

The unknown coefficients of the respective basis functions \mathbf{f}_{RWG} , which can be found in the current vector \mathbf{I} , are calculated with a matrix inversion of \mathbf{Z} .

$$\mathbf{I} = \mathbf{Z}^{-1} \cdot \mathbf{V}. \quad (3.8)$$

The principle to evaluate the matrix elements for the MFIE can be utilized with fewer modifications in a similar way.

3.3 PHMCTW Formulation for Dielectric and Magnetic Bodies

The formulations (EFIE and MFIE), reviewed in brief, are valid for PEC bodies placed in free space. These basic integral formulations can be combined into different extended formulations, which enable the treatment of dielectric and magnetic bodies. The first formulation suitable for the numerical evaluation with the MoM was the so-called PMCHWT (Poggio-Miller-Chang-Harrington-Wu-Tsai) formulation from 1971 [Har72a, Uma86]. Later, this formulations was modified, in order to improve the matrix calculation (e.g. Normal Müller Formulation or Combined Normal Formulation). Although other formulations yield more accurate results for specific geometries, only the

3. Method of Moments

PMCHWT formulation has a symmetric matrix, which enables real characteristic modes and real valued eigenvalues [Har72a]. These properties are important for the TCM analysis and, hence, the PMCHWT is used in this work.

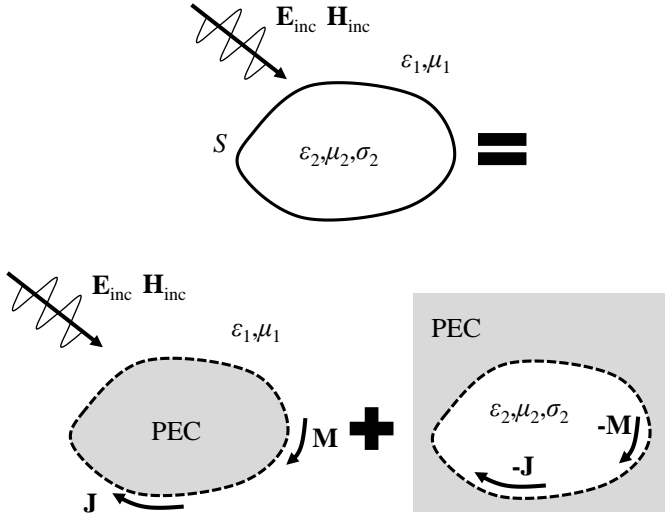


Fig. 3-2 Equivalence principle of the PMCHWT formulation.

The matrix formulation of the PMCHWT integral representation is:

$$\begin{bmatrix} \mathbf{V}_e \\ \mathbf{V}_m \end{bmatrix} = \begin{bmatrix} \mathbf{Z}_1 + \mathbf{Z}_2 & \mathbf{K}_1 + \mathbf{K}_2 \\ -\mathbf{K}_1 - \mathbf{K}_2 & \mathbf{Y}_1 + \mathbf{Y}_2 \end{bmatrix} \begin{bmatrix} \mathbf{I}_e \\ \mathbf{I}_m \end{bmatrix}. \quad (3.9)$$

In (3.9), the matrixes and vectors are defined as follows:

$$\begin{aligned} Z_{i,n,m} = & \left\langle \mathbf{f}_{\text{RWG},n}, j\omega\mu_i \iint_S \mathbf{f}_{\text{RWG},m} G_i(\mathbf{r}, \mathbf{r}') dS' \right\rangle + \\ & \left\langle \mathbf{f}_{\text{RWG},n}, \nabla \left(\frac{-1}{j\omega\epsilon_i} \iint_S \nabla \cdot \mathbf{f}_{\text{RWG},m} G_i(\mathbf{r}, \mathbf{r}') dS' \right) \right\rangle \end{aligned} \quad (3.10)$$

$$Y_{i,n,m} = \left\langle \mathbf{f}_{\text{RWG},n}, j\omega\epsilon_i \iint_S \mathbf{f}_{\text{RWG},m} G_i(\mathbf{r}, \mathbf{r}') dS' \right\rangle + \left\langle \mathbf{f}_{\text{RWG},n}, \nabla \left(\frac{-1}{j\omega\mu_i} \iint_S \nabla \cdot \mathbf{f}_{\text{RWG},m} G_i(\mathbf{r}, \mathbf{r}') dS' \right) \right\rangle \quad (3.11)$$

$$K_{i,n,m} = \left\langle \mathbf{f}_{\text{RWG},n}, \iint_S \mathbf{f}_{\text{RWG},m} \times \nabla' G_i(\mathbf{r}, \mathbf{r}') dS' \right\rangle \quad (3.12)$$

$$G_i(\mathbf{r}, \mathbf{r}') = \frac{e^{-jk_i|\mathbf{r}-\mathbf{r}'|}}{4\pi|\mathbf{r}-\mathbf{r}'|} \quad (3.13)$$

$$V_{e,n} = \left\langle \mathbf{f}_{\text{RWG},n}, \mathbf{E}_{\text{inc}}(\mathbf{r}) \right\rangle \quad (3.14)$$

$$V_{m,n} = \left\langle \mathbf{f}_{\text{RWG},n}, \mathbf{H}_{\text{inc}}(\mathbf{r}) \right\rangle \quad (3.15)$$

The subscript “ i ” is related to the i -th medium and “ n, m ” is related to the n -th testing and m -th basis function. The \mathbf{I}_e and \mathbf{I}_m vectors respectively contain the coefficients of the electric current \mathbf{J} and the magnetic current \mathbf{M} on the surface S .

The material parameters are defined with:

$$\epsilon_i = \epsilon_0 \epsilon_{r,i} - j \frac{\sigma_i}{\omega}, \quad (3.16)$$

$$\mu_i = \mu_0 \mu_{r,i} - j \frac{\sigma_{m,i}}{\omega}, \quad (3.17)$$

and

$$k_i = \omega \sqrt{\epsilon_i \mu_i}. \quad (3.18)$$

3. Method of Moments

In (3.16) and (3.17), ε_0 , $\varepsilon_{r,i}$, σ_i , μ_0 , $\mu_{r,i}$ and $\sigma_{m,i}$ are the permittivity of the free space, the relative permittivity, electric conductivity, permeability of the free space, relative permeability and the magnetic conductivity, respectively.

First of all, the system matrix in (3.9) is not symmetrical due to the minus sign in the upper \mathbf{K}_i operator. But with a few modifications, the system matrix can be made symmetrical for the TCM analysis. This concept is explained in the Chapter 4.3.

3.4 Efficient Numerical Evaluation of the Integral Equations

An efficient numerical calculation of the reviewed integral formulations requires advanced techniques. The matrix elements in (3.4) are calculated in two phases. In the first phase, the internal surface integral is evaluated with either the seven-point integration rule [Sav96] or with the Barycentric subdivision [Kam98] (see Appendix C). For both types of numerical treatments, the sampling points are used over the triangle surface to approximate the internal integral. In the second phase, the testing integral (3.4) is evaluated with the Mid-Point Rule [Rao80]. For this, the midpoint of the respective triangle is used to approximate the interaction of the testing function with the basis function. A detailed description can be found in Appendix B1.

Furthermore, the singularity extraction method is required to calculate the internal surface integral over the Green's function. In case of zero distance between the observation point \mathbf{r} and the source point \mathbf{r}' , the numerical evaluation of the Green's function with the samples is difficult. The singularity of the Green's function is extracted, and the term is split into a numerical and an analytical term. The numerical term is continuous and can be evaluated with

3.4 Efficient Numerical Evaluation of the Integral Equations

the given sampling points of the surface. The analytical term is solved in closed form with the evaluation of the contour integral instead of the surface integral. A description of the singularity extraction and the analytic solution can be found in [YOi03] and in Appendix B2 and B3.

3. Method of Moments

Chapter 4

The Theory of Characteristic Modes

The Theory of Characteristic Modes (TCM) was derived by Garbacz, Harrington and Mautz in the 1960s and 1970s. The initial idea to decompose the scattering field into an orthogonal field pattern was first reported by Garbacz in 1965 [Gar65, Gar68]. Later, this idea was developed further into the current known formulation by Harrington and Mautz in 1971 [Har71a, Har71b]. The authors exploited the generalized eigenvalue equation to derive equivalent modal surface currents, which are orthogonal with respect to the power budget. The same authors extended the basic theory, which is — first of all — valid for PEC bodies, towards the lossy dielectric and magnetic materials [Har72a, Har72a, Cha77]. Furthermore, Garbacz utilized the TCM on the network parameter of a multi-antenna system [Gar71]. He described the input admittance and the mutual admittance with a summation of the modal admittances. In 1972, Harrington and Mautz evaluated the modal Q-Factor directly from the eigenvalue of the respective mode [Har72b]. They demonstrated that the usage of lumped reactive elements can displace the resonance frequency of the modes selectively. These publications may pave the way for the development of equivalent circuits with the TCM and facilitate the fundamental understanding of the internal coupling phenomenon from a network theory point of view.

4. The Theory of Characteristic Modes

In the 1980s, the TCM was not developed further. The small amount of available publications in this area deal with specific problems, which are treated analytically [Kab87a, Kaba87b]. The limitation in the numerical computation with available computer programs of that time harms the TCM analysis for more realistic geometries and applications. With the increasing memory size and CPU speed of modern computers at the beginning of the 1990s, the TCM became more interesting for antenna design. The first antenna design concept, based on the TCM, was the UHV application for the land vehicles in [Mur94, Aus98].

The newly rising mobile phone market at the beginning of 2000 facilitated the TCM research for small antenna design. The pioneers in this research field found the TCM to be suitable for the understanding of the fundamental radiation principle and the influence of the small chassis. In [Man01] and in [Vai02], the TCM is used to describe the antenna resonances which are highly influenced by the finite size chassis. From that time onward, the TCM has been used for a large number of applications. In recent years, the TCM is again being used for the integration and optimization of the chassis conformal antennas in automotive applications (e.g. vehicle, aircraft [Cha14] and ship [Che14b]). A more detailed description of the history of TCM and its applications can be found in e.g. [Che15].

In the next few paragraphs, the generalized eigenvalue problem, as a fundamental mathematical background, is reviewed, and basic parameters are introduced, which are required for the discussion in this work.

4.1 The Generalized Eigenvalue Problem for PEC Modes

The generalized eigenvalue equation is a powerful method to solve advanced problems, and not only in the electromagnetic field theory. Other scientific fields, e.g. theoretical physics, benefit from the eigenvalue decomposition, as it allows scientists to solve complex differential equations. The basic idea of the TCM is to find orthogonal eigenvectors, which span out the sub-space of the solution. A complex matrix that describes the respective problem is used to calculate the eigenvectors and eigenvalues. Let us assume a complex impedance matrix $\mathbf{Z} = \mathbf{R} + j\mathbf{X}$ is given, as described in Chapter 3. The generalized eigenvalue equation in this case [Har71a] is:

$$\mathbf{X}\mathbf{J}_n = \lambda_n \mathbf{R}\mathbf{J}_n. \quad (4.1)$$

In (4.1), \mathbf{J}_n is the n -th characteristic mode (also commonly called *mode* or *wave mode*) and λ_n is the n -th eigenvalue. From (4.1) the eigenvectors \mathbf{J}_n can be scaled arbitrarily, but typically they are scaled to unity with:

$$\frac{1}{2} \langle \mathbf{J}_n, \mathbf{R}\mathbf{J}_n \rangle = 1. \quad (4.2)$$

This orthogonality of the modes can be summarized with three basic equations:

$$\frac{1}{2} \langle \mathbf{J}_m, \mathbf{Z}\mathbf{J}_n \rangle = (1 + j\lambda_n) \delta_{nm}, \quad (4.3)$$

$$\frac{1}{2} \langle \mathbf{J}_m, \mathbf{R}\mathbf{J}_n \rangle = \delta_{nm} \quad (4.4)$$

and

$$\frac{1}{2} \langle \mathbf{J}_m, \mathbf{XJ}_n \rangle = \lambda_n \delta_{nm}. \quad (4.5)$$

The δ_{nm} in (4.3), (4.4) and (4.5) denotes the Kronecker-Delta function ($\delta_{nm}=1$, if $n=m$ and 0 otherwise). The orthogonality of the modes is a useful property, which is a strict consequence of the generalized eigenvalue equation (4.1). It is noticeable that the characteristic modes are not strictly orthogonal, as the operation:

$$\frac{\langle \mathbf{J}_m, \mathbf{J}_n \rangle}{|\mathbf{J}_m| \cdot |\mathbf{J}_n|} \neq \delta_{nm} \quad (4.6)$$

is not valid.

An additional fact is important for the TCM analysis; this is related to the impedance matrix of the MoM. The symmetry of the impedance matrix \mathbf{Z} is the reason for the real valued eigenvalues λ_n and real characteristic modes \mathbf{J}_n in (4.1). In contrast to other well-known and trusted mode decomposition methods (e.g. for microstrip antennas, [Bal89, Bal05, Jam89]), the resonance frequency of the characteristic modes is real and allows a more intuitive interpretation of the radiation mechanism.

Other properties related to the matrix formulation (4.1) are explained in the next section.

4.2 On the Property of the Characteristic Modes

The impedance matrix \mathbf{Z} is related to the power and energy of the body. As described in [Har71a], the field distribution exterior to the body has a clear relationship with the radiated power P_{rad} with:

$$P_{\text{rad}} = \frac{1}{2} \iint_{S \rightarrow \infty} \mathbf{E} \times \mathbf{H}^* dS = \text{Re} \left\{ \frac{1}{2} \iint_S \mathbf{E} \times \mathbf{H}^* dS \right\} = \text{Re} \left\{ \frac{1}{2} \langle \mathbf{J}, \mathbf{ZJ} \rangle \right\}. \quad (4.7)$$

In (4.7), \mathbf{E} , \mathbf{H} and \mathbf{J} are respectively the total electric field, the total magnetic field and the total surface current. The $(S \rightarrow \infty)$ denotes the envelope surface in infinity. Eq. (4.7) is, in general, valid for lossless PEC bodies and can applied on the modes with the Poynting Theorem (as described in [Bal89]) with:

$$\begin{aligned} P_n &= \text{Re} \left\{ \frac{1}{2} \iint_S \mathbf{E}_n \times \mathbf{H}_n^* dS \right\} + j\omega \iiint_V \frac{1}{4} (\mu_0 |\mathbf{H}_n|^2 - \varepsilon_0 |\mathbf{E}_n|^2) dV \\ &= \frac{1}{2} \langle \mathbf{J}_n, \mathbf{ZJ}_n \rangle = 1 + j\lambda_n \end{aligned} \quad (4.8)$$

From (4.8), it is obvious that the eigenvalue λ_n is directly related to the reactive power of the system and allows scientists to classify the modes with respect to the energy stored. If the eigenvalue is negative ($\lambda_n < 0$), the mode stores more electric energy rather than magnetic energy. In this case, the mode is said to be *capacitive*. In the other case, if the eigenvalue is positive ($\lambda_n > 0$), more magnetic energy is stored rather than electric energy and the mode is called *inductive*. In the special case — where the eigenvalue is equal to zero ($\lambda_n = 0$) — the mode is in *resonance*. The resonance is a desirable state, since the reactive power of modes is zero. Therefore, any antenna design concept is aimed at the resonance of certain modes in the desired frequency bands [Cab07].

The power budget of the total surface current \mathbf{J} can be expanded with the TCM in an intuitive way. For that, the total surface current \mathbf{J} is decomposed into an infinite summation of modes \mathbf{J}_n with:

$$\mathbf{J} = \sum_{n=1}^{\infty} a_n \mathbf{J}_n, \quad (4.9)$$

4. The Theory of Characteristic Modes

where a_n is the complex coefficient. This can be calculated with:

$$a_n = \frac{\langle \mathbf{J}_n, \mathbf{E}_{\text{inc}} \rangle}{2(1 + j\lambda_n)}. \quad (4.10)$$

Evaluating (4.7) with (4.8) reveals the power budget and the obvious advantage of the TCM. The factor 2 in (4.10) is the consequence of the normalization in (4.4) (please see [Bla07, Kre12] for additional explanations).

The total radiated power P_{rad} is decomposed into portions; each mode contributes with:

$$P_{\text{rad}} = \sum_{n=1}^{\infty} |a_n|^2. \quad (4.11)$$

If (4.11) is normalized to the total radiated power, a more simple formulation can be found:

$$1 = \sum_{n=1}^{\infty} \frac{|a_n|^2}{P_{\text{rad}}} = \sum_{n=1}^{\infty} |b_n|^2. \quad (4.12)$$

In (4.12), b_n is the normalized coefficient of the n -th mode. The magnitude square of b_n is the percentage power each mode contributes to the overall power P_{rad} .

A more suitable depiction of the excitation coefficient is the so-called power coefficient [Led15]. This coefficient takes the impedance matching of the feeding port into account and gives information about how efficiently the modes are excited. The weighting of the square normalized coefficient with the scattering parameter of a single port system gives the power coefficient c_n :

$$c_n = |b_n|^2 \left(1 - |S_{11}|^2\right). \quad (4.13)$$

Any antenna design concept is aimed at the excitation of the resonant modes and the impedance matching of the feeding port. Therefore, this coefficient is more suitable to quantify the mode excitation with a concentrated single port.

4.3 The Generalized Eigenvalue Problem for Dielectric and Magnetic Modes

In the previous section, the basic TCM concept — valid for PEC bodies placed in free space — is reviewed. This concept can be extended towards the dielectric and magnetic bodies, including loss [Har72a, Cha77] in the SIE. In Chapter 3.3, the PMCHWT formulation for the SIE is presented, which includes an extended system matrix. This matrix is not symmetrical as denoted in (3.9). For this reason, the matrix formulation of the problem presented is not suitable for the TCM analysis. A few modifications are required to achieve a symmetric matrix, which enables real surface current modes and real eigenvalues.

The magnetic surface current \mathbf{M} (respectively, the current vector \mathbf{I}_m) is extended with the imaginary unit, and the matrix formulation now becomes:

$$\begin{bmatrix} \mathbf{V}_e \\ j\mathbf{V}_m \end{bmatrix} = \underbrace{\begin{bmatrix} \mathbf{Z}_1 + \mathbf{Z}_2 & -j(\mathbf{K}_1 + \mathbf{K}_2) \\ -j(\mathbf{K}_1 + \mathbf{K}_2) & \mathbf{Y}_1 + \mathbf{Y}_2 \end{bmatrix}}_{\mathbf{T}} \cdot \begin{bmatrix} \mathbf{I}_e \\ j\mathbf{I}_m \end{bmatrix}. \quad (4.14)$$

From (4.14), the generalized eigenvalue equation is:

$$\text{Im}\{\mathbf{T}\} \cdot \mathbf{W}_n = \lambda_n \text{Re}\{\mathbf{T}\} \cdot \mathbf{W}_n. \quad (4.15)$$

In (4.15), \mathbf{W}_n is the n -th characteristic mode of the lossy dielectric and magnetic body and can be further decomposed into:

$$\mathbf{W}_n = \begin{bmatrix} \mathbf{J}_n \\ j\mathbf{M}_n \end{bmatrix}. \quad (4.16)$$

And again, the characteristic mode \mathbf{W}_n is a real valued vector with a real valued eigenvalue λ_n . The magnetic current mode \mathbf{M}_n has a fixed phase shift of 90° to the electric surface current mode \mathbf{J}_n due to the imaginary unit j in (4.16).

In the case of lossless materials, the modal far fields of \mathbf{W}_n are orthogonal, as demanded in the common theory for PEC bodies. However, in case of lossy materials, the orthogonality of the modal far fields is not valid anymore. Although the orthogonal property of the modes is lost in the far field, an interpretation of the scattering phenomenon can be made with some limitations. This problem is discussed in Chapter 8.4 (for lossy components included in the TCM) and Chapter 9.4 (for lossy materials).

At this point, it should be noticed that the eigenvalue λ_n of dielectric modes \mathbf{W}_n cannot be used to determine the resonance of the mode in general. This circumstance is a major drawback at first appearance. However, a physical interpretation of the eigenvalue λ_n can still be given and used for the antenna design. This issue is explained in Chapter 9.

4.4 Characteristic Mode Computation

In order to solve the Generalized Eigenvalue Equation (4.1) or (4.14), two program libraries can be used; the LAPACK [LAP] and the ARPACK [ARP] libraries. Both libraries are written in Fortran77 and are available in MATLAB [MAT] or as dynamic libraries. A more special method can be found in [Har71b], which is based on the so-called SVD (Singular Value Decomposition).

The LAPACK library provides the EIG Function which is able to calculate all

eigenvalues and eigenvectors of a symmetric matrix. The numerical calculation of the characteristic modes with this function gives the relevant modes required to analyze the given body. In addition, other typically none real eigenvectors are given, which cannot be used for the TCM. Therefore, the output parameter (eigenvectors and eigenvalues) has to be filtered for the real modes. The second library (ARPACK) provides the EIGS Function, which can calculate the relevant modes without any other disturbed (incorrect) modes. For this, the function requires the number of modes to be calculated as a parameter. Since it can be difficult to estimate the number of the relevant modes at the beginning of the TCM analysis, some initial experiments may be required to find the right number. The SVD method (as described in [Har71b]) delivers all relevant modes without an additional parameter. However, the SVD method can give inaccurate modes, if the geometry is complex. From the available routines and methods, the EIGS Function is preferred to calculate the modes numerically. In practice, only a few modes are interesting for the TCM analysis.

4.5 Characteristic Basis Function (CBF)

The characteristic modes can be used to decompose an arbitrary surface current distribution \mathbf{J} as denoted in (4.9), if an infinite set of modes is used. In common applications, a limited set of modes is sufficient, which has a small eigenvalue, i.e., small magnitude value $|\lambda_n|$. In [Pra03], the author describes an idea to use a limited number of orthogonal modes as the basis function (instead of the RWG) in the MoM. This principle can help reduce the size of the matrix and save computation time. The characteristic basis function is commonly used to solve large-scale problems [Mit08, Maa08] or to analyze not connected coupled structures [Hu14].

4. The Theory of Characteristic Modes

In order to use the characteristic basis function in the MoM, an additional calculation step is required. First of all, the impedance matrix \mathbf{Z} is calculated, as described in Chapter 3. Next, a limited set of N characteristic modes \mathbf{J}_n is calculated with (4.1) and normalized as usual. Now, the basis function \mathbf{f}_{RWG} is replaced with the characteristic modes and a new matrix \mathbf{Z}_{CBF} is calculated with:

$$\mathbf{Z}_{\text{CBF}} = [\mathbf{J}_1 \quad \cdots \quad \mathbf{J}_N]^T \cdot \mathbf{Z} \cdot [\mathbf{J}_1 \quad \cdots \quad \mathbf{J}_N]. \quad (4.17)$$

In the same manner, the excitation vector \mathbf{V}_{CBF} is defined with:

$$\mathbf{V}_{\text{CBF}} = [\mathbf{J}_1 \quad \cdots \quad \mathbf{J}_N]^T \mathbf{V}. \quad (4.18)$$

The original problem of the MoM is now simplified to:

$$\mathbf{V}_{\text{CBF}} = \mathbf{Z}_{\text{CBF}} \cdot \mathbf{I}_{\text{CBF}}. \quad (4.19)$$

The matrix \mathbf{Z}_{CBF} has the dimension $N \times N$ and is much smaller than the original matrix \mathbf{Z} . The unknown vector \mathbf{I}_{CBF} contains the coefficients a_n of the respective characteristic modes \mathbf{J}_n . As a more advanced concept, the linear equation in (4.19) can be used in a second generalized eigenvalue equation to calculate coupled characteristic modes.

4.6 Examples

In order to introduce the TCM and the basic parameters required in this thesis, two simple examples — a dipole and a rectangular plate — are investigated. The examples will show what the eigenvalue of common modes look like and how they affect the input impedance of a feeding port. Furthermore, these examples demonstrate how the modes are excited with common feeding concepts (plane wave and concentrated voltage source).

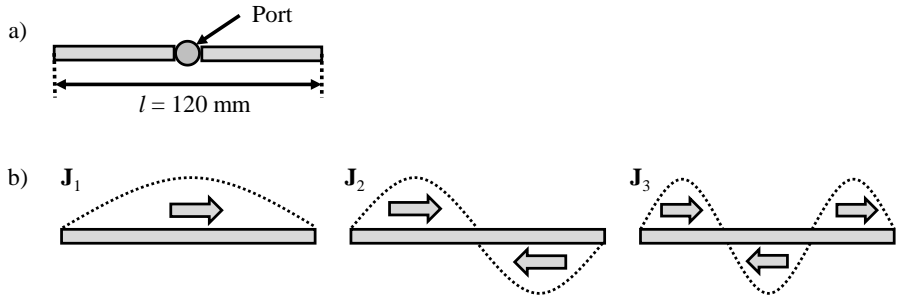


Fig. 4-1 Center-fed dipole having the length $l = 120$ mm a) and three lower order modes \mathbf{J}_{1-3} b). © IEEE 2014 [Saf14].

4.6.1 Dipole

The first example is the simplest example that can be found in literature. A dipole having the length $l = 120$ mm is fed with a delta-gap voltage (please see Appendix C3 or [Mak03] for details), placed at the center. The first three lower order modes \mathbf{J}_{1-3} can be found in the observed frequency range ($0.5 \leq f[\text{GHz}] \leq 4$) shown in Fig. 4-1 b).

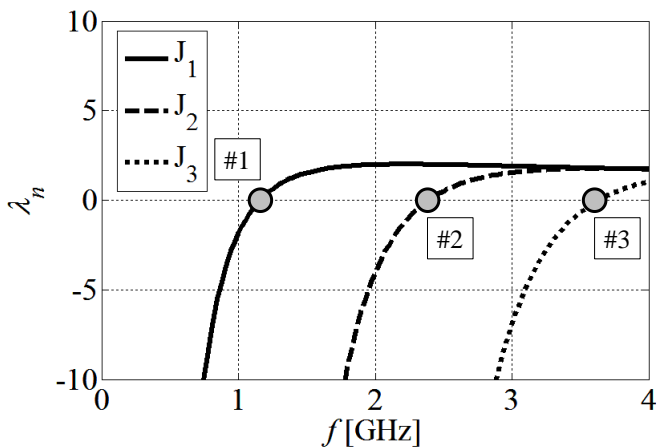


Fig. 4-2 Eigenvalues of the first three characteristic modes of a center-fed dipole having the length $l = 120$ mm.

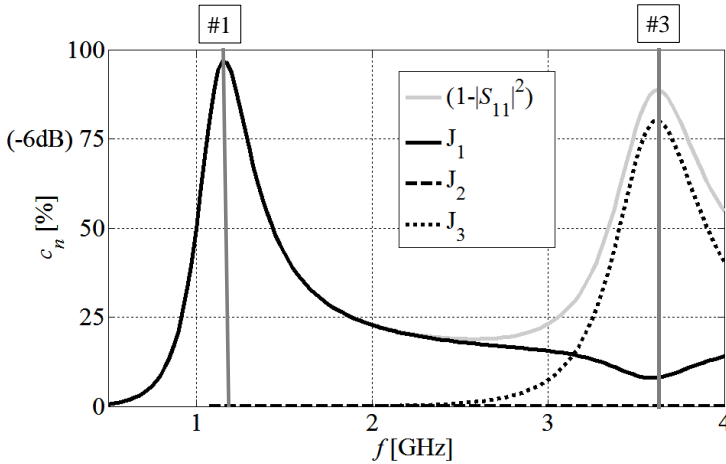


Fig. 4-3 Power coefficient a_n of the first three characteristic modes of a center-fed dipole having the length $l = 120$ mm.

The first three modes \mathbf{J}_{1-3} have a resonance (#1 – #3 in Fig. 4-2) in the frequency range sought, as it can be observed in Fig. 4-2. Owing to the excitation in the center of the dipole, only two modes (\mathbf{J}_1 and \mathbf{J}_3) are excited with a significant contribution. From the TCM and their applications, it is known that the excitation of the resonant modes can give a reasonable impedance matching of the respective feeding port. In this example, mode \mathbf{J}_1 and mode \mathbf{J}_3 have a resonance at $f_{\text{res},J1} = 1.15$ GHz (#1) and at $f_{\text{res},J3} = 3.625$ GHz (#3) respectively. Since they are excited with a high purity, an impedance matching around the resonance frequencies can be observed, as depicted in Fig. 4-3.

4.6.2 Rectangular Plate

The rectangular plate is excited with an illuminating plane wave \mathbf{E}_{inc} polarized in x - and y -direction, as denoted in Fig. 4-4 a) and b). The first six characteristic modes (shown in Fig. 4-5) are calculated, as explained in Chapter 4.4. The eigenvalues of the first six characteristic modes are shown in Fig. 4-6. This

eigenvalue plot is common for planar structures. The eigenvalue of the capacitive modes \mathbf{J}_{1-5} starts from high negative values and converge toward zero. On the other side, the eigenvalue of the inductive mode \mathbf{J}_6 has a high positive eigenvalue at the low frequency, and converges with increasing frequency toward zero eigenvalue.

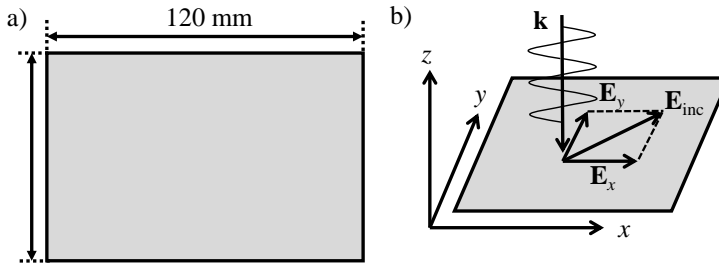


Fig. 4-4 Rectangular PEC plate placed in free space a). The plate is excited with a plane wave \mathbf{E}_{inc} polarized in x - and y -direction b). © IEEE 2016 [Saf16].

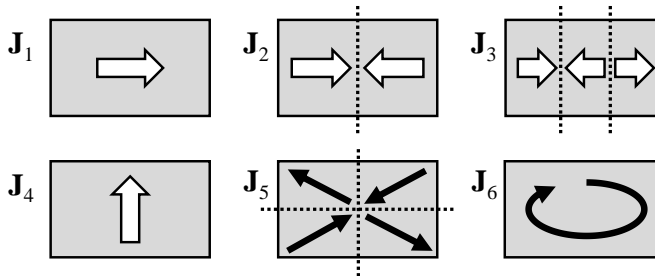


Fig. 4-5 Six significant characteristic modes \mathbf{J}_{1-6} of a rectangular PEC plate placed in free space.

In the frequency range observed ($1 \leq f [\text{GHz}] \leq 5$), five resonances can be found, listed in Table 4-1 and marked in Fig. 4-6 (#1 – #5). The lowest resonance is at $f_{\text{res},J1} = 1.1 \text{ GHz}$ (#1) and represents a half wavelength dipole mode in vertical direction. The next resonance (#2) of \mathbf{J}_2 represents the full wavelength dipole mode in vertical direction. On the same principle, modes \mathbf{J}_3 and \mathbf{J}_4 can be interpreted with respect to the surface current distribution. Mode \mathbf{J}_5

4. The Theory of Characteristic Modes

represents a quadrupole in free space with a resonance at $f_{\text{res},J5} = 3.3$ GHz. The inductive mode \mathbf{J}_6 is a magnetic dipole mode without a resonance in the observed frequency range.

The plane wave excites the full and half wave dipole modes ($\mathbf{J}_{1,3,4}$) with an alternating dominance, as can be observed in Fig. 4-7. In the low frequency range ($1 \leq f[\text{GHz}] \leq 2$) where the first mode \mathbf{J}_1 reveals a resonance (#1), a strong dominance can be observed. With increasing frequency, the vertical dipole mode \mathbf{J}_3 becomes more dominant in combination with the first mode \mathbf{J}_1 . The plane wave, which is polarized in vertical and horizontal directions, excites a surface current orientated in a similar direction. Above $f = 4$ GHz, mode \mathbf{J}_1 and \mathbf{J}_4 lose their dominance, and mode \mathbf{J}_3 becomes more significant. The total surface current distribution induced is similar to a 1.5 wavelength dipole mode along the major axis and, therefore, is similar to the surface current of mode \mathbf{J}_3 in Fig. 4-5. However, in the higher frequency range ($f > 4$ GHz), more modes are excited, and a clear dominance of isolated modes cannot be found. This behavior is typical for objects, which are larger than the wavelength.

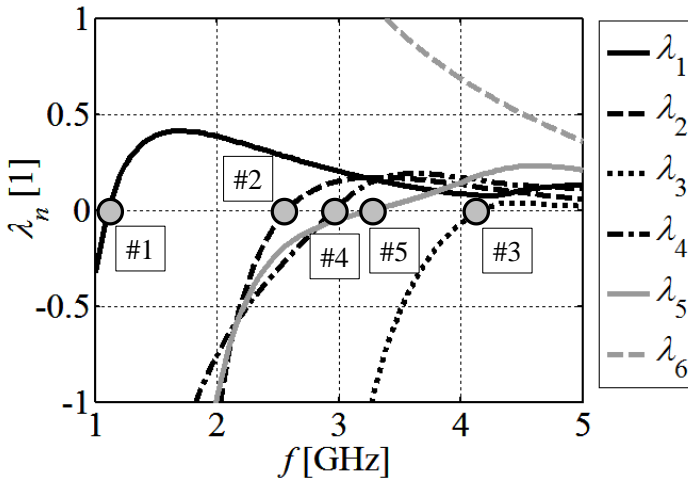


Fig. 4-6 First six eigenvalues of the modes shown in Fig. 4-5.

TABLE 4-1
 RESONANCE FREQUENCY OF THE CHARACTERISTIC MODES OF A RECTANGULAR PLATE.

	Mode	Resonance Frequency
#1	\mathbf{J}_1	1.10 GHz
#2	\mathbf{J}_2	2.55 GHz
#3	\mathbf{J}_4	3.00 GHz
#4	\mathbf{J}_5	3.30 GHz
#5	\mathbf{J}_3	4.10 GHz
	\mathbf{J}_6	None

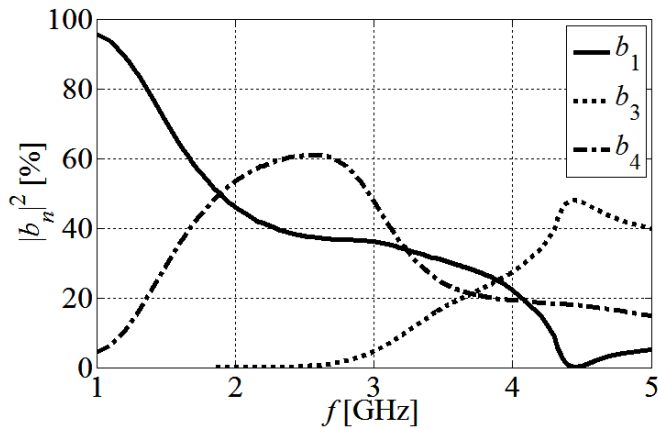


Fig. 4-7 Normalized coefficients of three significant modes of rectangular plate excited with a plane wave polarized in x - and y -direction. The eigenvalues and the normalized coefficients are tracked with the orthogonalization based algorithm as explained in Chapter 5. © IEEE 2016 [Saf16].

Chapter 5

Eigenvalue Tracking

¹The eigenvalue of the Characteristic Modes is an important parameter, which allows for an intuitive interpretation of the radiation mechanism in case of lossless PEC bodies. From the eigenvalue, other parameters are calculated, e.g., excitation coefficient or Q-factor, which are used for analysis and further optimizations. Therefore, continuous and differential eigenvalue curves are of high importance for the TCM analysis. The basic eigenvalue equation is defined in the frequency domain and, hence, the matrix (impedance matrix in case of PEC bodies) is calculated at isolated frequencies through the predefined frequency range. After the eigenvalue equation is solved, a sorting of the eigenvalues is required with an algorithm.

The problem in tracking the eigenvalue of a parameterized matrix is known from other scientific areas, e.g., signal processing [Aal85] or mathematics [Kal10]. Although tracking algorithms are available for specific scientific areas, none of these is suitable for the TCM in the form presented. In [Max10, Cap11, Kre12, Mie15, Rai11, Lud14, Che15], different concepts are presented

¹ The following chapter uses textual materials and figures from [Saf16] © *IEEE* 2016.

5. Eigenvalue Tracking

for the tracking of characteristic modes based on the surface current, far field and eigenvector correlation. The correlation-based tracking algorithms may be acceptable for specific structures, but, in general, they are either not stable or have other issues that restrict their applicability.

The correlation-based algorithms can fail if the gradient of a certain mode is high. This can happen if the geometry of the structure is complex or if reactive elements are used. In [Cap11], the author reports about an unavoidable effect that can occur while tracking the eigenvalues of the modes. The surface current distribution of specific modes changes drastically and appears unsymmetrically at isolated frequency points. This effect goes along with equal eigenvalues at certain frequency points [Bla07]. These modes are commonly denoted as *degenerated modes* and exert a strong influence on the common tracking algorithm. In common tracking algorithms, the degeneration becomes critical at frequencies, where the eigenvalues of different modes intersect.

5.1 Definition of the Tracking Problem

The problem to track the eigenvalues of modes over a wide frequency range is originated in the late 1990s and at the beginning of the millennium. With the increasing computing capability, more complex geometries (compared with wired structures) have been investigated, e.g., rectangular plate and fractal antenna. The eigenvalues of the characteristic modes have been used to find the natural resonance of the chassis wave modes and to derive simple equivalent circuits [Vai02]. The continuous eigenvalue curves of the modes are used to derive the values of the equivalent circuit elements, viz., inductor and capacitor.

The defined eigenvalues range is $-\infty < \lambda_n < +\infty$ and may be not appropriate to

demonstrate the capability of the tracking of modes, especially if the eigenvalue is close to zero or tends to infinity. Therefore, the so-called *characteristic angle* α_n is defined [New79]

$$\alpha_n = 180^\circ - \tan^{-1}(\lambda_n), \quad (5.1)$$

which maps the eigenvalue into the limited range of $90^\circ < \alpha_n < 270^\circ$. The special case where the eigenvalue is zero ($\lambda_n = 0$) the characteristic angle is mapped to $\alpha_n = 180^\circ$.

In order to demonstrate the general tracking problem, a simple rectangular strip — having the outer dimension of $120 \times 20 \text{ mm}^2$ — is investigated. In Fig. 5-1 a), the raw data and in Fig. 5-1 b), the sorted data are shown. It can be observed that the order of modes in Fig. 5-1 a) is incorrect. The use of a tracking algorithm corrects the characteristic angle, as it can be observed in Fig. 5-1 b).

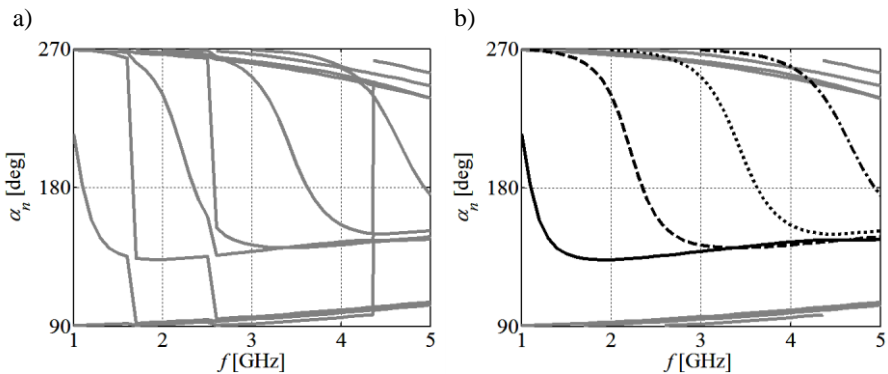


Fig. 5-1 Eigenvalues of a PEC strip having an outer dimension of $120 \times 20 \text{ mm}^2$. The raw data of the eigenvalues a) and sorted eigenvalues b) with a correlation based tracking algorithm. © IEEE 2016 [Saf16].

5.2 Correlation Based Eigenvalue Tracking

The correlation based tracking algorithms are widely used in TCM software

5. Eigenvalue Tracking

tools. The concept requires a quantity that can be correlated at all frequencies. Such quantities can be the eigenvectors \mathbf{J}_n , the far field \mathbf{E}_n or the surface current correlation of the modes. In the following, the principle is explained of how an automatic tracking can be applied with the three different quantities.

The concept to track the modes with a correlation-based algorithm is simple in realization. A correlation matrix is constructed, where the rows are related to frequency f_1 (\mathbf{J}_m) and the columns are related to the frequency f_2 (\mathbf{J}_n). The entries of the correlation matrix close to unity indicate the correct order of the modes. Since it is not possible to predict a high gradient of the eigenvalue, and, therefore a high gradient of any quantity, an adaptive frequency control is used to improve the tracking. Although this concept is basically known from other simulation tools, it has not been used for the tracking of modes known from available literature.

The principle of a correlation-based tracking algorithm (independent of the quantity chosen) is illustrated in Fig. 5-2. The algorithm can be summarized as follows. The modes \mathbf{J}_m at the initial frequency f_1 are calculated, preconditioned and stored in the memory for the next steps. The preconditioning is an important step, which helps keep the number of unsorted modes small. A typical strategy for a preconditioning is to filter the eigenvalues to be within a certain interval (e.g. $-100 \leq \lambda_n [1] \leq +100$). A different preconditioning technique is presented in [Cap11], where the modes are presorted and processed in a more advanced sorting algorithm. Thereafter, the modes \mathbf{J}_n at the following frequency step are calculated and preconditioned, using the same procedure. The correlation matrix $\rho_{m,n}$ between the modes is calculated and is used to search for the highest magnitude of a column. If the magnitude is high enough (in this case $|\rho_{m,n}| \geq 0.75$), the modes at the two frequencies can be ordered into the same mode number. In the other case, i.e., if the highest magnitude is less than

$|\rho_{m,n}| < 0.75$, the tracking has failed. In this case, the frequency f_2 is adjusted to be closer to f_1 and the procedure is repeated. In order to avoid the frequency f_2 to be too close to f_1 , the minimum bandwidth (10% of the defined frequency bandwidth BW) is tested. In case of $f_2 - f_1 < 0.1 BW$, the tracking has anyway failed; otherwise, the new frequency f_2 is set. After all modes are tracked, the initial frequency is $f_1 \leftarrow f_2$ and the next frequency is set $f_2 \leftarrow f_2 + BW$. These steps are repeated until the end frequency of the simulation is reached.

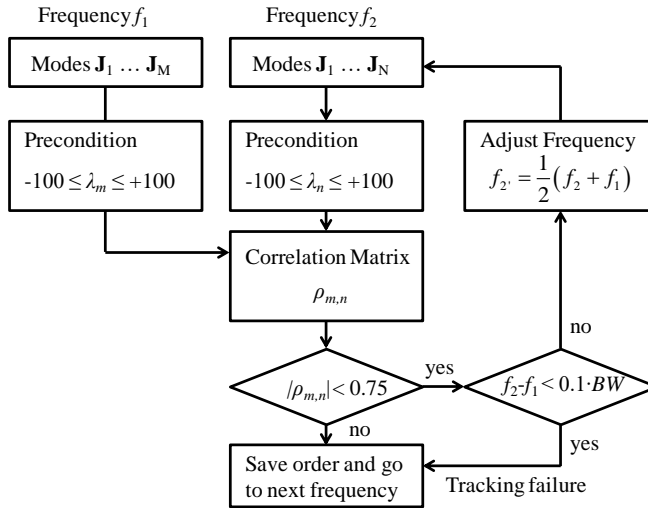


Fig. 5-2 Simple sketch of the correlation based tracking algorithm. © IEEE 2016 [Saf16].

The tracking with the correlation-based tracking algorithm can fail for certain reasons. Two modes can change the respective mode order, if the correlation alternates between low and high value within a single frequency step. Such observations can be made if the eigenvalue reveals a high gradient or the surface current mode alternate strongly. The common correlation-based tracking may not be able to distinguish between the two modes and these can be interpreted as identical modes and labeled accordingly. The strong surface current deformation is somehow related to the degenerated mode effect, and gives an

5. Eigenvalue Tracking

explanation of the appearance and disappearance of modes.

In the other case, where the eigenvalues exceed the defined range of $|\lambda_n| > 100$, the algorithm is not able to continue the tracking. In most cases, it might be sufficient to refine the frequency stepping or to redefine the eigenvalue range in order to improve the tracking. The tracking of higher order modes might require a higher mesh density, since they show more complex surface current distributions.

In the following, three different correlations are explained which can be used to track the characteristic modes.

5.2.1 Eigenvector Correlation

The eigenvector correlation — as described in [Max10, Cap11, Kre12] — is a basic method to track the modes over the frequency. This correlation $\rho_{m,n}$ is calculated with the eigenvector \mathbf{J}_n with:

$$\rho_{m,n} = \frac{(\mathbf{J}_m)^T \mathbf{J}_n}{|\mathbf{J}_m| \cdot |\mathbf{J}_n|}. \quad (5.2)$$

The eigenvector correlation is very sensitive to the change of the surface current modes \mathbf{J}_m and \mathbf{J}_n respectively. This — and the fact that the eigenvectors are strictly not orthogonal at the same frequency (please see (4.6)) — makes the eigenvector correlation more susceptible to wrong tracking, compared with other quantities. The orthogonality of certain eigenvectors, which can be observed for some examples, is random. Therefore, the eigenvector correlation is not preferred for the tracking in this form. However, a more advanced eigenvector correlation can be found in [Che15].

5.2.2 Far Field Correlation

The far field correlation requires an additional calculation step before the correlation matrix can be set. The far fields \mathbf{E}_m and \mathbf{E}_n of the modes have to be calculated numerically with a defined resolution (e.g. a resolution of 5° for the phi- and theta-component of the modal far field \mathbf{E}_n and \mathbf{E}_m). Owing to the usual normalization to unity ($1=0.5\langle\mathbf{J}_n,\mathbf{R}\mathbf{J}_n\rangle$), the far field correlation, in this case, is:

$$\rho_{m,n} = \frac{1}{2Z_{F0}} \iint_{S \rightarrow \infty} (\mathbf{E}_m)^* \mathbf{E}_n dA. \quad (5.3)$$

Under the assumption that the frequency difference between $\mathbf{E}_n(f_1)$ and $\mathbf{E}_m(f_1+\Delta f)$ is small, the correlation in (5.3) tends to unity. The modal far fields can be saved after the algorithm is finished and used for a modification of the tracking in an additional post-processing step, if required.

The additional far field calculation with a given resolution decreases the accuracy of the correlation (see Chapter 6.3 for detailed explanations). Therefore, this correlation is not discussed further, but detailed explanations and an advanced tracking algorithm can be found in [Mie15].

5.2.3 Surface Current Correlation

The surface current correlation is an advanced method to program a tracking algorithm in a similar way, as presented for the far field correlation. The real part of the impedance matrix \mathbf{Z} (for lossless PEC bodies) is used to calculate the correlation between two modes at different frequencies [Rai11, Lud14, Che15], with

$$\rho_{m,n} = \frac{1}{2} \langle \mathbf{J}_m, \mathbf{R}\mathbf{J}_n \rangle. \quad (5.4)$$

5. Eigenvalue Tracking

In a similar manner, as explained earlier, the correlation is close to unity, if the frequency variation is small. The correlation in (5.4) is more accurate compared with other quantities, since no other calculation steps (such as the far field calculation) are required.

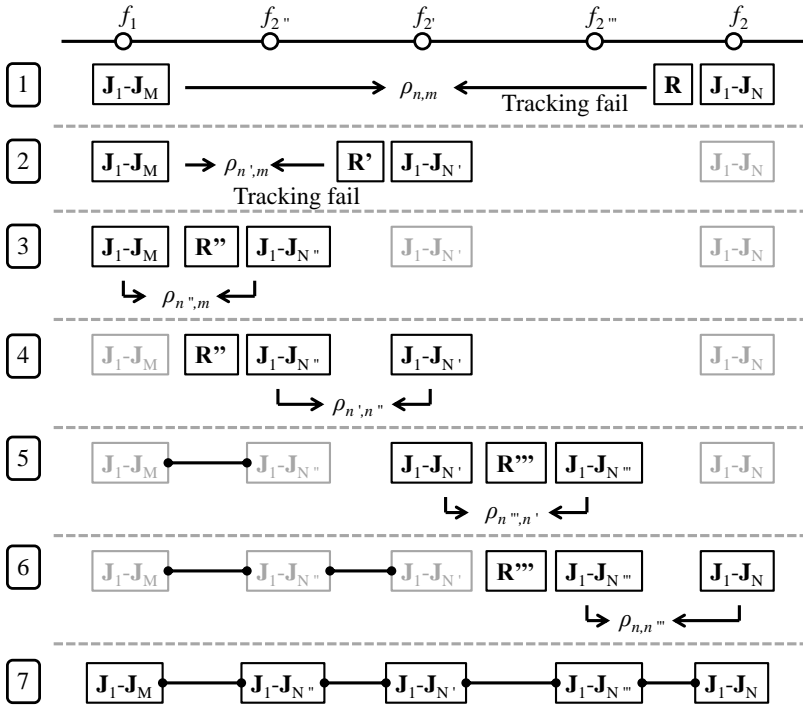


Fig. 5-3 Schematic of the correlation based tracking algorithm with the surface current correlation. The scheme shows the principle of the frequency control. The areas that are separated with dashed gray lines denote the memory allocated for the modes \mathbf{J}_n and for the matrix \mathbf{R} . © IEEE 2016 [Saf16].

An optimal algorithm requires an intelligent frequency control to avoid the need to save more than one matrix \mathbf{R} . Since the matrix \mathbf{R} can be large, a frequency control helps use the allocated memory efficiently. The concept to store one matrix \mathbf{R} at all frequencies is sketched in Fig. 5-3. If the correlation matrix in Fig. 5-3 reveals a not trackable mode (Step 1), the frequency is decreased

(Step 2), and the correlation matrix is recalculated. Under the assumption that the tracking has failed again, the frequency is reduced for the second time (Step 3). Now, the tracking is successful, and the modes between the f_1 and f_2'' can be ordered. The same matrix \mathbf{R}'' can be used to track the modes between the f_2'' and f_2' (Step 4). Next, a tracking is required between f_2' and f_2 without the need to recalculate the matrix \mathbf{R} again. In order to continue the tracking, the impedance matrix \mathbf{R}''' at frequency f_2''' is calculated and used to track from f_2' to f_2''' and from f_2''' to f_2 (Steps 5-6). In the ideal case, the tracking is successful, and a clear mode order from f_1 to f_2 (Step 7) can be defined.

This method requires a sufficient mesh density of the structure and a minimum frequency step size to enable the correct tracking, even for higher order modes.

5.3 Correlation-Based Eigenvalue Tracking – Example

The combination of the correlation-based tracking, as sketched in Fig. 5-2, and the frequency control in Fig. 5-3, gives a powerful and robust algorithm. In order to demonstrate the correlation-based eigenvalue tracking, a generic example (rectangular plate) is investigated. Such an example is typically used, as it can be easily reproduced by other TCM software tools. The rectangular plate is excited with a plane wave polarized in x - and y - direction, as denoted in Fig. 4-4.

The results of the correlation-based tracking algorithm for the far field and surface current correlation is shown in Fig. 5-4, Fig. 5-5 and Fig. 5-6. The bandwidth is 50 MHz for both tracking methods. Notice that, the correlation-based tracking algorithm adjusts the frequency step size in an adaptive manner, depending on the respective correlations between the modes. The bandwidth is reduced through the tracking, if at least one mode is difficult to track, and increased up to the initial bandwidth, if the modes are tracked successfully.

5. Eigenvalue Tracking

The tracking of the rectangular plate (please see Fig. 5-4) shows, at first appearance, reasonable characteristic angle curves α_n with the far field and surface current correlation. However, it seems that the tracking has failed for mode $J_{1,4}$ in Fig. 5-4 (please see the zoomed area).

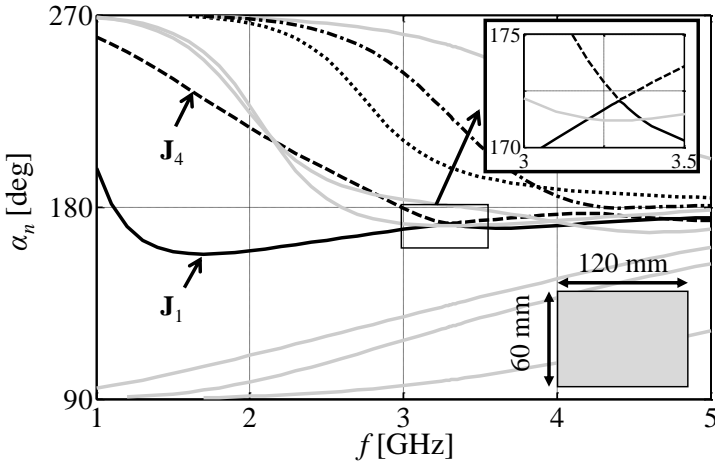


Fig. 5-4 Characteristic angles α_n of 10 modes for a rectangular plate tracked with the correlation-based algorithm. The results achieved with the far field and the surface current correlation are equal. © IEEE 2016 [Saf16].

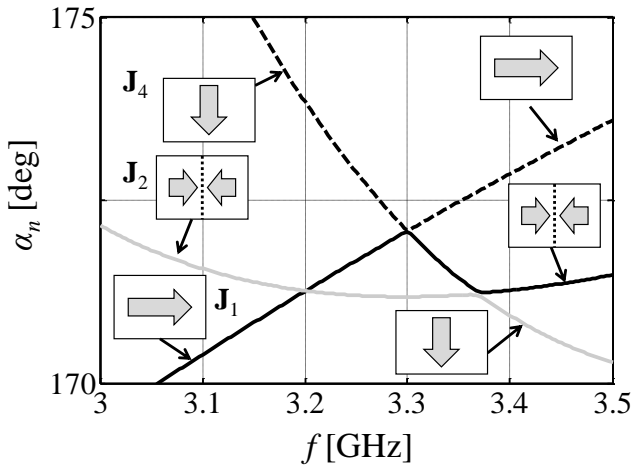


Fig. 5-5 Recalculated characteristic angles α_n of the rectangular plate (zoomed area in Fig. 5-4) with 180 frequency points. © IEEE 2016 [Saf16].

The wrong tracking of mode $\mathbf{J}_{1,4}$ in the zoomed area in Fig. 5-4 is investigated in detail. For that, the tracking algorithm is repeated with a high frequency resolution (2.76 MHz initial bandwidth) in the new frequency range $3 \leq f [\text{GHz}] \leq 3.5$. The result of this high-resolution tracking is shown in Fig. 5-5. The tracking somehow reveals a different mode order, compared to Fig. 5-4. Mode \mathbf{J}_2 is tracked with a different mode order above 3.35 GHz (please compare Fig. 5-5 with the zoomed area in Fig. 5-4). In order to understand why the tracking has failed for the different frequency resolutions, the surface current modes $\mathbf{J}_{1,4}$ around $f = 3.3$ GHz are investigated as an example.

The surface current distribution $\mathbf{J}_{1,4}$ and the respective eigenvalues $\lambda_{1,4}$ are shown in Fig. 5-6 for different frequencies around $f \approx 3.3$ GHz. It can be observed that the surface current modes $\mathbf{J}_{1,4}$ show a strong deformation within the frequency range ($3.222 \leq f [\text{GHz}] \leq 3.317$). Furthermore, the two modes $\mathbf{J}_{1,4}$ swap around $f = 3.3$ GHz with respect to the surface current distribution. The eigenvalue distance $|\lambda_1 - \lambda_4|$ can be used to quantify the swapping of modes. The same effect can be observed for other modes in the entire frequency range (e.g. at $f = 3.2$ GHz and $f = 3.36$ GHz in Fig. 5-5 or at $f = 2.2$ GHz in Fig. 5-4). These incorrect modes are called *degenerated modes*, and they harm the tracking in general.

Depending on the current simulation, one can hit the exact frequency where two incorrect modes swap their surface current distribution (e.g. in Fig. 6 at $f = 3.3$ GHz) or omit at random. For this reason, the correlation-based tracking algorithm can give different tracking results, depending on the initial frequency resolution, for the same structure and the same mesh density.

5. Eigenvalue Tracking

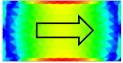
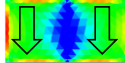

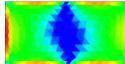

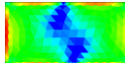
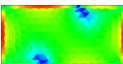
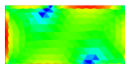
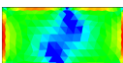
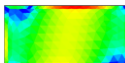
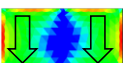
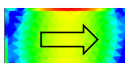
Frequency	Mode \mathbf{J}_1	λ_1	$ \lambda_1 - \lambda_4 $	λ_4	Mode \mathbf{J}_4
3.222 GHz		0.1504	0.0346	0.1158	
3.289 GHz		0.1407	0.0045	0.1362	
3.297 GHz		0.1395	0.0012	0.1383	
3.300 GHz		0.1394	0.0006	0.1388	
3.303 GHz		0.1399	0.0013	0.1386	
3.317 GHz		0.1432	0.0065	0.1367	

Fig. 5-6 Incorrect surface current of two modes $\mathbf{J}_{1,4}$ at different frequency points. The black arrows denote the effective surface current distribution. © *IEEE* 2016 [Saf16].

5.4 Degenerated Modes

The correlation-based mode tracking algorithm reveals an effect that occurs if two modes have nearly equal eigenvalues. This effect is related to the generalized eigenvalue decomposition of the impedance matrix \mathbf{Z} . From the eigenvalue decomposition of a matrix, it is known that double eigenvalues can exist with two respective orthogonal eigenvectors. In this special case, the eigenvectors of the two identical eigenvalues are not clearly defined. In order to explain this fact, let us assume that two modes $\mathbf{J}_{a,b}$ exist with identical eigenvalues $\lambda_a = \lambda_b$. The two modes $\mathbf{J}_{a,b}$ fulfill the eigenvalue equation (4.1) with the two eigenvalues $\lambda_{a,b}$ with:

$$\mathbf{X}(\mathbf{J}_a + \mathbf{J}_b) = \lambda_a \mathbf{R}(\mathbf{J}_a + \mathbf{J}_b) = \lambda_b \mathbf{R}(\mathbf{J}_a + \mathbf{J}_b) . \quad (5.5)$$

Therefore, any combination of the two modes $\mathbf{J}_{a,b}$ fulfills the generalized eigenvalue equation in the same way:

$$\mathbf{X}(\kappa_a \mathbf{J}_a + \kappa_b \mathbf{J}_b) = \lambda_a \mathbf{R}(\kappa_a \mathbf{J}_a + \kappa_b \mathbf{J}_b) = \lambda_b \mathbf{R}(\kappa_a \mathbf{J}_a + \kappa_b \mathbf{J}_b) . \quad (5.6)$$

where $\kappa_{a,b}$ are real-valued weighting coefficients.

From (5.6), it is clear that the weighted summation of \mathbf{J}_a and \mathbf{J}_b leads to an infinite number of possible solutions. In order to find a unique solution for (5.6), the orthogonality must be exploited. The aim is now to find two new modes ($\mathbf{J}_{a',b'}$) that are orthogonal and that can be substituted in (5.6). The new two modes are now

$$\mathbf{J}_{a'} = \kappa_a \mathbf{J}_a + \kappa_b \mathbf{J}_b \quad (5.7)$$

and

$$\mathbf{J}_{b'} = \nu_a \mathbf{J}_a + \nu_b \mathbf{J}_b . \quad (5.8)$$

In (5.8), $\nu_{a,b}$ are real-valued weighting coefficients similar to $\kappa_{a,b}$ in (5.7). The new modes $\mathbf{J}_{a',b'}$ must be real and orthogonal with respect to each other and with respect to the remaining modes. By exploiting (5.4) and (5.6) in (4.1), a generally valid condition for the new real coefficients can be derived:

$$\kappa_a \nu_a + \kappa_b \nu_b = 0 . \quad (5.9)$$

Although (5.9) is valid even for complex coefficients a solution with real coefficients can be found. The condition (5.9) can be used to find a solution based on a single parameter γ . The general solution is

$$\mathbf{J}_{a'} = \underbrace{\cos(\gamma)}_{\kappa_a} \mathbf{J}_a + \underbrace{\sin(\gamma)}_{\kappa_b} \mathbf{J}_b \quad (5.10)$$

and

$$\mathbf{J}_{b'} = \underbrace{-\sin(\gamma)}_{v_a} \mathbf{J}_a + \underbrace{\cos(\gamma)}_{v_b} \mathbf{J}_b. \quad (5.11)$$

The angle γ describes a rotation of the initial modes $\mathbf{J}_{a,b}$ in the respective subspace as depicted in Fig. 5-7.

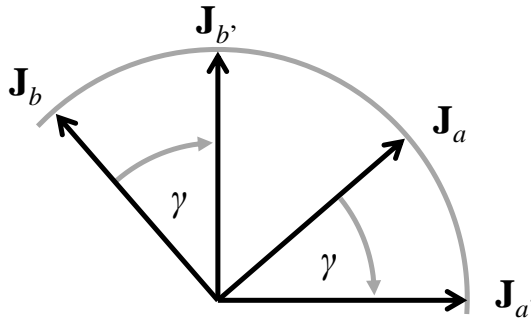


Fig. 5-7 Illustration of the degenerated modes. The initial eigenvectors \mathbf{J}_a and \mathbf{J}_b are rotated by the angle γ to get the true eigenvectors $\mathbf{J}_{a'}$ and $\mathbf{J}_{b'}$. © IEEE 2016 [Saf16].

The effect of the degenerated modes exerts a high influence on the eigenvalue tracking. This effect is emphasized in an incorrect mode order after the tracking algorithm is used. However, the effect can have another appearance, which is explained in Fig. 5-8. The normalized coefficient b_n , which determines the power the mode contributes to the overall input power, is shown below the eigenvalue tracking of the rectangular plate. It can be observed that the normalized coefficient b_n shows a conspicuous behavior near the equal eigenvalue points (at $f = 3.3$ GHz, $f = 3.9$ GHz and $f = 4.7$ GHz). A high point-wise deviation from the expected curves indicates the proposed effect. The strong deformation of the incorrect surface current modes affects the calculation of the weighting coefficient a_n and the normalized coefficients b_n . It is noticeable that the normalized coefficients b_n are incorrect, although the eigenvalue tracking is correct (please see Fig. 5-8 at $f = 3.9$ GHz and $f = 4.7$ GHz).

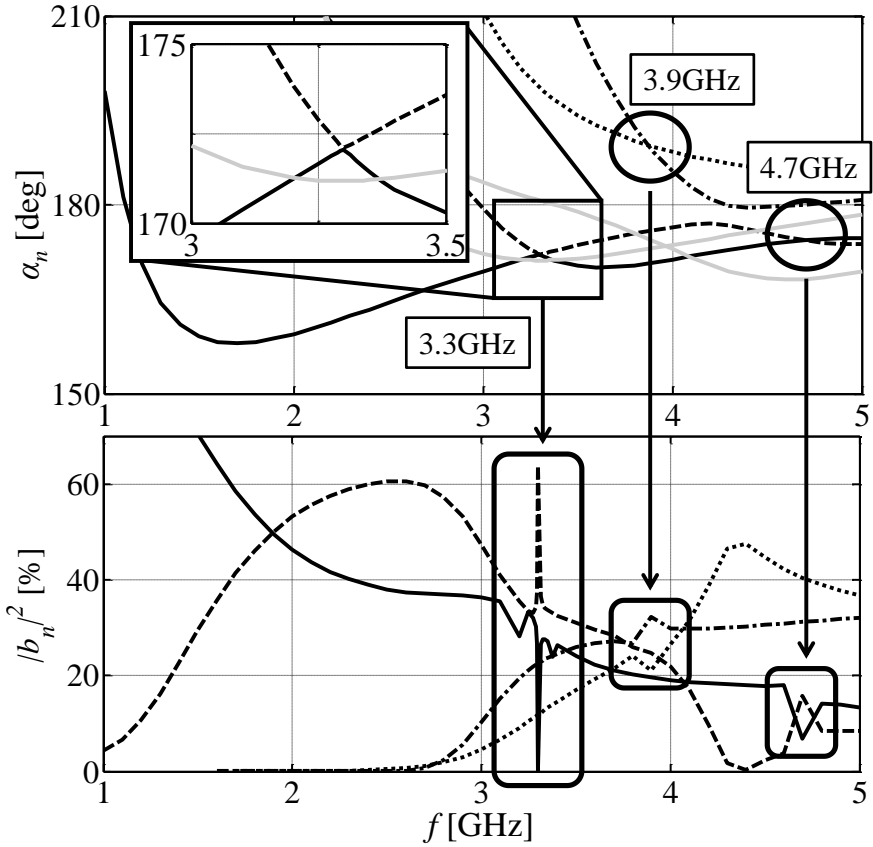


Fig. 5-8 Characteristic angles α_n and the normalized coefficients b_n for a rectangular plate (excited by a plane wave polarized in x - and y -direction). The two plots illustrate the degenerated mode effect. © IEEE 2016 [Saf16].

One possible solution to overcome the degenerated mode effect is to avoid the mode computation at frequencies where two modes have nearly the same eigenvalue. This solution is not practicable, since those equal eigenvalue frequencies increase rapidly with the number of modes tracked. Furthermore, the omitted frequencies could distort the tracking algorithm and give insufficient results. For these reasons, the proposed solution is not favorable.

An alternative solution for the degenerated mode effect is to use the modes at

the previous frequency values as a condition to set up the angle γ and recalculate the eigenvectors. Based on this idea, a new tracking algorithm is derived, which enables a rotation of the eigenvectors. For that, the eigenvectors at the previous frequency are used as a starting vector for the realignment with a modified Arnoldi-orthogonalization (the origin method can be found in [Arn51]). The orthogonalization method and the new tracking algorithm are explained in the next section.

5.5 Orthogonalization-Based Eigenvalue Tracking

The orthogonalization-based eigenvalue tracking is an iterative algorithm to find nearly orthogonal eigenvectors from a given set of starting vectors. Under the assumption that the starting vectors are already nearly orthogonal to each other, the algorithm requires a few steps to recalculate the desired *true* eigenvectors. In the following, the new concept is described to realign the characteristic modes.

First of all, the initial characteristic modes \mathbf{J}_m at the start frequency f_1 are defined as the starting vector for the new algorithm. The initial modes are assumed to be the *true* eigenvectors needed to decompose the surface current at the first frequency point. Next, the modes \mathbf{J}_i are calculated at the next frequency f_2 and the best decomposition of the initial modes \mathbf{J}_m , which are found at the initial frequency f_1 with

$$\mathbf{J}_m = \sum_{i=1}^N a_i \mathbf{J}_i = \underbrace{[\mathbf{J}_1 \quad \cdots \quad \mathbf{J}_N]}_{\mathbf{A}} \cdot \begin{bmatrix} a_1 \\ \vdots \\ a_N \end{bmatrix}. \quad (5.12)$$

The real coefficients a_i in (5.12) can be found with the least mean square approximation:

$$\begin{bmatrix} a_1 \\ \vdots \\ a_N \end{bmatrix} = (\mathbf{A}^T \mathbf{A})^{-1} (\mathbf{A}^T \mathbf{J}_m) . \quad (5.13)$$

In order to use (5.13), a condition is needed to set the number of modes used. The eigenvalue range $(-100 \leq \lambda_i [1] \leq +100)$ is used to identify the modes required for the new algorithm.

The magnitude of the coefficients a_i is used to find those modes that are not included in matrix \mathbf{A} (indicated with a small a_i in (5.13)). By scanning the coefficients a_i , the number of modes tracked can be changed through the tracking program. This step allows one to start or end the tracking of a single mode. The real coefficients a_i are searched for the highest magnitude value. If the highest magnitude value is smaller than e.g. $|a_i| < 0.6$, the initial mode \mathbf{J}_m exceeds the defined range (e.g. $|\lambda_m| > 100$), and is not tracked further. Otherwise, the initial mode \mathbf{J}_m can be identified in the new set of modes \mathbf{J}_i . The decomposition of the initial modes is used to define the starting vector for the iterative procedure for the modified Arnoldi-Orthogonalization:

$$\mathbf{J}_n = \mathbf{A} \cdot [a_1 \quad \cdots \quad a_N]^T . \quad (5.14)$$

In the next step the impedance matrix \mathbf{Z} at the frequency f_2 is used for the orthogonalization method as follows:

$$\mathbf{J}_n = \mathbf{J}_n - \sum_{\substack{w=1 \\ w \neq n}}^N \Psi_{w,n} \operatorname{Re} \left\{ \frac{\langle \mathbf{J}_w, \mathbf{Z} \mathbf{J}_n \rangle}{\langle \mathbf{J}_w, \mathbf{Z} \mathbf{J}_w \rangle} \right\} \mathbf{J}_w , \quad (5.15)$$

where $\Psi_{w,n}$ controls the length of the eigenvector \mathbf{J}_w . Since the new orthogonalized eigenvectors \mathbf{J}_n must be real, the parameter $\Psi_{w,n}$ is real, and the real part of the complex matrix \mathbf{Z} is used.

5. Eigenvalue Tracking

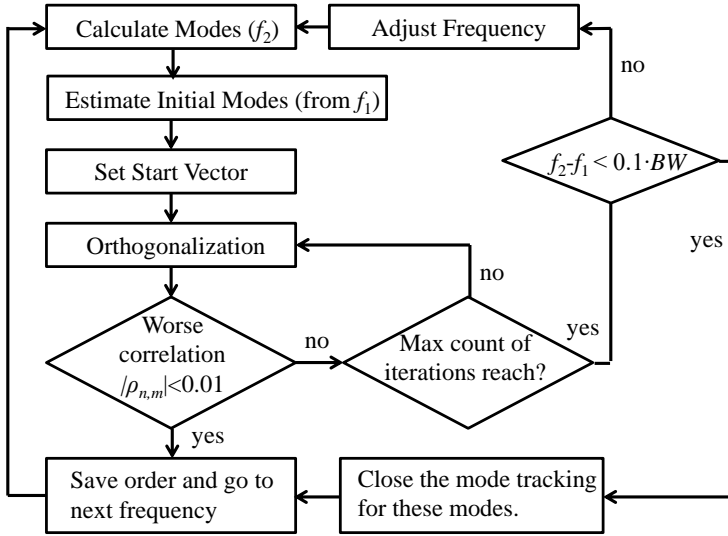


Fig. 5-9 Schematic sketch of the orthogonalization-based algorithm. © IEEE 2016 [Saf16].

The step width $\Psi_{w,n}$ can be set by the imaginary part of the complex matrix with:

$$\Psi_{w,n} = e^{-\left| \operatorname{Im} \left\{ \frac{\langle \mathbf{J}_w, \mathbf{Z}_n \rangle}{\langle \mathbf{J}_w, \mathbf{Z}_w \rangle} \right\} \right|} . \quad (5.16)$$

The iteration (5.15) is repeated until all modes \mathbf{J}_n are orthogonal to each other with respect to the power budget. The worst correlation between the modes is used as an indicator to stop the iteration. If the worst correlation is smaller than $|\rho_{n,m}| < 0.01$, the procedure has finished, and the same procedure is used for the next frequency until the last frequency value has been reached. If the iteration reaches a predefined count (e.g. 500 steps), the procedure is stopped and the current frequency f_2 is reduced similarly to the frequency control in the correlation based algorithm. In order to avoid a too small bandwidth, the same query — as explained in Chapter 5.2 — is used. The minimum band width ($f_2 - f_1 < 0.1 BW$) condition is used to break up the tracking for certain modes.

A schematic sketch of the algorithm is shown in Fig. 5-9.

After the procedure has finished, the eigenvectors are normalized to radiate a unit power ($1=0.5\langle\mathbf{J}_n,\mathbf{R}\mathbf{J}_n\rangle$) and the eigenvalues are recalculated with:

$$\lambda_n = \frac{\text{Im}\{\langle\mathbf{J}_n,\mathbf{Z}\mathbf{J}_n\rangle\}}{\text{Re}\{\langle\mathbf{J}_n,\mathbf{Z}\mathbf{J}_n\rangle\}}. \quad (5.17)$$

The main advantage of the orthogonalization-based tracking algorithm is the fact that a new set of modes is calculated with the condition of minimal change in the modal surface current distribution. The comparison between the commonly used mode calculation and the new presented algorithm shows that the new *true* modes are slightly different, compared with the original modes. However, the new set of modes fulfills all conditions defined by the TCM, and these can be used for the antenna design without restrictions.

The disadvantage of the new algorithm is the slow convergence of the main orthogonalization in (5.15). The algorithm has to complete the full count of iteration steps until it recognizes the failure at the current frequency. Only after these steps can the frequency be adjusted. For these reasons, the algorithm requires more time to track the modes, compared with the correlation-based tracking algorithm.

5.6 Orthogonalization-Based Eigenvalue Tracking – Example

In this section, the proposed orthogonalization-based eigenvalue tracking algorithm is discussed on two examples with increasing complexity. In the first example a rectangular plate is discussed. The same example is used in Chapter 4.6.2 to introduce the TCM. In the second example, a fractal antenna — placed

5. Eigenvalue Tracking

over an infinite size ground plate — is investigated to demonstrate the capability and the limitation of the proposed algorithm.

5.6.1 Rectangular Plate

The rectangular plate has the outer dimension of $120 \times 60 \text{ mm}^2$ and is placed in the x/y -plane, as denoted in Fig. 4-4. A plane wave polarized in x - and y -direction excites a limited number of modes on the surface. The result of the eigenvalue tracking with the new orthogonalization-based tracking algorithm is shown in Fig. 5-10.

The eigenvalue curves in Fig. 5-10 and the normalized coefficients in Fig. 5-11 are reasonable in the entire frequency range. The effect of the degenerated modes is avoided. The tracking between modes \mathbf{J}_1 and \mathbf{J}_4 — that failed in the correlation based tracking algorithm (please see Fig. 5-8) — is now correct. Even a simulation with a high count of frequency points yields the same result (see the zoomed area in Fig. 5-10).

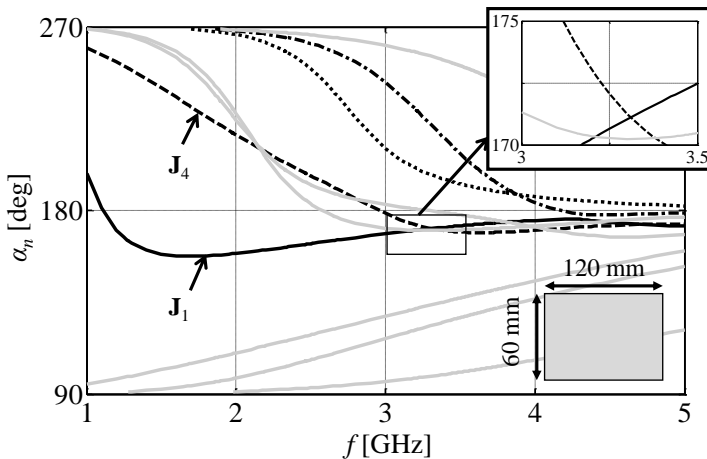


Fig. 5-10 The characteristic angles α_n for a rectangular plate tracked with the orthogonalization-based tracking algorithm. © IEEE 2016 [Saf16].

The recalculated characteristic modes reveal a minimized alternation with respect to the surface current distribution, compared to the commonly used correlation-based tracking algorithm. Therefore, the new algorithm is not only a tracking algorithm of eigenvalues, but a new method to calculate the characteristic modes. The new set of modes is orthogonal — as demanded in the basic theory — and, hence, the new eigenvectors are the characteristic modes initially introduced in [Har71a] and in Chapter 4.

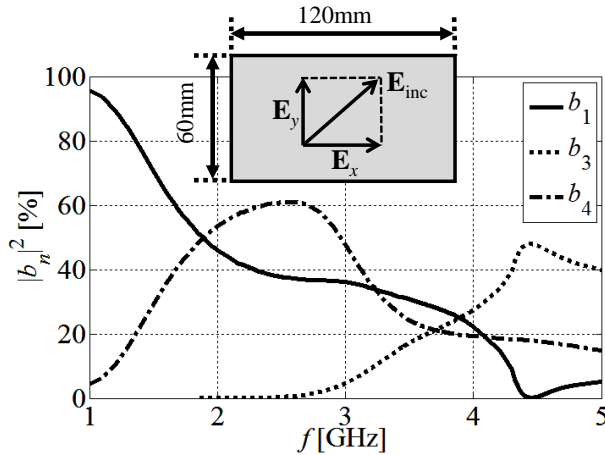


Fig. 5-11 The normalized coefficient b_n for a rectangular plate tracked with the orthogonalization based tracking algorithm. © IEEE 2016 [Saf16].

5.6.2 Fractal Antenna over an Infinite Size Ground Plane

The fractal antenna, placed over the infinite size ground plate, is used to demonstrate the capability and the limitation of the orthogonalization-based eigenvalue tracking algorithm. A similar example is used in [Cap11] to demonstrate the degenerated mode effect. The outer dimension of the fractal antenna is $102 \times 60 \times^2$ and the height over the ground plane is $h = 10$ mm. A small strip is added between the antenna and the ground plane.

The tracking result with the orthogonalization-based tracking algorithm is

5. Eigenvalue Tracking

shown in Fig. 5-12. It can be observed that the modes are tracked accurately in the observed frequency range. However, the tracking algorithm can fail, as it can be observed for the high inductive (with $\alpha_n \approx 90^\circ$) modes above $f > 2.8$ GHz. The orthogonalization can fail, if the number of modes used increases and the eigenvalue is large. Owing to the iterative procedure, any mistake made will affect further calculations and could be responsible for wrong tracked modes. The other disadvantage of the new algorithm is the overall time consumption. Compared to the robust surface current correlation-tracking algorithm, the new algorithm requires more time to recalculate the eigenvectors and to set the right order. In the special case, if one mode falls into the defined eigenvalue range ($|\lambda_m| > 100$) which was not tracked previously, the algorithm needs more iteration steps to orthogonalize the eigenvectors. The time required and the limited number of modes that can be tracked up to a certain frequency give the limitation of the new algorithm.

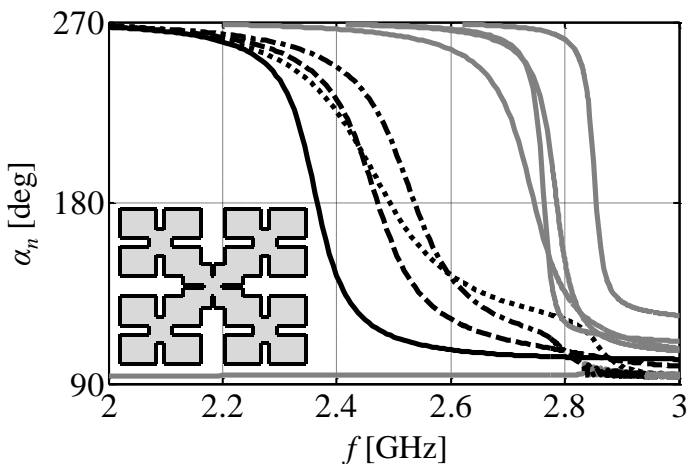


Fig. 5-12 Eigenvalue tracking of a fractal antenna placed over an infinite size ground plane. The distance between the fractal antenna and ground plane is $h = 10$ mm. The initial frequency step is 50 MHz. The fractal antenna is discretized in 2088 RWG basis functions. The main and higher order modes are respectively denoted in black and gray curves. A similar example has been investigated in [Cap11]. © IEEE 2016 [Saf16].

Chapter 6

Source Reconstruction

²Meanwhile, it is widely accepted that in terms of small terminals, the current distribution on the terminal chassis itself can play a significant role for the entire antenna performance. It has been shown in [Man01] and [Vai02] that in case of mobile phones, especially in low band operation, dominant modes are mainly affected by the overall dimensions of the chassis rather than by complex geometrical details of the terminal or the antenna element itself. Therefore, a profound understanding of the current distribution on the terminal chassis, respectively the PCB, is a key aspect in the design of novel antenna solutions.

Typically, the characteristic modes are calculated numerically using the MoM [Har93]. The MoM is well suited, because it is based on an impedance matrix (in case of PEC bodies), which allows for a direct calculation of the coupling between different current elements of the structure. On the other hand many state-of-the-art software tools used for antenna design utilize grid-based methods such as the FDTD (Finite Difference Time Domain) method. For such

² The following chapter uses textual materials and figures from [Saf13] © *IEEE* 2013.

tools, a direct calculation of the characteristic modes is not easily possible.

The TCM analysis of the real complex structure can be difficult in practice. In some cases, it might be sufficient to analyze simplified structures carrying almost the same significant modes, i.e., describe the main radiation mechanism of the complex structure sufficiently to draw simple conclusions.

This chapter presents a source reconstruction with a simplified geometry using two methods. The significant modes are extracted from the simplified structure and used to give an explanation of how the mounted antenna works in the presence of a finite size ground plate.

6.1 Far Field Calculation

The far field calculation of a known vector and scalar potential is well-known and available in literature. Two equations can be used, as described in brief in the following.

The scattering equation (2.2) is a basic formula to calculate the scattering electric field \mathbf{E}_s in any location in free space with

$$\begin{aligned} \mathbf{E}_s(\mathbf{r}) = & -j\omega\mu \iint_S \mathbf{J}(\mathbf{r}') \frac{e^{-jk|\mathbf{r}-\mathbf{r}'|}}{4\pi|\mathbf{r}-\mathbf{r}'|} dS' \\ & - \nabla \left(\frac{-1}{j\omega\epsilon} \iint_S \nabla \cdot \mathbf{J}(\mathbf{r}') \frac{e^{-jk|\mathbf{r}-\mathbf{r}'|}}{4\pi|\mathbf{r}-\mathbf{r}'|} dS' \right). \end{aligned} \quad (6.1)$$

Thus, Equation (6.1) is valid in the near and far field of the PEC body.

From (6.1), a second formula can be derived, which is valid only in the far field region. For this, the common far field approximation is used in (6.1), as explained in detail in [Bal05, pp908] to derive a simplified equation:

$$\mathbf{E}_s(\mathbf{r}) = -\frac{j\omega\mu}{4\pi} \frac{e^{-jkr}}{r} \left[\iint_S (\mathbf{J}(\mathbf{r}') - (\mathbf{J}(\mathbf{r}') \cdot \mathbf{n}) \cdot \mathbf{n}) e^{jk\mathbf{n}\mathbf{r}'} dS \right], \quad (6.2)$$

where \mathbf{n} is the unit vector from the source point \mathbf{r}' to the observation point \mathbf{r} .

6.2 Correlation of the Characteristic Modes

The correlation between the modal far field and the total radiated far field can be used as a testing procedure to predict the mode contribution for the specific excitation. It describes the similarity of two vector fields (\mathbf{E}_α and \mathbf{E}_β) by their spatial convolution over the infinite envelope:

$$\rho_{\alpha,\beta} = \frac{\frac{1}{2Z_0} \iint_{S' \rightarrow \infty} \mathbf{E}_\alpha \cdot \mathbf{E}_\beta^* dS}{\sqrt{\frac{1}{2Z_0} \iint_{S' \rightarrow \infty} |\mathbf{E}_\alpha|^2 dS} \sqrt{\frac{1}{2Z_0} \iint_{S' \rightarrow \infty} |\mathbf{E}_\beta|^2 dS}}. \quad (6.3)$$

The correlation between the total electric far field \mathbf{E} and the electric far field of a certain characteristic mode \mathbf{E}_n can be interpreted as a measurement of how strongly this mode contributes to the entire far field:

$$\begin{aligned} \rho_{\text{total},n} &= \frac{\frac{1}{2Z_0} \iint_{S' \rightarrow \infty} \mathbf{E} \cdot a_n^* \mathbf{E}_n^* dS}{\sqrt{\frac{1}{2Z_0} \iint_{S' \rightarrow \infty} |\mathbf{E}|^2 dS} \sqrt{\frac{1}{2Z_0} \iint_{S' \rightarrow \infty} |a_n \mathbf{E}_n|^2 dS}} \\ &= \frac{\frac{1}{2Z_0} \iint_{S' \rightarrow \infty} \mathbf{E} \cdot a_n^* \mathbf{E}_n^* dS}{\sqrt{P_{\text{rad}}} \cdot |a_n|} \\ &= \frac{1}{2Z_0} \iint_{S' \rightarrow \infty} \frac{1}{\sqrt{P_{\text{rad}}}} \mathbf{E} \cdot \frac{a_n^*}{|a_n|} \mathbf{E}_n^* dS. \end{aligned} \quad (6.4)$$

The coefficient a_n in (6.4) simply cares for the consistency of the units and can

6. Source Reconstruction

be set to unity:

$$\frac{a_n^*}{|a_n|} = 1. \quad (6.5)$$

Now, Equation (6.4) yields:

$$\rho_{\text{total},n} = \frac{1}{2Z_0} \oint\!\!\!\oint_{S' \rightarrow \infty} \frac{1}{\sqrt{P_{\text{rad}}}} \mathbf{E} \cdot \mathbf{E}_n^* dS = \sum_m \frac{a_m}{\sqrt{P_{\text{rad}}}} \underbrace{\frac{1}{2Z_0} \oint\!\!\!\oint_{S' \rightarrow \infty} \mathbf{E}_m \cdot \mathbf{E}_n^* dS}_{=0 \forall (m \neq n)}. \quad (6.6)$$

By exploiting the orthogonality of the modes (6.6) can be simplified in such a way that the integral becomes zero for $m \neq n$.

$$\frac{1}{2Z_0} \oint\!\!\!\oint_{S' \rightarrow \infty} \mathbf{E}_m \cdot \mathbf{E}_n^* dS = \delta_{nm}. \quad (6.7)$$

Thus the correlation reduces to a single term for $n = m$:

$$\rho_{\text{total},n} = \frac{a_n}{\sqrt{P_{\text{rad}}}} = \frac{a_n}{\sqrt{P_{\text{rad}}}} = b_n. \quad (6.8)$$

Eq. (6.7) shows that the correlation between the total radiated far field and the n -th characteristic mode is actually represented by the normalized coefficient b_n . Note that the terms $|b_n|^2$ are equal to the percentage each mode contributes to the total radiated power P_{rad} , as denoted in (4.12).

6.3 Reconstruction of the Modal Sources

Based on the above considerations, two methods are derived to reconstruct an approximation for the modal weighting factors of a simplified structure from the total radiated far field of the actual antenna. As explained above, this is based on the assumption that the actual (complex) antenna contains almost the same modes as the simplified structure, but these might have different

weighting coefficients due to the different coupling structure. However, the assumption made for the simplified structure is in any case a best guess and the method presented proves whether it is sufficiently correct. In case it is not correct, this is indicated by an incorrect power budget, and, in this case, the simplified structure has to be remodeled.

The first method is called the “Scalar-Method” as it is directly based on the correlation in (6.6) and the assumption that (4.4) and (6.7) are equal due to the orthogonality of the current modes and the linear operator \mathbf{L} that links these modes to the far field modes. As will be shown later, due to numerical inaccuracy, this is not exactly true. In order to compensate for this inaccuracy, a second method, called the “Matrix-Method” is derived.

6.3.1 *Scalar Method*

First, the actual (complex) antenna is modeled using the FDTD-based commercial EM software Empire XPU [EMP]. As a result, the entire far field \mathbf{E} of the antenna is calculated. Then, a simplified structure is modeled using our in-house MoM-based software. As a result the characteristic current modes \mathbf{J}_n and the related far field modes \mathbf{E}_n are obtained for the simplified structure. Assuming that the radiation mechanism of both structures — the complex one and the simplified one — is essentially based on the same modes, the correlation of the total far field of the complex structure is calculated with the different modes of the simplified structure. This leads to the specific contribution of each mode to the entire far field.

This method uses the relationship in (6.6) in a straight-forward approach by exploiting the orthogonality of the modes. Under the assumption that only a limited number of modes add a significant contribution to the radiation, the computational effort can be reduced. Therefore, the power budget in (4.12) can

6. Source Reconstruction

be used in order to check if all relevant modes are included in the calculation, i.e., the power budget must be reasonably close to unity.

The presented method is simple and leads to a good estimation of the relevant modes, i.e., which eigenvalues are reasonably low. However, the accuracy is limited when the eigenvalue of the observed mode is large. The origin of this inaccuracy is the far field relation in (6.2). As explained earlier, Equation (4.4) is chosen for the normalization to ensure that all modes radiate exactly 1 W power. If the normalization is applied, Equation (6.7) should be exact as well, but is indeed affected by numerical inaccuracies.

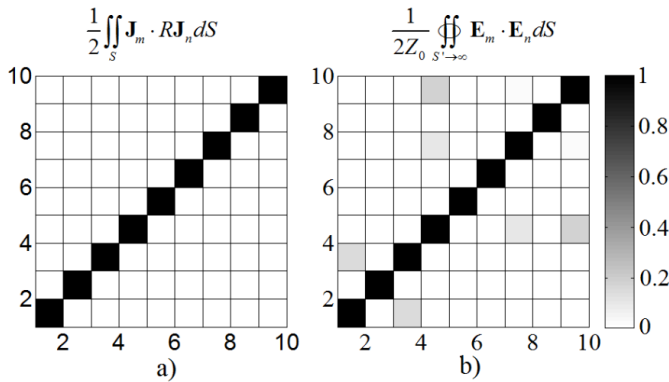


Fig. 6-1 a) Correlation of 10 characteristic modes of the surface current density of a rectangular plate with dimensions $120 \times 60 \text{ mm}^2$ at $f = 1 \text{ GHz}$. B) Correlation of the related far field modes obtained using (6.7). The axes are related to the order numbers of the characteristic modes. © IEEE 2013 [Saf13].

Fig. 6-1 illustrates the inaccuracies by a simple test applied to the characteristic modes of a rectangular plate having the dimensions $120 \times 60 \text{ mm}^2$ at $f = 1 \text{ GHz}$. The actual characteristic modes of the surface current density are orthogonal to each other. Therefore, their auto-correlation must be one, and their cross-correlation must be zero. As can be observed from Fig. 6-1 a) this can be achieved as a result of a numerical calculation with good accuracy.

However, if the far field transformation is applied using (6.2) and the correlation test is performed again, slight inaccuracies for some modes are obtained, as denoted in Fig. 6-1 b). A close look at the eigenvalues of these modes exhibits high eigenvalues of $|\lambda_3| = 3250$ for Mode 3, $|\lambda_7| = 1975$ for Mode 7 and $|\lambda_9| = 166$ for Mode 9. For most of the other modes, the eigenvalues are low, and the error in the correlation is relatively small. Therefore, the contribution of these modes to the entire far field is extremely small, and their accuracy suffers more from numerical inaccuracies of the far field transformation due to the limited dynamic range.

Nevertheless, the ‘‘Scalar-Method’’ is a versatile tool for practical applications, where only the dominant modes with low eigenvalues in the desired frequency range are of interest. However, in order to increase the accuracy for modes with high eigenvalues, the actual method can even be expanded to what is called the ‘‘Matrix-Method’’. The second method takes possible inaccuracies in the modal far field into account in order to improve the calculation of the coefficients.

6.3.2 Matrix Method

As explained in the previous section, the ‘‘Scalar-Method’’ leads to inaccuracies in case of high eigenvalues of certain modes. Therefore, the simplification in (6.6) cannot be applied and the correlation between the total far field \mathbf{E} and the certain mode \mathbf{E}_n results in

$$\begin{aligned} \rho_{\text{total},n} &= \frac{1}{2Z_0} \iint_{S' \rightarrow \infty} \frac{1}{\sqrt{P_{\text{rad}}}} \mathbf{E} \cdot \mathbf{E}_n^* dS = \sum_m \frac{a_m}{\sqrt{P_{\text{rad}}}} \frac{1}{2Z_0} \iint_{S' \rightarrow \infty} \mathbf{E}_m \cdot \mathbf{E}_n^* dS \\ &= \sum_m b_m \frac{1}{2Z_0} \iint_{S' \rightarrow \infty} \mathbf{E}_m \cdot \mathbf{E}_n^* dS . \end{aligned} \quad (6.9)$$

The correlation in (6.9) now contains several unknown normalized coefficients

6. Source Reconstruction

b_n which cannot be solved by a single equation. If the correlation is evaluated for N modes, it results in a linear system, where the coefficients can be determined by a simple matrix inversion. Now, the reconstruction is formulated in terms of a matrix equation:

$$\begin{pmatrix} \rho_{\text{total},1} \\ \vdots \\ \rho_{\text{total},N} \end{pmatrix} = \begin{pmatrix} \{\mathbf{E}_1, \mathbf{E}_1\} & \cdots & \{\mathbf{E}_N, \mathbf{E}_1\} \\ \vdots & \ddots & \vdots \\ \{\mathbf{E}_1, \mathbf{E}_N\} & \cdots & \{\mathbf{E}_N, \mathbf{E}_N\} \end{pmatrix} \cdot \begin{pmatrix} b_1 \\ \vdots \\ b_N \end{pmatrix}. \quad (6.10)$$

where the $\{\cdot\}$ operator is defined by

$$\{\mathbf{E}_m, \mathbf{E}_n\} = \frac{1}{2Z_0} \iint_{S' \rightarrow \infty} \mathbf{E}_m \cdot \mathbf{E}_n^* dS. \quad (6.11)$$

The entities of the matrix in (6.10) contain the correlation of the modes. If the far field modes obtained from the numerical calculation would be perfectly decorrelated, the matrix would result in the identity matrix, and the solution of the unknown normalized coefficients b_n would be obvious.

In order to evaluate the matrix in (6.10), N modes are required where at least some of them have to add a significant contribution. The eigenvalue λ_n is used here to detect the relevant modes. If the eigenvalue is within the range $-100 < \lambda_n [1] < 100$, the mode is taken into account.

6.4 Examples

For the numerical validation, two examples with increasing complexity are discussed. In the first example, a simple plate excited by an incident plane wave \mathbf{E}_{inc} is investigated (see Fig. 6-2 a)). This example is somehow generic, as the incident plane wave just excites the main modes along the major axis in accordance with the boundary conditions of the plate. This example, first of all, acts as a validation of the proposed methods.

In the second example, an iPhone 4, shown in Fig. 6-2 b), is modeled in Empire XPU [EMP] with a reasonable amount of geometrical complexity. It contains the main metal parts including the two parts of the metal frame, which are used as coupling (antenna) elements as well as some plastic and glass of the casing. Assuming that the entire chassis determined by the overall dimensions of the phone represents the radiation mechanism sufficiently, a plate of the same outer dimensions as the iPhone 4 is modeled in the in-house software (please see Fig. 6-2 c)) in order to calculate its characteristic modes. The far field of the complex structure for these modes is traced with the reconstruction methods.

The reconstruction for the two examples is realized with six modes, which are shown in Fig. 6-3.

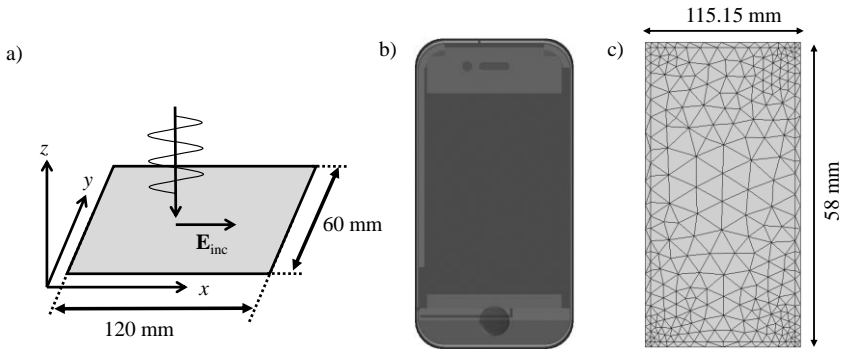


Fig. 6-2 Rectangular plate excited by a plane wave \mathbf{E}_{inc} polarized parallel to the major axis a). The Empire model of the iPhone 4 b) and the simplified structure c). © IEEE 2013 [Saf13].

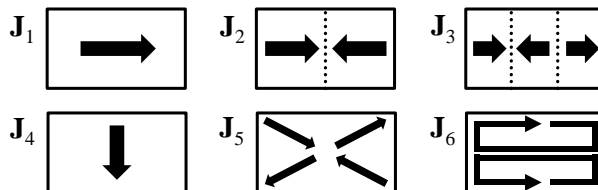


Fig. 6-3 Six characteristic modes of the plate shown in Fig. 6-2 a). © IEEE 2013 [Saf13].

6. Source Reconstruction

6.4.1 Plane Wave

The results of the reconstructions with the two methods are shown in Fig. 6-4. The “Scalar-Method” in Fig. 6-4 a) shows good agreement for the dominant mode \mathbf{J}_1 over the simulated frequency range. This mode carries nearly all the power up to $f \leq 3$ GHz. Other modes add only significant contribution above $f > 3$ GHz. The reconstruction of mode \mathbf{J}_3 , shows relatively large errors below $f < 2$ GHz, where their contribution to the total radiated far field is low. Other modes (\mathbf{J}_2 , \mathbf{J}_4 , \mathbf{J}_5 and \mathbf{J}_6) have a negligible contribution to the entire far field in the observed frequency range. It can be observed in Fig. 6-4 b) that the “Matrix-Method” gives better results even in the case of high eigenvalues. The remaining error for high eigenvalues is negligible for practical applications as a coefficient $|b_n| < -40$ dB means that the mode contributes less than 1 % of the total radiated power.

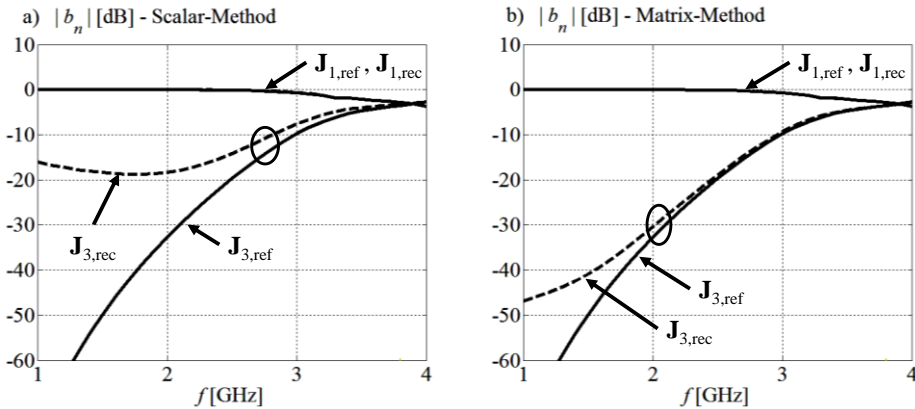


Fig. 6-4 Result of the reconstruction for the first example shown in Fig. 6-2 a). a) Reconstruction using the “Scalar-Method” and b) using the “Matrix-Method” for 2 relevant modes shown in Fig. 6-3. The subscript “ref” denotes a reference value and ‘rec’ denotes the result of the reconstruction. © IEEE 2013 [Saf13].

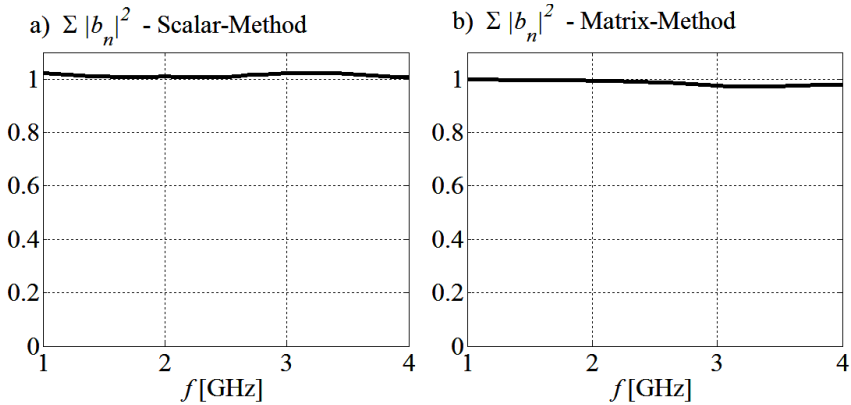


Fig. 6-5 Power budget of the first example calculated with the “Scalar-Method”, shown in a), and “Matrix-Method,” shown in b). For the power budget, $N = 10$ modes are taken into account. © IEEE 2013 [Saf13].

In order to check whether the reconstruction gives meaningful results at all, the power budget in (4.12) is used (please see Fig. 6-5). The summation of all normalized coefficients b_n should be close to one, if all significant modes are involved. The small offset (Fig. 6-5) is the effect of the error in the far field transformation. The consequence of the error is the limited accuracy in the reconstruction of the coefficients b_n . If a number of distorted coefficients $|b_n|^2$ is summed up with the accurate coefficients $|b_n|^2$ of dominant modes, a value larger than one can occur. This is an indication that only a small number of modes (one or two modes) has a significant contribution to the total far field. As can be observed in Fig. 6-5 b), the “Matrix-Method” compensates the error and the power budget is close to one.

6.4.2 iPhone 4

In the second example, an iPhone 4 is investigated. The Empire XPU [EMP] model includes quite an amount of geometrical details as well as the antenna structure for the GSM and UMTS bands. Assuming again that the main radiation mechanism is carried by the chassis itself and the antenna elements just

6. Source Reconstruction

act as coupling elements for the chassis modes, a simple rectangular plate, having the same outer dimensions as the iPhone 4, is modeled in the in-house.

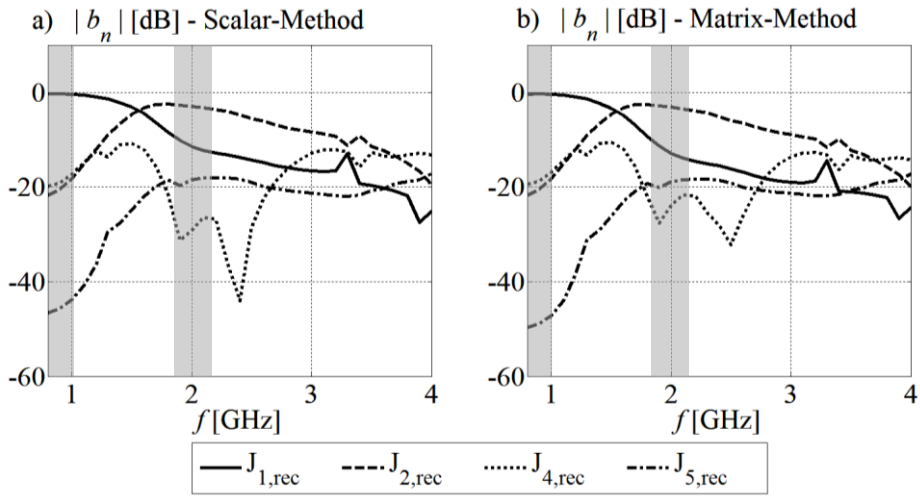


Fig. 6-6 Result of the reconstruction for the iPhone 4 shown in Fig. 6-2 a). a) Reconstruction using the “Scalar-Method” and b) using the “Matrix-Method” for four relevant modes shown in Fig. 6-3. The subscript “rec” denotes the result of the reconstruction. © *IEEE* 2013 [Saf13].

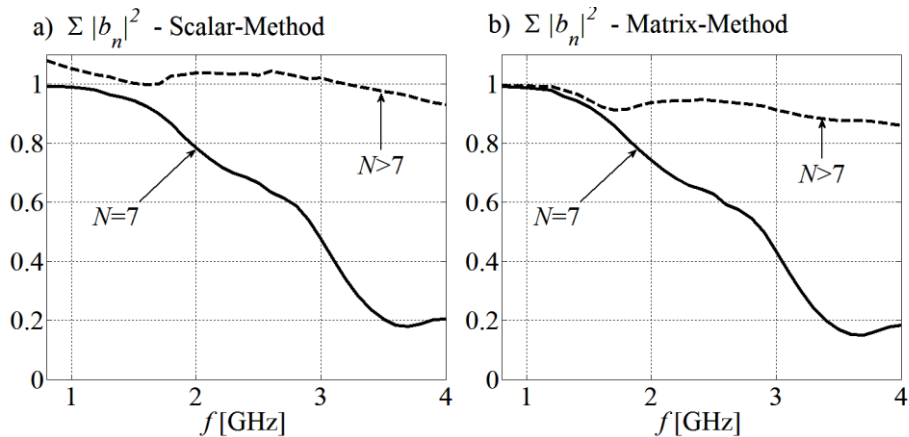


Fig. 6-7 Power budget for the third example (iPhone 4) calculated with the “Scalar-Method”, shown in a), and “Matrix-Method,” shown in b). For the power budget, $N = 7$ and $N > 7$ modes are taken into account. © *IEEE* 2013 [Saf13].

The results of the reconstruction with the two methods are shown in Fig. 6-6. Because the two models are not identical, a reference value is not available in this case. However, the results demonstrate that the iPhone 4 excites different modes, depending on the actual frequency band. At $f = 900$ MHz, mode \mathbf{J}_1 is excited strongly and carries almost 93% of the entire power. With increasing frequency, the significance of mode \mathbf{J}_1 decreases, and mode \mathbf{J}_2 becomes dominant instead. Mode \mathbf{J}_2 carries more than 50% of the entire power at $f = 2$ GHz. Above $f > 2$ GHz, no clear dominance can be determined, since a number of modes is excited with similar significance for the entire radiation.

The two methods result in almost the same coefficients b_n , as can be observed in Fig. 6-6. The power budget is shown in Fig. 6-7, and it can be observed that it gives reasonable results for both methods, if a sufficient number of characteristic modes is taken into account ($N > 7$).

Chapter 7

Characteristic Admittance and Impedance

The characteristic modes offer the possibility to understand the physical mechanism essential for the radiation. Modal parameters can be derived to give hints on how to optimize the radiating structure and to enhance the impedance behavior and, hence, the bandwidth potential. For that, an additional modal parameter — the modal admittance and impedance of the feeding port — can be used for the optimization. These parameters can be used to derive equivalent circuits and to find the optimal impedance matching network. In [Yee73], the modal admittance has been introduced first. The author has evaluated the modal admittance on a two-port wired antenna system. He decomposed the input admittance and the mutual admittance into the modal admittances, which provide information about the modes that contribute strongly. Furthermore, the author reports about a slow convergence of the series expansion with the TCM for the input admittance. In [Cab07], the convergence problem is investigated in more detail.

The development of equivalent circuit models for the feeding port is an interesting problem that has been studied for many years. The decomposition of the

7. Characteristic Admittance and Impedance

input impedance or admittance into a limited set of sub circuits, which represent the natural resonances of the antenna structure, can benefit from the modal decomposition. In [Cab07, Ada13, Kre14], some circuit models have been presented, which have been derived by the TCM. For that, the equivalent circuit has been considered as a series *LC*-circuit, or a high pass filter 2nd order. In addition to the modal decomposition, a shunt capacitor is used in almost all models to complete the series expansion of the input impedance or admittance. This shunt capacitor represents the higher order modes that radiate less power (in typical antenna designs, the power radiated by the higher order modes is close to zero). Since the numerical calculation of such higher order modes is difficult the overall influence is modeled with the shunt capacitor. Such approximation is valid within a limited frequency range and for limited antenna shapes. In the following, chapter a more advanced approximation of the higher order modes is presented to improve the modal admittance decomposition. A definition for the modal impedance is given as an alternative to the modal admittance. Furthermore, the reactive load concept is used to demonstrate how the impedance matching technique affects the modal admittance and impedance decomposition. The convergence of the modal series expansion is the main focus of this chapter.

7.1 Characteristic Admittance

The input admittance can be fully decomposed into modal admittances for an infinite number of modes. Such decomposition has been presented in [Yee73] and is

$$Y_{\text{in}} = \sum_{n=1}^{\infty} Y_n \quad (7.1)$$

for the self- and mutual-admittance.

The modal admittance can be described by the eigenvalue and the modal surface current at the respective feeding position:

$$Y_n = \frac{1}{2} \frac{1}{(1 + j\lambda_n)} [l_m I_m]^2, \quad (7.2)$$

where l_m is the edge length and I_m is the surface current of the mode at the m -th position.

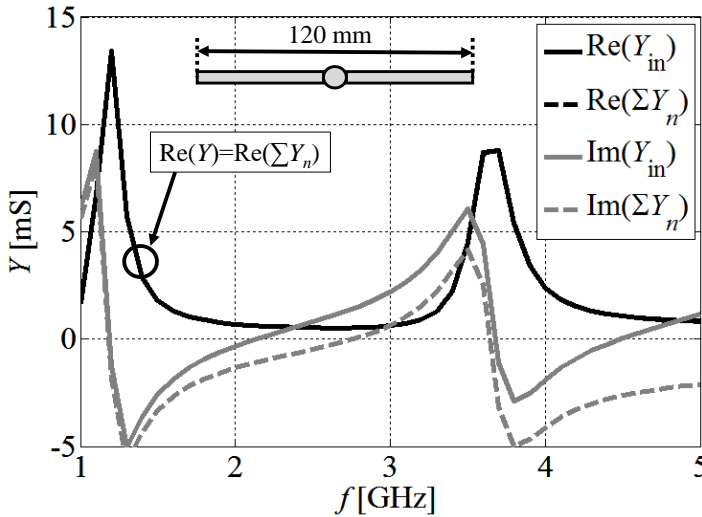


Fig. 7-1 Admittance decomposition with four ($N=4$) dipole modes. The center-fed dipole has the length of $l = 120$ mm.

The modal decomposition (7.1) is not practicable since a limited number of modes is available from the eigenanalysis. Hence, the following question arises: How accurate is the decomposition (7.1) with a limited number of modes? The answer was given by the author in [Yee73] who introduced the admittance decomposition. A finite summation of the modal admittances is complete only for the real part of the admittance. The imaginary part of the admittance requires higher order modes which do not radiate power. Such modes have a high Q-factor and they have a high magnitude eigenvalue

7. Characteristic Admittance and Impedance

($|\lambda_n| \rightarrow \infty$). In Fig. 7-1, the admittance decomposition (7.1) with (7.2) and $N = 4$ modes is shown for a center-fed dipole having the length $l = 120$ mm. It can be observed that the real part of the admittance equals the summation of the real part of the modal admittances. The imaginary part shows a deviation in the entire frequency range.

From that point of view the admittance is decomposed into a limited number of N modes and the remaining admittance Y_{Rest} :

$$Y_{\text{in}} = \sum_{n=1}^N Y_n + Y_{\text{Rest}}. \quad (7.3)$$

The remaining admittance Y_{Rest} can be described further with the higher order modes with:

$$\begin{aligned} Y_{\text{Rest}} &= \sum_{n=(N+1)}^{\infty} \frac{1}{2} \frac{1}{(1 + j\lambda_n)} [I_m I_m]^2 \approx \sum_{n=(N+1)}^{\infty} \frac{1}{2} \frac{1}{j\lambda_n} [I_m I_m]^2 \\ &= \sum_{n=(N+1)}^{\infty} (-j) \frac{1}{2} \frac{[I_m I_m]^2}{\lambda_n}. \end{aligned} \quad (7.4)$$

From (7.4), it is clear that the remaining admittance is purely imaginary, and affects only the imaginary part of the admittance. Although the eigenvalue λ_n tends to infinity, the surface current I_m at the m -th position can tend to infinity for certain higher order modes. From the numerical point of view, the calculation of these higher order modes is difficult, and the approximation of the remaining part Y_{Rest} is required.

The approximation of the remaining part Y_{Rest} with a single shunt capacitor ($Y_{\text{Rest}} = j\omega C$) is the most favorite method used in literature. Indeed, such approximation can give reasonable results for some antenna geometries in a limited frequency range. For more complex antenna shapes, a more advanced approx-

imation is required to be able to describe the admittance behavior. The convergence series is highly affected by the antenna geometry in a close vicinity of the feeding port. Therefore, the approximation must account for the antenna shape near the feeding port.

In recent years the so-called capacitive and inductive coupling elements have proved for the selective excitation of modes as shown in e.g. [Mar14]. Those coupling elements required a more advanced approximation of the remaining admittance with advanced models. Ideal transmission lines are used to describe the natural admittance behavior of the structure.

7.2 Approximation of the Remaining Admittance with an Ideal Transmission Line

The approximation of the remaining admittance is performed separately for the capacitive and inductive coupling elements, as the geometry is somehow different. The capacitive coupling element (CCE) and the inductive coupling element (ICE) are approximated with an open and short-terminated ideal transmission line, as denoted in Fig. 7-2 a) and Fig. 7-2 b), respectively. The unknown parameters of the ideal transmission lines are the input impedance Z_0 and the length l . In the following section, a method is presented to determine the parameter of those ideal transmission lines. Furthermore, the approximation of the given models is investigated, and the limitations are discussed.

In both cases (CCE and ICE), a small ($L = 20$ mm) coupling element and a long ($L = 40$ mm) coupling element are investigated for various positions on the edge of a finite size ground plate.

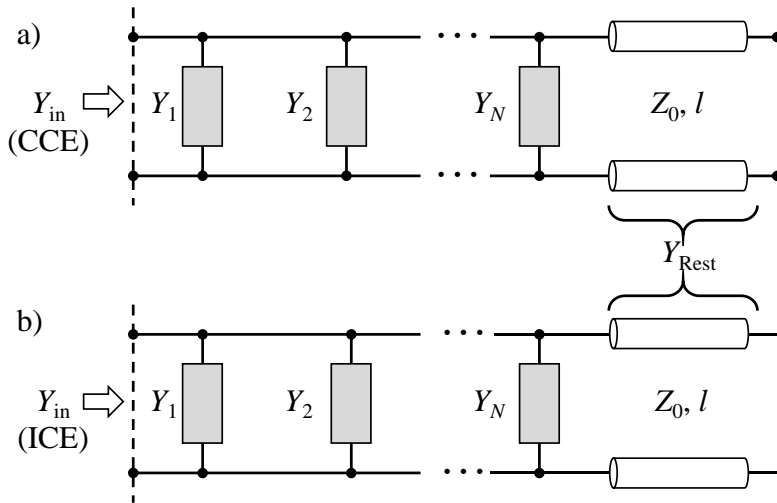


Fig. 7-2 Equivalent circuit model for the modal admittance decomposition. The remaining admittance Y_{Rest} is approximated with an open ideal transmission line a) and a short-terminated ideal transmission line b).

7.2.1 Capacitive Coupling Elements (CCE)

The remaining admittance Y_{Rest} for the CCE is investigated for two lengths of the element ($L = 20$ mm and $L = 40$ mm) and for various positions ($0 \leq d$ [mm] ≤ 60) along the major axis of the finite size ground plate, as denoted in Fig. 7-3.

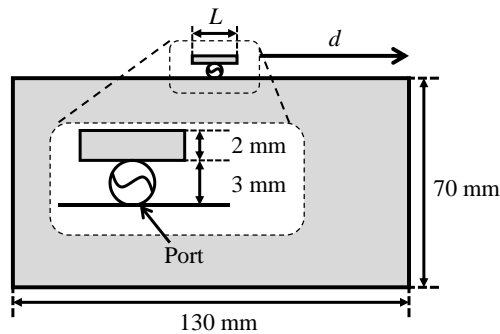


Fig. 7-3 Finite size ground plate with a CCE on the top edge.

7.2 Approximation of the Remaining Admittance with an Ideal Transmission Line

The investigated remaining admittance Y_{Rest} of the input admittance Y_{in} in dependence of the position d of the CCE is shown in Fig. 7-4 and Fig. 7-5, respectively for the small CCE and long CCE. It can be observed that at certain frequencies, if more modes are included in the decomposition, the remaining admittance $Y_{\text{Rest}}(d)$ decreases with a high gradient. The characteristic modes can be calculated accurately up to a specific frequency, where the eigenvalue is less than e.g. $|\lambda_n| < 1000$. Since the eigenvalue of the modes tends to zero and more eigenvalues falls within the eigenvalue range with higher frequency, the modes are used in an incremental manner in the summation in (7.3).

Furthermore, it can be observed that the remaining part $Y_{\text{Rest}}(d)$ is mostly independent of the position d . The imaginary part of the surface current at the feed position is mostly influenced by the geometry in the close vicinity of the feeding port. The transmission line reflects the given influence of the feeding structure of the CCE better, rather than a single shunt capacitor. The admittance of an ideal open transmission line is purely imaginary and, therefore, suitable to model the remaining admittance Y_{Rest} . The circuit model of the CCE is shown in Fig. 7-2 a).

The transmission line parameters (Z_0 and l) can be estimated by the geometry of the CCE and the number N of the characteristic modes used. First, the wave impedance Z_0 of the transmission line is estimated with the aid of an infinite size ground. The wave impedance Z_0 is nearly identical to the wave impedance of an infinite long CCE placed on an infinite size ground. The numerical estimated value with Empire XPU [EMP] is $Z_0 \approx 130 \Omega$. Next, the length l of the transmission line is determined for different CCE lengths L . If the CCE is small compared to the wavelength ($L \ll \lambda$), the geometrical length of the CCE can be used to determine the parameter l . In the proposed example, the geometrical

7. Characteristic Admittance and Impedance

length of the CCE is $L = 10$ mm, and this leads to a slight longer parameter $l = 10.8$ mm. In the other case, if the length of the CCE is nearly or larger than the wavelength, the modal surface currents can be used to find the parameter l . For that the frequency f_0 is determined where the approximation of the total surface current with a limited set of N modes is reasonable:

$$\left| I_m - \sum_{n=1}^N a_n I_n \right|^2 = 0. \quad (7.5)$$

After the frequency f_0 is determined, the parameter l is calculated by the use of the well-known impedance equation of an open transmission line:

$$Z = -jZ_0 \cot\left(\frac{2\pi}{\lambda} l\right). \quad (7.6)$$

The parameter l is determined by enforcing the phase term of the cotangent in (7.6) to be zero with:

$$l = \frac{c_0}{4f_0}. \quad (7.7)$$

The zero magnitude frequency (7.5) for the long CCE ($L = 40$ mm) is $f_0 = 3.275$ GHz, this leads to the parameter $l = 22.9$ mm. The method presented to determine the open transmission line parameters are valid for the specific geometry of the CCE and with some modifications (instead of (7.6), the impedance equation of an ideal short-terminated transmission line is used) only for the ICE. It has to be clarified that the calculated values are an approximation of the parameters required to model the remaining admittance Y_{Rest} . In some cases, a careful tuning of the length l or the impedance Z_0 might be required.

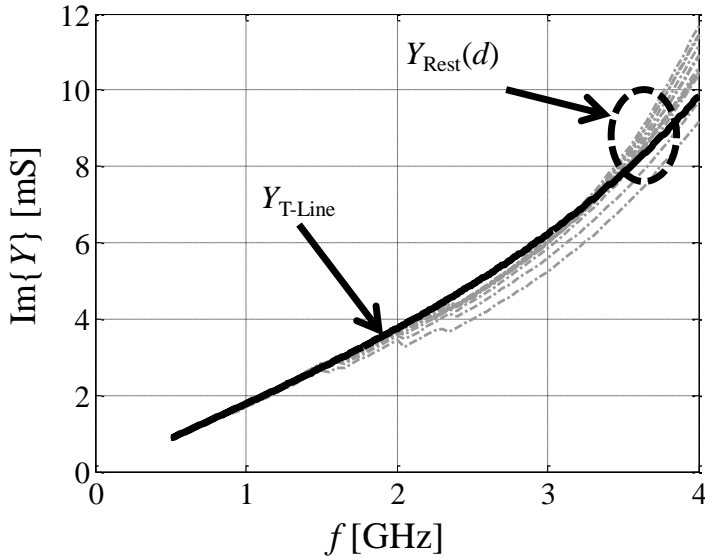


Fig. 7-4 Imaginary part of the admittance $Y_{\text{Rest}}(d)$ of the CCE ($L = 10$ mm). The gray curves denote the remaining part of the decomposition for different positions of the small CCE. The solid black line $Y_{\text{T-Line}}$ denotes the approximation with an ideal open-terminated transmission lines.

The admittance of the approximated open-terminated transmission line is shown in Fig. 7-4 for a small CCE ($L = 10$ mm) and in Fig. 7-5 for a large CCE ($L = 40$ mm). Both models, with the estimated transmission line parameters Z_0 and l , approximate the remaining admittance Y_{Rest} good, except near the zero admittance point $Y_{\text{Rest}}(f = 3.3$ GHz) in Fig. 7-5. However, the remaining admittance Y_{Rest} for $L=40$ mm in Fig. 7-5 shows the behavior of the imaginary part of a lossy open-terminated transmission line or the imaginary part of a lossy high pass 2nd order (such approximation has been used in [Ada13] to derive equivalent circuit models of the characteristic modes).

The approximation of the remaining admittance Y_{Rest} is invalid near the zero admittance frequency ($\text{Im}\{Y_{\text{Rest}}(f)\}=0$), as can be clearly observed in Fig. 7-5.

7. Characteristic Admittance and Impedance

Depending on the number of used modes N the resonance of the input admittance is slightly lower than the zero admittance point (typically $\Delta f \approx 300$ MHz with $N = 4$). Therefore, a reasonable modal decomposition of the admittance Y_{in} at the resonance frequency ($\text{Im}\{Y_{in}\}=0$) can be reached for the proposed examples.

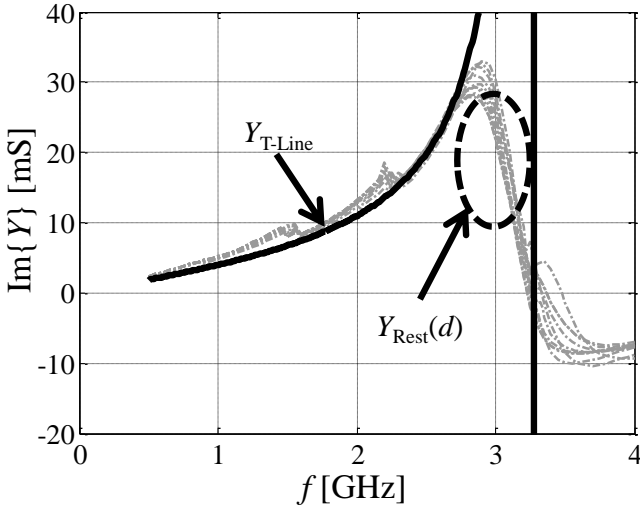


Fig. 7-5 Imaginary part of the admittance $Y_{Rest}(d)$ of the CCE ($L = 40$ mm). The gray curves denote the remaining part of the decomposition for different positions of the small CCE. The solid black line Y_{T-Line} denotes the approximation with an ideal open-terminated transmission lines.

7.2.2 Inductive Coupling Elements (ICE)

The ICE is an interesting alternative to the commonly used CCE to excite the characteristic modes on a small terminal. In [Mar14], several ICEs are used in combination to design a MIMO antenna system. It has been shown that single modes can be excited with a high purity with the ICEs. The example that has been treated now is somehow similar to the previous example. A slit with a variable length L is brought into the finite size ground plate at different positions d , as shown in Fig. 7-6. The ICE is shifted till the corner of the ground

plane with respect to the used length L .

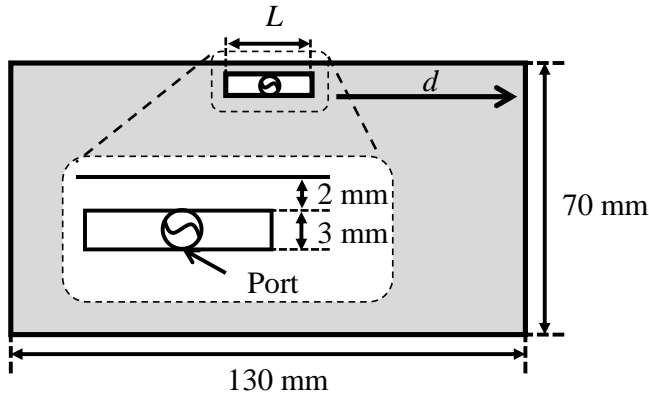


Fig. 7-6 Finite size ground plate with an ICE on the top edge.

The approximation of the remaining admittance Y_{Rest} with a short-terminated transmission line is denoted in Fig. 7-2 b). The transmission line parameters (Z_0 and l) are determined with a method similar to the one presented for the CCE. The wave impedance of the short-terminated transmission line is found to be equal to the wave impedance of the CCE ($Z_0 = 130 \Omega$), since the gap of both coupling elements are the same (3 mm). The parameter l of the short-terminated transmission line — in the case of the small ICE ($L = 10$ mm) — is found to be slightly shorter than the geometrical length ($l = 9.2$ mm). In the case of the long ICE ($L = 40$ mm), the same principle — as presented for the long CCE — can be used. The zero magnitude frequency is determined to be $f_0 = 3.22$ GHz and then used to estimate the length $l = 23.3$ mm ($L = 40$ mm).

The approximation of the remaining admittance Y_{Rest} is shown in Fig. 7-7 for $L = 10$ mm and for $L = 40$ mm. It can be observed that the remaining admittance Y_{Rest} is again independent of the position d of the ICE for both lengths. The assumed approximation of a short-terminated ideal transmission line is

valid in the entire frequency range.

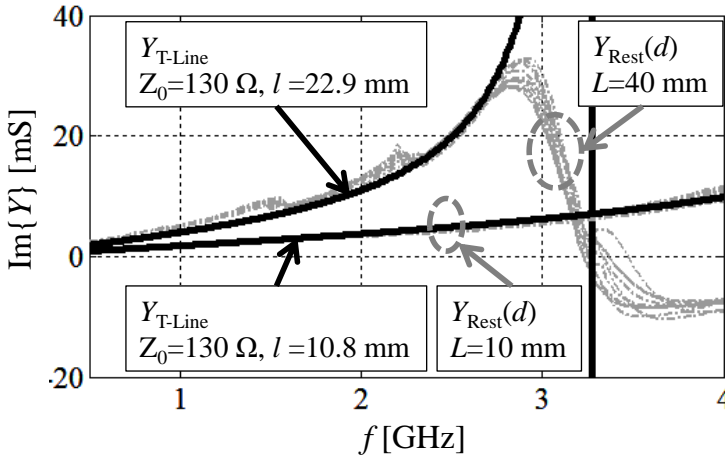


Fig. 7-7 Imaginary part of the admittance $Y_{\text{Rest}}(d)$ of the ICE ($L = 10$ mm and $L = 40$ mm). The gray curves are the remaining admittance $Y_{\text{Rest}}(d)$ of the decomposition for different positions d of the small ICE. The solid black lines $Y_{\text{T-Line}}$ denote the approximation, with ideal short-terminated transmission lines.

7.3 Approximation of the Loaded Remaining Admittance

In the previous chapter, it was shown that the remaining admittance Y_{Rest} can be approximated by an ideal open-terminated or short-terminated transmission line for the CCE and ICE, respectively. Now the investigation is extended toward the reactive loading of the feeding port with a single reactive component. This fundamental impedance matching technique is used to influence the eigenvalue behavior of characteristic mode [Saf15]. The resonance frequency of the modes ($\lambda_n = 0$), which are excited by the coupling element, are shifted to the desired operational frequency in order to achieve good impedance matching. In the following section, the same examples (CCE and ICE) are used with an additional lumped inductance placed at the feeding port to demonstrate the approximation of the remaining admittance Y_{Rest} .

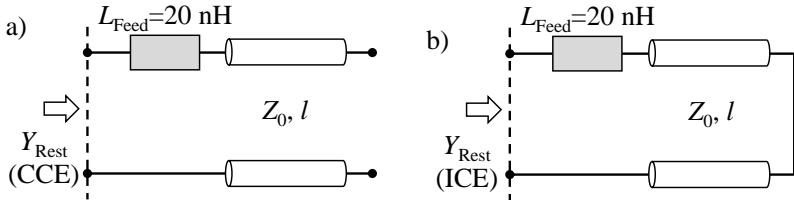


Fig. 7-8 Remaining admittance Y_{Rest} for a loaded CCE a) and ICE b) with inductance $L_{\text{Feed}} = 20$ nH.

7.3.1 Loaded Capacitive Coupling Element

The CCE is now loaded with an inductance $L_{\text{Feed}} = 20$ nH. In order to approximate the new remaining admittance Y_{Rest} , an inductor is inserted in the series with the ideal open-terminated transmission line, as denoted in Fig. 7-8 a). The remaining admittance $Y_{\text{Rest}}(d)$ and the new approximation are shown in Fig. 7-9. The resulting approximation for both lengths is good in the entire frequency range. The length of the transmission line for the long CCE ($L = 40$ mm) is adjusted ($l = 26.7$ mm) with the method explained earlier.

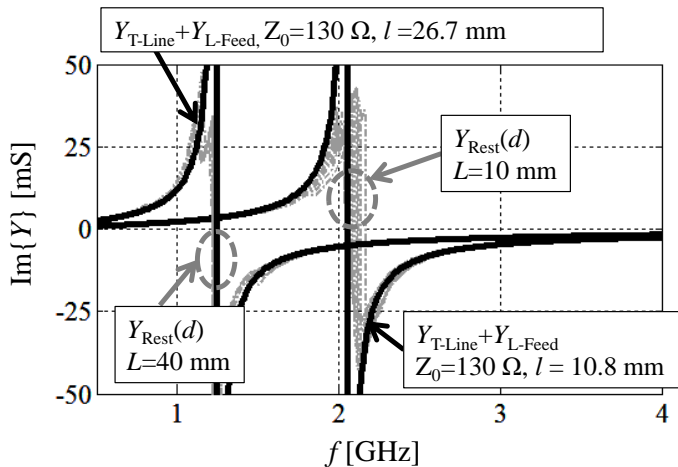


Fig. 7-9 Imaginary part of the admittance $Y_{\text{Rest}}(d)$ of the CCE ($L = 10$ mm and $L = 40$ mm). The gray curves denote the remaining admittance $Y_{\text{Rest}}(d)$ of the decomposition for different positions d of the CCE. The solid black line $Y_{\text{T-Line}} + Y_{\text{L-Feed}}$ denotes the approximation with an ideal open-terminated transmission line in series with the inductance $L_{\text{Feed}} = 20$ nH.

7. Characteristic Admittance and Impedance

7.3.2 Loaded Inductive Coupling Element

The remaining loaded admittance Y_{Rest} of the ICE can be approximated in the same way as presented earlier. The ideal short-terminated transmission line, already introduced, which have the same parameters, is used in combination with the inductance as illustrated in Fig. 7-8 b). The approximated admittance and the remaining admittance $Y_{\text{Rest}}(d)$ are shown in Fig. 7-10. The approximations with the inductance are reasonable except near the zero admittance point $Y_{\text{Rest}}(f = 3.76 \text{ GHz})$ for the long ICE ($L = 40 \text{ mm}$).

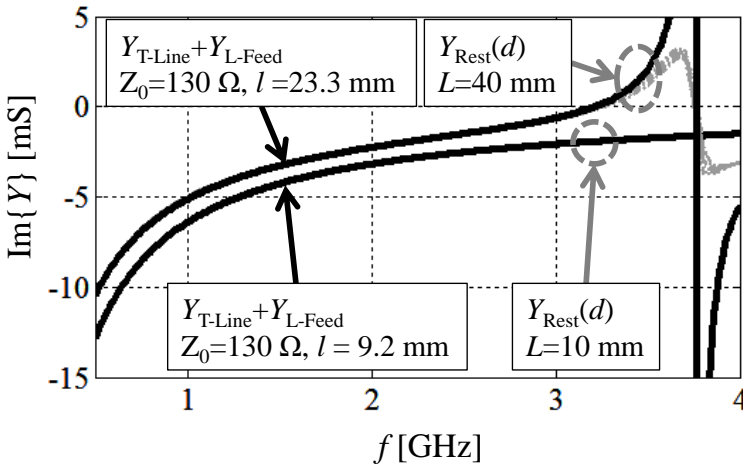


Fig. 7-10 Imaginary part of the admittance $Y_{\text{Rest}}(d)$ of the ICE ($L = 10 \text{ mm}$ and $L = 40 \text{ mm}$). The gray curves denote the remaining admittance $Y_{\text{Rest}}(d)$ of the decomposition for different positions d of the ICE. The solid black line $Y_{\text{T-Line}} + Y_{\text{L-Feed}}$ denotes the approximation with an ideal short-terminated transmission line in the series with the inductance $L_{\text{Feed}} = 20 \text{ nH}$.

From the examples of the CCE and ICE investigated, it can be concluded that an equivalent circuit model can be found to approximate the remaining admittance with and without reactive loading, at the feeding port. In the next section, the characteristic impedances are investigated, which allow a more intuitive interpretation of the input impedance from the modal point of view.

7.4 Characteristic Impedance

The decomposition of the input admittance into a set of characteristic admittances as described earlier, can be modified for an alternative decomposition into characteristic impedances. Owing to the orthogonality of the modes the power budget is a summation of the power each mode contributes [Saf13]. Therefore, a modal impedance Z_n can be found to represent the modal power relation with:

$$Z_n = \frac{2|a_n|^2}{|l_m I_m|^2} (1 + j\lambda_n), \quad (7.8)$$

This equation can be rewritten further into:

$$Z_n = \frac{1}{2} \frac{[l_m I_m]^2}{1 - j\lambda_n} \left| \sum_{n=1}^{\infty} \frac{1}{2} \frac{[l_m I_m]^2}{1 + j\lambda_n} \right|^{-2} = \frac{(Y_n)^*}{\left| \sum_{n=1}^{\infty} Y_n \right|^2}. \quad (7.9)$$

The poor convergence of the series expansion in (7.1) requires a modification of (7.9). The infinite summation of the modal admittances is replaced by the input impedance Z_{in}

$$Z_n = |Z_{in}|^2 (Y_n)^*. \quad (7.10)$$

This formula is a simple transformation from a shunt circuit into a series circuit. In a similar manner, as denoted in (7.3), the input impedance can be approximated by N modes:

$$Z_{in} = \sum_{n=1}^N Z_n + Z_{Rest}. \quad (7.11)$$

The remaining impedance Z_{Rest} can be approximated with the same components (open- and short-terminated ideal transmission lines) having the same

7. Characteristic Admittance and Impedance

parameters (Z_0 and l) as presented in the previous sections.

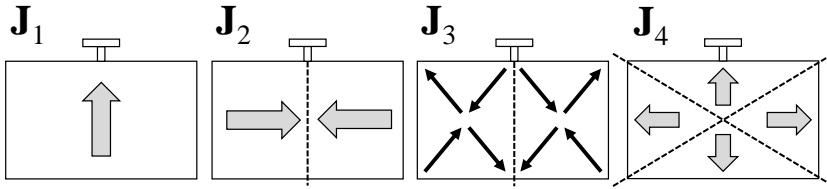


Fig. 7-11 Four significant modes for the impedance decomposition of the rectangular plate ($130 \times 70 \text{ mm}^2$) with a CCE on top.

The characteristic impedance is evaluated for the example shown in Fig. 7-3. Four characteristic modes (see Fig. 7-11) are significant for the impedance decomposition in (7.11). Mode \mathbf{J}_1 and \mathbf{J}_2 are well-known as they represent the half- and the full-wave dipole mode in vertical and horizontal direction, respectively. The other two modes $\mathbf{J}_{3,4}$ are higher order capacitive modes which become significant above $f > 2 \text{ GHz}$. The surface current of the respective modes \mathbf{J}_{1-4} on the feeding position is high.

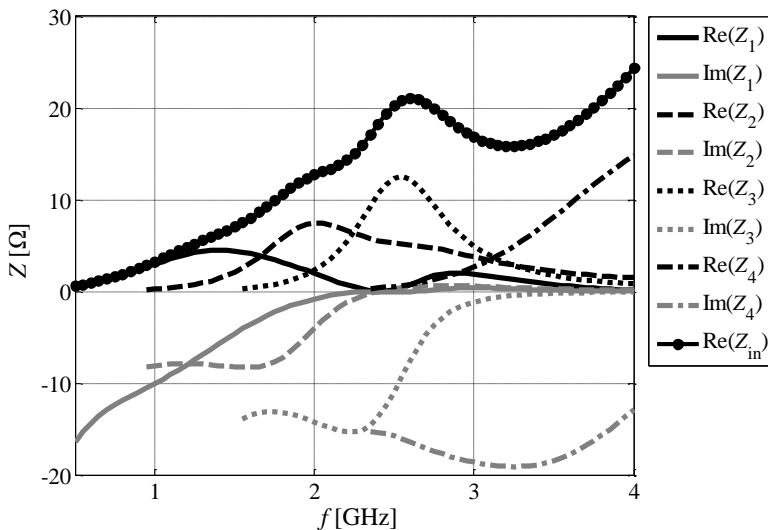


Fig. 7-12 Characteristic impedances of four significant modes and the real part of the input impedance Z_{in} for the example, with the CCE having the length $L = 10 \text{ mm}$ and the

7.5 Manipulation of the Characteristic Impedance with Reactive Elements

position $d = 0$ mm.

The characteristic impedances Z_{1-4} are shown in Fig. 7-12. It can be observed that the real parts of the characteristic impedances Z_{1-4} show an alternating dominance for the real part of the input impedance Z_{in} . Furthermore, the imaginary part of the characteristic impedances is zero ($\text{Im}\{Z_n\} = 0$), if the respective mode is in resonance ($\lambda_n = 0$), as expected. The approximation of the input impedance Z_{in} with the $N = 4$ modes and the remaining impedance Z_{Rest} is shown in Fig. 7-13. These four modes \mathbf{J}_{1-4} are required to decompose the real part of the input impedance Z_{in} . The imaginary part shows good agreement with the equivalent transmission line model.

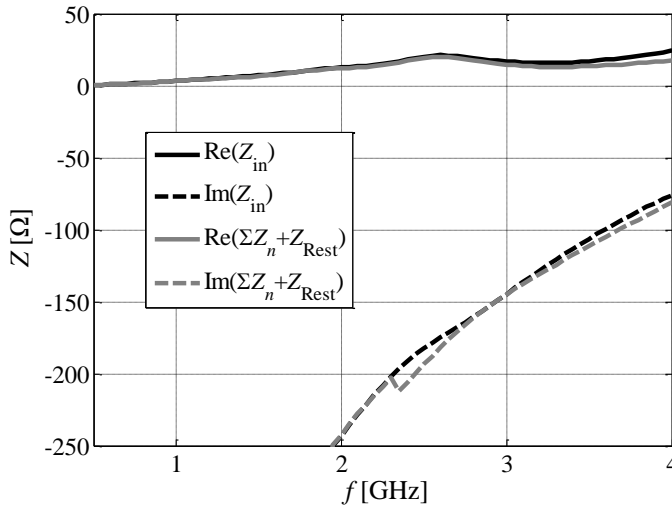


Fig. 7-13 Input impedance of the CCE ($L = 10$ mm and $d = 0$ mm) and the approximated impedance with $N = 4$ modes.

7.5 Manipulation of the Characteristic Impedance with Reactive Elements

The basic characteristic impedances can be modified with well-placed reactive

7. Characteristic Admittance and Impedance

components on the surface. In [Har72b, Mau73], this concept is used to manipulate the resonance frequency of a single mode. The same principle can be used to manipulate the characteristic impedances Z_n and the remaining part Z_{Rest} in order to impedance-match the feeding port.

In the following example, $N = 4$ modes are investigated, which are loaded with a single inductance $L_{\text{Feed}} = 10$ nH. The influence of the inductance is included in the characteristic mode computation, as explained in [Har72b] and in the approximation of the remaining impedance Z_{Rest} , as denoted in Fig. 7-14. The real and imaginary part of the modal impedances for the first four modes \mathbf{J}_{1-4} are shown in Fig. 7-15 and Fig. 7-16, respectively. It can be observed that the real and imaginary part of the modal impedance Z_1 is changed drastically. This mode is now more dominant, up to $f = 2.6$ GHz. The modal impedance Z_2 is mostly unchanged within the observed frequency range, although the surface current is high at the feeding position. The other two modes $\mathbf{J}_{3,4}$ are insignificant above $f \geq 2$ GHz. The surface current of these modes has been lowered in the close vicinity of the feeding port. It is obvious that above $f \geq 2.65$ GHz other modes are excited. A reasonable decomposition of the real part of the input impedance is not possible with these four modes. Nevertheless, the decomposition is acceptable up to $f \leq 2.65$ GHz, where the CCE is matched ($|\mathcal{S}_{11}| \leq -6$ dB), as can be observed in Fig. 7-17.

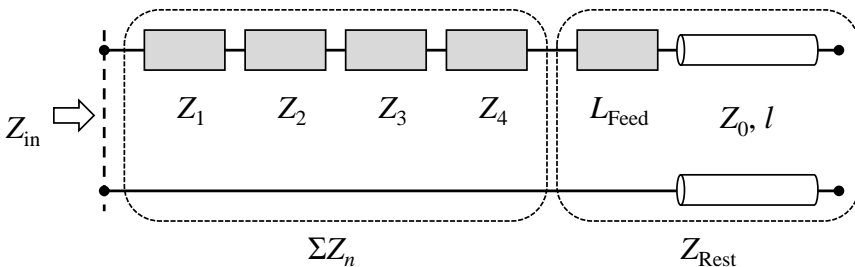


Fig. 7-14 Circuit model of the small CCE ($L = 10$ mm and $d = 0$ mm) with four characteristic impedances Z_{1-4} . The feeding port is loaded with $L_{\text{Feed}} = 10$ nH.

7.5 Manipulation of the Characteristic Impedance with Reactive Elements

The impedance matching with the inductance L_{Feed} can be summarized as follows. The reactive element changes the first significant mode with the lowest resonance frequency while other modes are either unchanged or become less significant.

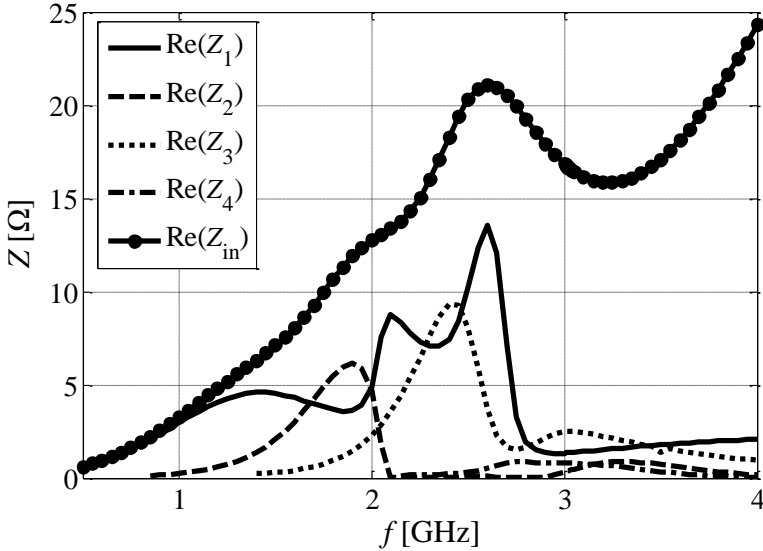


Fig. 7-15 Real part of the characteristic impedances of the mode J_{1-4} and the real part of the input impedance Z_{in} of the CCE ($L = 10$ mm and $d = 0$ mm).

The imaginary part of the characteristic impedances Z_{1-4} is less significant for the overall impedance Z_{in} . On the other hand, the approximated remaining impedance Z_{Rest} is pure imaginary. Only this term is needed to describe the imaginary part of Z_{in} . The inductance L_{Feed} is added to the ideal open-terminated transmission line (see Fig. 7-14). Therefore, it can be concluded that the characteristic impedances are needed to decompose the real part of the impedance, while the remaining part Z_{Rest} , which is needed to compensate the effect of the higher order modes, exerts a high influence on the imaginary part of the input impedance. The same principle holds for the long CCE ($L = 40$ mm, loaded with a capacitor) and for various lengths of the ICE.

7. Characteristic Admittance and Impedance

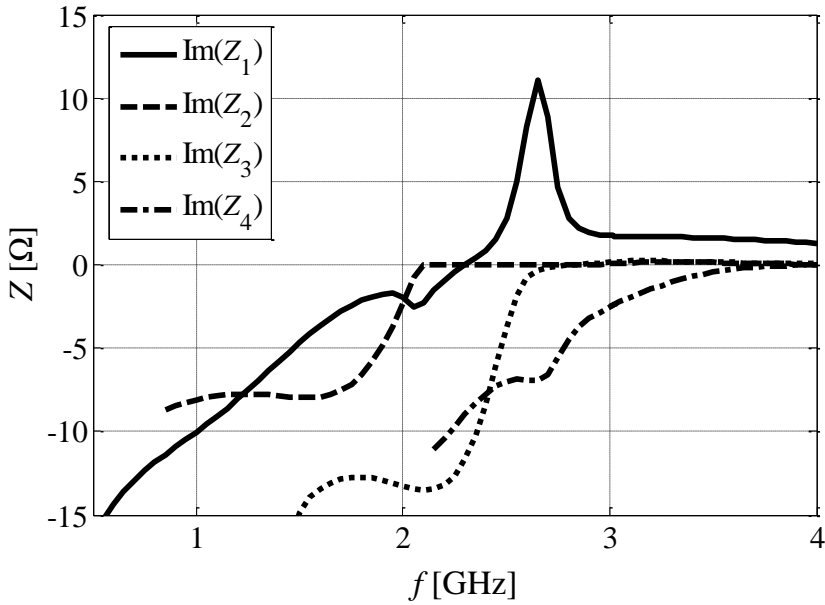


Fig. 7-16 Imaginary part of the characteristic impedances of the mode J_{1-4} of the CCE ($L = 10$ mm and $d = 0$ mm).

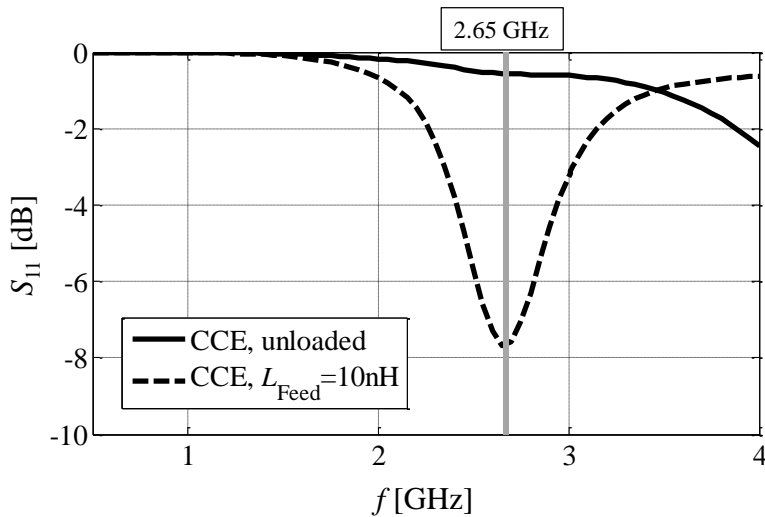


Fig. 7-17 Scattering parameter S_{11} of the CCE with and without the inductance $L = 10$ nH.

Chapter 8

Reactive Loading in the TCM

³Reactive loading of certain parts of an antenna is a powerful instrument to tailor the impedance behavior of the antenna with respect to the desired frequency bands of operation. Different methods are already described widely in basic microwave literature [Jam89, Bal89, Bal05]. The most basic methods simply refer to the entire current distribution on the antenna in order to find out where to place inductors or capacitors that affect this current distribution. More advanced methods — referring to a modal decomposition of the electromagnetic field of the antenna — have been studied intensively for microstrip antennas [Jam89] and dielectric resonator antennas [Bal89, Mon94]. Such modal decompositions facilitate some insight into how a specific loading affects the different wave modes excited on the antenna.

Apart from the conventional use of the TCM, the network ports of a multi-antenna system can be analyzed with the network modes [Vol08]. From such a perspective, a simple model of a much more complex antenna system can be derived and used to design an efficient decoupling network. This could further

³ The following chapter uses textual materials and figures from [Saf15] © *IEEE* 2015.

help optimize the antenna shape and location. The combination of both mode types — the wave modes and the network modes — can help scientist to gain a deeper insight into the internal mechanism responsible for the efficient radiation, mutual coupling and feeding of a multi-antenna system.

8.1 Resonance Manipulation due to Reactance Distribution

In common applications the resonance of the antenna is an important parameter, which is used to impedance match the feeding port towards the load. Therefore, the resonance should be known, as also the method to shift into the desire frequency band. In [Har72b, Mau73], a methodology is presented to find a continuous reactive load distribution on the surface of a PEC antenna structure in order to change the resonance frequencies of the characteristic modes. For that, the weighted eigenvalue equation (2) is extended with a diagonal matrix \mathbf{X}_L such that

$$[\mathbf{X} + \mathbf{X}_L] \mathbf{J}_{L,n} = \lambda_{L,n} \mathbf{R} \mathbf{J}_{L,n} . \quad (8.1)$$

where $\mathbf{J}_{L,n}$ is n -th characteristic mode and $\lambda_{L,n}$ is the n -th eigenvalue of the loaded system.

The matrix \mathbf{X}_L represents the reactive loads on each basis function (in our case the RWG basis function). The diagonal entries $X_{L,i}$ of the matrix \mathbf{X}_L are given by

$$X_{L,i} = \begin{cases} \omega L_i l_i^2 & X_{L,i} > 0 \\ -\frac{1}{\omega C_i} l_i^2 & X_{L,i} < 0 \end{cases} . \quad (8.2)$$

8.1 Resonance Manipulation due to Reactance Distribution

where L_i is the i -th inductance, C_i is the i -th capacitance, ω is the angular frequency and l_i is the edge length of the i -th edge element as defined in [Saf13].

From the numerical point of view this method suffers from poor convergence if the amplitude of the surface current modes is low in magnitude. The other aspect of this methodology is the complicated practical realization of the reactive element distribution on the entire surface. It is therefore more convenient to place few reactive loads in well-defined positions, in order to modify the eigenvalue in accordance with the needs. Since the additional reactive load impedance matrix is added to the generalized eigenvalue equation, the characteristic modes change their surface current distribution. This fact makes an interpretation of the characteristic modes and their properties (e.g. eigenvalue λ_n) difficult. Therefore, it is more convenient to use the initial characteristic modes \mathbf{J}_m to describe the change of the eigenvalues and the surface current distribution. A similar technique is used to solve large-scale problems with the so-called Characteristic Basis Function (CBF) (please see Chapter 4.5 for a brief summary or [Maa08, Mit08]).

Under the assumption that the surface current distribution, under the influence of an arbitrary reactance distribution, can be decomposed fully into the initial surface current modes \mathbf{J}_n , the loaded characteristic modes $\mathbf{J}_{L,n}$ can be written with:

$$\mathbf{J}_{L,n} = \sum_{m=1}^{\infty} a_m \mathbf{J}_m \quad . \quad (8.3)$$

In (8.3) a_m is a real valued weight coefficient of the m -th characteristic mode \mathbf{J}_m of the initial configuration. Substituting (8.3) into (8.1) results in:

8. Reactive Loading in the TCM

$$\begin{aligned}
 & \begin{bmatrix} \langle \mathbf{J}_1, (\mathbf{X} + \mathbf{X}_L) \mathbf{J}_1 \rangle & \langle \mathbf{J}_1, (\mathbf{X} + \mathbf{X}_L) \mathbf{J}_2 \rangle & \cdots \\ \langle \mathbf{J}_2, (\mathbf{X} + \mathbf{X}_L) \mathbf{J}_1 \rangle & \langle \mathbf{J}_2, (\mathbf{X} + \mathbf{X}_L) \mathbf{J}_2 \rangle & \\ \vdots & & \ddots \end{bmatrix} \begin{pmatrix} a_1 \\ a_2 \\ \vdots \end{pmatrix} \\
 &= \mu_n \begin{bmatrix} \langle \mathbf{J}_1, \mathbf{R} \mathbf{J}_1 \rangle & \langle \mathbf{J}_1, \mathbf{R} \mathbf{J}_2 \rangle & \cdots \\ \langle \mathbf{J}_2, \mathbf{R} \mathbf{J}_1 \rangle & \langle \mathbf{J}_2, \mathbf{R} \mathbf{J}_2 \rangle & \\ \vdots & & \ddots \end{bmatrix} \begin{pmatrix} a_1 \\ a_2 \\ \vdots \end{pmatrix}.
 \end{aligned} \tag{8.4}$$

Owing to the orthogonality of the initial modes \mathbf{J}_m , (8.3) is simplified using the normalization ($\langle \mathbf{J}_l, \mathbf{R} \mathbf{J}_k \rangle = 2\delta_{lk}$):

$$\begin{aligned}
 & \left(\underbrace{\begin{bmatrix} 2\lambda_1 & 0 & \cdots \\ 0 & 2\lambda_2 & \\ \vdots & & \ddots \end{bmatrix}}_{\underline{\lambda}} + \underbrace{\begin{bmatrix} \langle \mathbf{J}_1, \mathbf{X}_L \mathbf{J}_1 \rangle & \langle \mathbf{J}_1, \mathbf{X}_L \mathbf{J}_2 \rangle & \cdots \\ \langle \mathbf{J}_2, \mathbf{X}_L \mathbf{J}_1 \rangle & \langle \mathbf{J}_2, \mathbf{X}_L \mathbf{J}_2 \rangle & \\ \vdots & & \ddots \end{bmatrix}}_{\underline{\mathbf{X}}_L} \right) \begin{pmatrix} a_1 \\ a_2 \\ \vdots \end{pmatrix} = \lambda_{L,n} \begin{pmatrix} a_1 \\ a_2 \\ \vdots \end{pmatrix} \\
 &= \lambda_{L,n} \begin{bmatrix} 2 & 0 & \cdots \\ 0 & 2 & \\ \vdots & & \ddots \end{bmatrix} \begin{pmatrix} a_1 \\ a_2 \\ \vdots \end{pmatrix}.
 \end{aligned} \tag{8.5}$$

Finally, the modified eigenvalue equation yields:

$$\left(\underline{\lambda} + \frac{1}{2} \underline{\mathbf{X}}_L \right) \mathbf{a}_n = \lambda_{L,n} \mathbf{a}_n. \tag{8.6}$$

From (8.6), an alternative description of the eigenvalue $\lambda_{L,n}$ can be derived:

$$\lambda_{L,n} = \sum_{l=1}^{\infty} \lambda_l |a_l|^2 + \frac{1}{2} \sum_{l=1}^{\infty} \sum_{k=1}^{\infty} a_l a_k \langle \mathbf{J}_l, \mathbf{X}_L \mathbf{J}_k \rangle. \tag{8.7}$$

In (8.6), the weighting coefficients a_l and a_k are related to the eigenvector \mathbf{a}_n . The term $\langle \mathbf{J}_l, \mathbf{X}_L \mathbf{J}_k \rangle$ describes the correlation of the surface current modes by the positions and values of the reactances.

8.1 Resonance Manipulation due to Reactance Distribution

The solution of the Modified Eigenvalue Equation (8.6) can be calculated more efficiently, since the size of the used matrix is smaller than the commonly used impedance matrix. From the initial definition of the modified modes the left hand side of (8.6) is real and the loaded modes $\mathbf{J}_{L,n}$ are real. For a clear treatment of the eigenvectors the usual normalization to unity ($\underline{\mathbf{a}}_n^T \underline{\mathbf{a}}_m = \delta_{nm}$) is applied. The new set of modes fulfills the condition of orthogonality, as they are composed of a set of already orthogonal modes (of the initial problem without reactive loading). With (8.6), the active and reactive part of the power budget are diagonalized as before and, hence, the loaded modes $\mathbf{J}_{L,n}$ fulfill the required conditions without restriction.

In order to demonstrate the proposed calculation of the eigenvalues a single reactance in the center of a dipole having the length $l = 120$ mm (see 4.6.1) is placed. Fig. 8-1 shows the eigenvalue behavior of the first mode \mathbf{J}_1 , respectively $\mathbf{J}_{L,1}$. It can be observed that the inductance $L = \{5, 10, 15, 20\}$ nH decreases the resonance of the mode \mathbf{J}_1 , while the capacitance $C = \{0.1, 0.2, 0.5, 1, 5\}$ pF increases the resonance frequency, as expected. For a low inductance — or respectively a high capacitance — the reactance curves converge towards the initial eigenvalue behavior.

The method presented can aid understanding of how the reactance exerts influence on the surface current distribution of the modes and their eigenvalue behavior. As an example, Fig. 8-2 shows the weighting coefficient a_l of the first mode $\mathbf{J}_{L,1}$, which is now composed, in principle, out of the initial modes \mathbf{J}_1 and \mathbf{J}_3 (see Fig. 4-1 b)). Other modes can be neglected, since their contribution to the radiated power is rather insignificant. Below 2 GHz the surface current distribution of mode $\mathbf{J}_{L,1}$ is less influenced by the reactance X_L , although the eigenvalue is increased up to $\lambda_{L,1} = 5$. Above 2 GHz a stronger deformation

8. Reactive Loading in the TCM

of the surface current mode $\mathbf{J}_{L,1}$ can be observed. At 3.5 GHz, the surface current of this mode looks more similar to the initial mode \mathbf{J}_3 , as the coefficient a_3 is increased. At this high frequency, \mathbf{J}_3 shows a higher dominance, while mode \mathbf{J}_1 becomes less dominant.

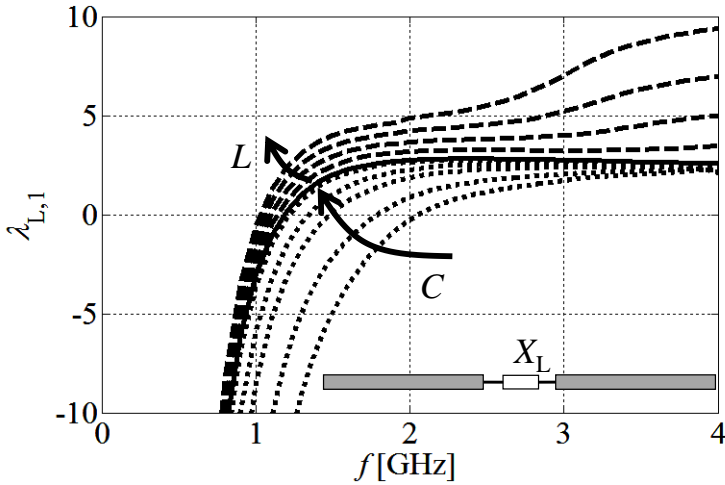


Fig. 8-1 Eigenvalue behavior $\lambda_{L,1}$ of the first mode $\mathbf{J}_{L,1}$ under the influence of a reactance X_L placed in the center of a dipole. The solid black line denotes the initial eigenvalue λ_1 of the first mode \mathbf{J}_1 . © IEEE 2015 [Saf15].

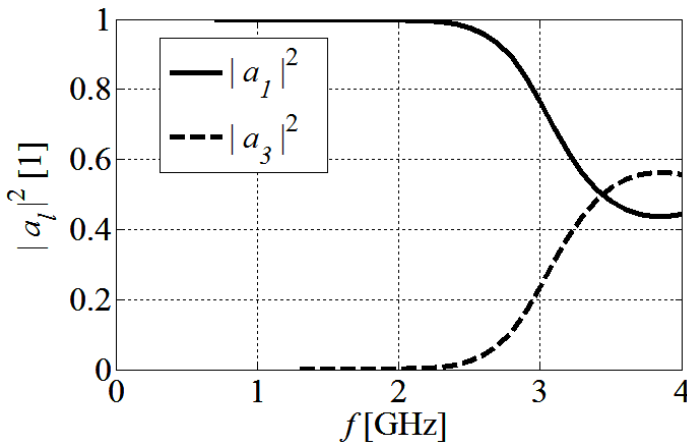


Fig. 8-2 Weighting coefficients of the first and third initial mode (\mathbf{J}_1 and \mathbf{J}_3) for mode $\mathbf{J}_{L,1}$. An inductance $L = 20\text{nH}$ is placed at the center of the dipole. © IEEE 2015 [Saf15].

8.2 Eigenvalue Manipulation by Reactive Loading

The concept of reactive loading, presented in the previous section, allows for the manipulation of the eigenvalue behavior and the resonance frequency of the respective characteristic modes. In this section two different examples — based on the simple dipole previously discussed — will be investigated to show how the basic method (8.6) can be applied quite intuitively e.g. to broadband antennas and multi-antenna systems by adding selective mutual coupling. Both examples are aimed at the selective manipulation of the characteristic modes.

8.2.1 Combined Excitation of Modes to Increase the Impedance Bandwidth of an Antenna

The first example is based on the initial simple dipole (please see Chapter 4.6.1), and emphasis on deriving a modified version with the potential of broader impedance bandwidth. Therefore, it would be desirable to have the resonances of the first two characteristic modes closer to each other. In theory, this can be achieved by shifting the resonance of mode \mathbf{J}_1 up in frequency or shifting mode \mathbf{J}_2 down or a combination of both. Obviously, this is not feasible with the initial dipole structure, but may be achieved with some modification of its shape in combination with reactive loading of specific parts.

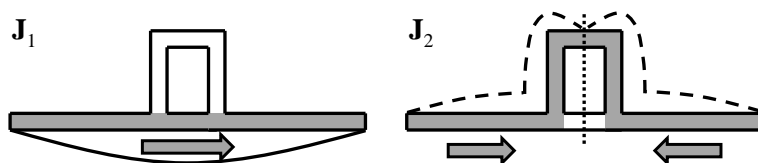


Fig. 8-3 Two surface current modes of a modified dipole. The arrows denote the relative orientation and the curves denote the magnitude of the surface currents. The white branches denote a low magnitude of the modal surface currents. The dashed line in the right figure denotes the symmetry of mode \mathbf{J}_2 . © IEEE 2015 [Saf15].

8. Reactive Loading in the TCM

The simple dipole in Fig. 4-1 a) is reconsidered and its modal eigenvalue behavior is given in Fig. 4-2. Mode \mathbf{J}_1 represents a half wavelength dipole mode with a constant direction of the current along the dipole. Mode \mathbf{J}_2 represents a full wavelength dipole mode, having different directions of the modal current on both arms of the dipole. In order to increase the resonance frequency of mode \mathbf{J}_1 , the dipole is bent, as shown in Fig. 8-3. This modification shortens the surface current distribution of the first mode \mathbf{J}_1 and hence, increases its resonance frequency. Mode \mathbf{J}_2 is not affected by this modification due to the symmetry of the surface currents distribution of this mode.

The modified modal surface current in Fig. 8-3 can be used to identify the positions, where the surface current of one mode exhibits a low magnitude while the other mode is high in magnitude. Such positions are well suited for placing lumped reactive components to manipulate the eigenvalue of the respective modes selectively. Hence, a capacitor of $C = 1\text{pF}$ is placed between the bended branches in order to increase the resonance frequency of mode \mathbf{J}_1 . In addition, two inductors of $L = 20\text{nH}$ are inserted into the left and right branches of the bend in order to decrease the resonance frequency of mode \mathbf{J}_2 . As can be observed from Fig. 8-4 the resonance frequency of mode \mathbf{J}_1 is shifted up in frequency ($f_{j1} = 1.85\text{ GHz}$) compared to the initial dipole while the resonance frequency of mode \mathbf{J}_2 occurs at a lower frequency ($f_{j2} = 2.1\text{ GHz}$).

After the desired modification of the shape and the characteristic modes a location for the feeding port has to be found. The location of the port should facilitate the excitation of the two modes $\mathbf{J}_{1,2}$ as an important criterion. According to the current distribution of the modified modes, such a location is no longer at the center of the dipole but can be found in one of the dipole arms.

Fig. 8-5 shows the final result of the modified dipole with respect to the matching of the antenna. It can be observed that the antenna exhibits a broadband matching ($S_{11} < -6\text{dB}$ for $1.7 < f [\text{GHz}] < 2.25$) due to the excitation of the two modes $J_{1,2}$.

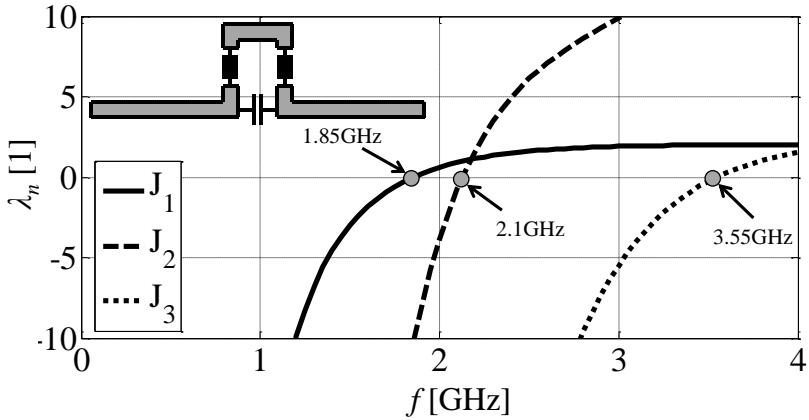


Fig. 8-4 Eigenvalue of three characteristic modes of the loaded modified dipole in Fig. 8-3. © IEEE 2015 [Saf15].

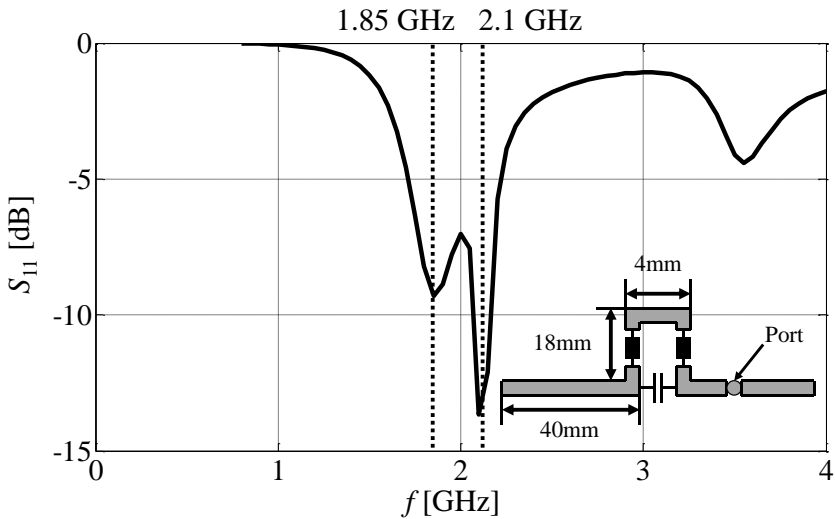


Fig. 8-5 Reflection coefficient of the loaded modified dipole shown in Fig. 8-3 with a feed in the right arm. © IEEE 2015 [Saf15].

8. Reactive Loading in the TCM

The modified dipole modes differs from the initial modes since the structure is changed. However, this approximation does not harm the design methodology in general. Also, the size of the modified dipole needs to be scaled to operate in the desired frequency range. If necessary an adjustment of the location of the elements and their component values can be conducted as an additional optimization process.

8.2.2 Selective Excitation of Modes by Decoupled Antenna Ports

Apart from matching multiple characteristic modes simultaneously for broadband impedance matching some recent applications require multi antenna systems. As the characteristic modes are basically orthogonal to each other in the case of lossless antennas they generally offer the possibility of multi-antenna systems if excited by isolated antenna ports.

In order to derive such a multi-antenna system from the initial dipole, the capability to localize reactive loading needs to be modified, in order to insert selective mutual coupling between different parts of the structure. Therefore, an additional boundary condition is added into the original problem. Two positions v and w are defined, where the selective mutual coupling is added using a lumped component having the impedance Z_L . The voltage on the v -th and w -th positions is now affected not only by the field distribution in free space, but also by the impedance Z_L , as denoted in Fig. 8-6.

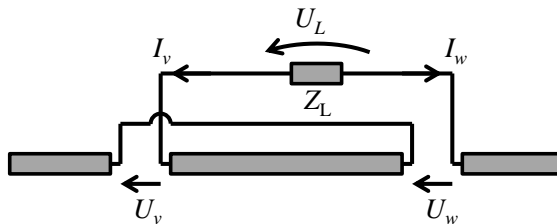


Fig. 8-6 A dipole having the length $l = 120$ mm with an additional mutual coupling Z_L . © IEEE 2015 [Saf15].

The implementation of the additional mutual coupling yields two equations for the voltage

$$U_v - U_w + U_L = 0 . \quad (8.8)$$

and the current

$$I_v + I_w = 0 . \quad (8.9)$$

In (8.8) U_v and U_w are the voltages over the v -th and w -th edge elements, respectively. The new boundary condition is (8.9).

In the next step, the w -th row is subtracted from the v -th row of the original impedance matrix and added on the v -th position of the impedance matrix. The new boundary condition (8.9) is inserted into the w -th row, and the new impedance matrix \mathbf{Z} is obtained:

$$\mathbf{Z} = \begin{pmatrix} \cdots & Z_{v,v} - Z_{w,v} + Z_L l_v^2 & \cdots & Z_{v,w} - Z_{w,w} & \cdots \\ \cdots & & l_v & & \\ \cdots & & & l_w & \cdots \end{pmatrix}, \quad (8.10)$$

where l_v and l_w are the edge length of the respective RWG basis functions.

As can be observed from (8.10), the new impedance matrix \mathbf{Z} is not symmetrical anymore. However, the weighted eigenvalue equation (4.1) can still be used, since the active and reactive power can be determined in the usual way. The eigenvalues and eigenvectors of this system are still real and orthogonal with respect to the radiated far field, if purely reactive loads are used.

In order to demonstrate the influence of the selective mutual coupling an inductor — having the value of $L = 5$ nH — is placed, and the eigenvalue analysis applied as before. The eigenvalues of this configuration are shown in Fig.

8-7.

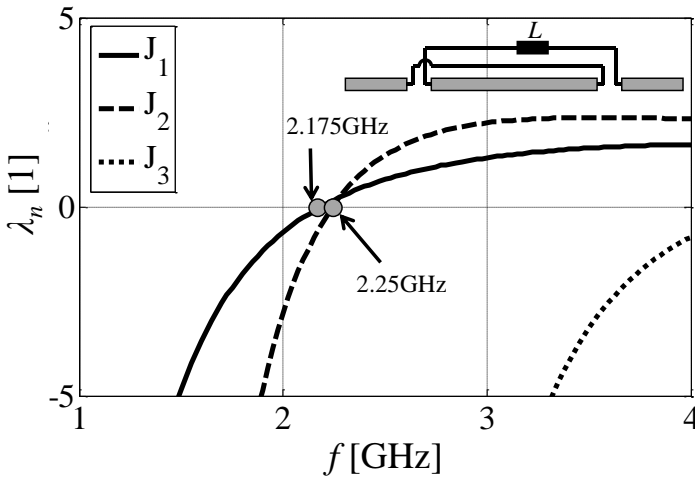


Fig. 8-7 Eigenvalue of three dipole modes with a selective mutual coupling ($Z_L = j\omega L$). © IEEE 2015 [Saf15].

The additional boundary condition, applied on the dipole configuration enforces all surface currents to flow in the opposite directions on the respective positions. Mode \mathbf{J}_1 does not fulfill the additional boundary condition, since the initial surface current is oriented almost in the same direction along the dipole. Hence, the surface current distribution is null at the positions of the selective mutual coupling to fulfill the additional boundary condition (8.9). The current distribution of mode \mathbf{J}_1 is compressed toward the center of the dipole (see Fig. 8-8). Therefore, the effective length decreases and the resonance frequency of mode \mathbf{J}_1 increases to 2.175 GHz. Since the surface current magnitude is null at the positions of the selective mutual coupling, the influence of the inductor L on the eigenvalue λ_1 is small. Mode \mathbf{J}_2 fulfills the additional boundary condition and hence the surface current distribution of this mode is less affected by the position of the selective mutual coupling. The inductor L is used in order to modify the resonance frequency of mode \mathbf{J}_2 selectively. A comparison of

8.2 Eigenvalue Manipulation by Reactive Loading

the surface current distribution of mode $\mathbf{J}_{1,2}$ reveals two positions where one mode has a relatively high magnitude while the other exhibits a null. Hence, two ports can be inserted in order to excite mode $\mathbf{J}_{1,2}$ selectively, as denoted in Fig. 8-8. This two-port antenna system is matched at 2.2 GHz and offers good isolation of the ports, as can be observed from Fig. 8-9.

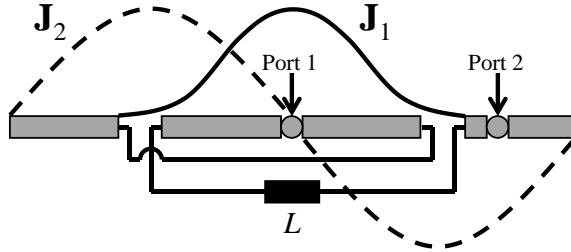


Fig. 8-8 A dipole configuration with selective mutual coupling ($Z_L=j\omega L$) and two ports. © IEEE 2015 [Saf15].

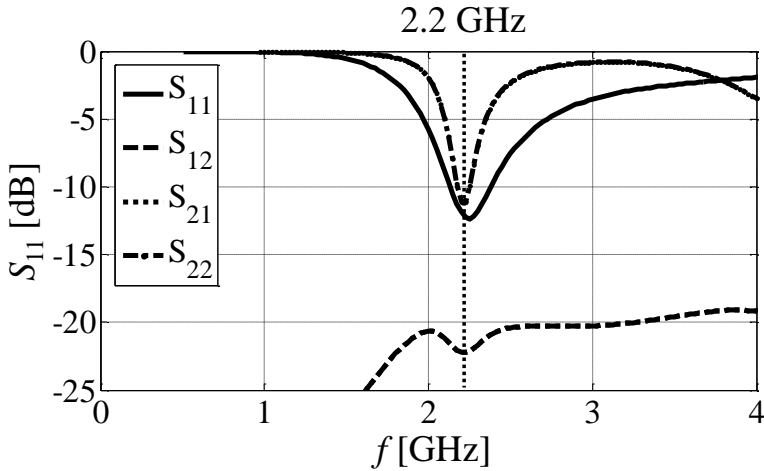


Fig. 8-9 Reflection coefficient of a dipole with a selective mutual coupling and two ports. © IEEE 2015 [Saf15].

In theory there is no restriction on the placement of the reactive elements between different parts of the structure. However, from the practical point of

8. Reactive Loading in the TCM

view, some configurations may not be realizable straight away. An ideal connection of the two parts of the structure with a lumped inductor L is contradictory to the idea of concentrated elements. However, although the theory may suggest structures that are difficult to realize in practice one might be able to think of practical solutions for some of them. One possible solution is shown in Fig. 8-10. The figure shows the 3D model (Fig. 8-10 a-c)) of a dipole with selective mutual coupling between two parts. The connection between the two positions and the inductance L are realized with four half-wavelength coaxial cables as sketched in Fig. 8-10 d). In this example, the outer conductor of the coaxial cable is used as the radiating structure.

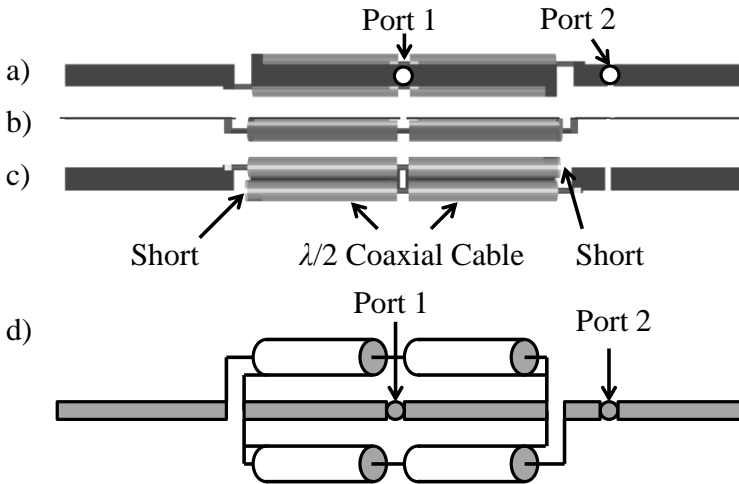


Fig. 8-10 Two-port dipole setup with four half wavelength coaxial cables, a) top view, b) side view, c) bottom view. The coaxial cables are connected, as denoted in the sketch d). © IEEE 2015 [Saf15].

The result of this multi-port antenna system is shown in Fig. 8-11. A reasonable impedance matching and decoupling between the two ports around 2.1 GHz is achieved.

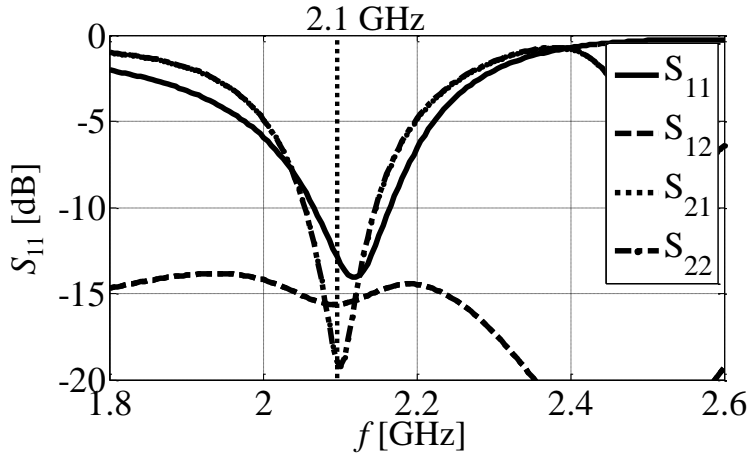


Fig. 8-11 Reflection coefficient of a practical realization of a dipole with a selective mutual coupling. The results are obtained with Empire XPU [EMP] © IEEE 2015 [Saf15].

8.3 Impedance Matching Network

In Chapter 8.2, two concepts are presented to modify the eigenvalue and the modal surface current distribution with concentrated reactive components placed in predefined positions on the antenna. A restriction of the location — where the elements can be placed on the feeding port location — gives a more important case for the practical realizations of antenna concepts. In this case, the lumped reactive component is a concentrated impedance matching network. Such a network can consist of multiple components; typically, it is also important to account for the losses of the network. In this section, the influence of the network on the characteristic modes is investigated by including the network in the eigenvalue analysis.

Assume an arbitrary two-port network represented by its impedance matrix \mathbf{Z}_{MN} . The antenna structure (e.g. dipole) is connected to the network at the ν -th edge element. The voltage between the network ports is related to the current by

$$\begin{pmatrix} U_1 \\ U_2 \end{pmatrix} = \begin{pmatrix} Z_{11} & Z_{12} \\ Z_{21} & Z_{22} \end{pmatrix} \begin{pmatrix} I_1 \\ I_2 \end{pmatrix}. \quad (8.11)$$

From Fig. 8-12 it can be observed that the current on the ν -th edge element I_ν is equal to the negative current I_2 and hence already included in the vector \mathbf{J} of the MoM matrix formulation.

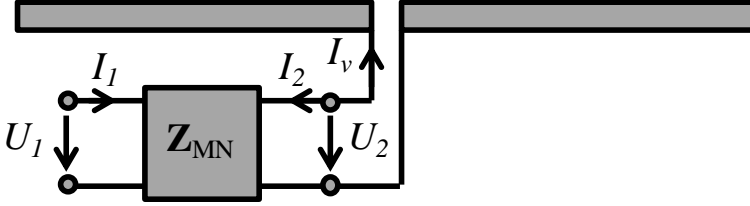


Fig. 8-12 A center-fed dipole having a length of 120 mm connected to an impedance matching network. © IEEE 2015 [Saf15].

The current I_1 is an additional unknown which has to be calculated by the MoM. Therefore, the column vector \mathbf{J} is extended by the current I_1 . Consequently, the formulation for the MoM equation yields:

$$\begin{bmatrix} \mathbf{V} \\ U_1 \end{bmatrix} = \underbrace{\begin{bmatrix} \mathbf{Z} + \mathbf{Z}_{22} & \mathbf{Z}_{21} \\ \mathbf{Z}_{12} & Z_{11} \end{bmatrix}}_{\mathbf{Z}_s} \cdot \begin{bmatrix} \mathbf{J} \\ I_1 \end{bmatrix}. \quad (8.12)$$

In (16) the matrices are defined as:

$$\mathbf{Z}_{22} = \text{diag}[0 \quad \cdots \quad Z_{22}l_\nu^2 \quad \cdots \quad 0], \quad (8.13)$$

$$\mathbf{Z}_{21} = [0 \quad \cdots \quad -Z_{21}l_\nu \quad \cdots \quad 0]^T, \quad (8.14)$$

$$\mathbf{Z}_{12} = [0 \quad \cdots \quad -Z_{12}l_\nu \quad \cdots \quad 0], \quad (8.15)$$

$$\mathbf{V} = [0 \quad \cdots \quad \cdots \quad \cdots \quad 0]^T. \quad (8.16)$$

For a linear network, the entire impedance matrix of the overall system \mathbf{Z}_S in (8.12) is symmetrical ($Z_{12}=Z_{21}$). The characteristic modes of the entire system \mathbf{Z}_S , including the matching network, are calculated in accordance with (4.1).

In the case of a lossless matching network and a lossless antenna structure, the characteristic modes of the extended impedance matrix \mathbf{Z}_S are still orthogonal to each other. The eigenvalues are real and allow a simple physical interpretation of the overall system. The resonance frequency of the characteristic modes can be determined by the eigenvalue, as it is directly related to the ratio of radiated and reactive power. In case the matching network contains losses, the characteristic modes of the entire system are no longer orthogonal to each other [Har72a]. Therefore, the modal far fields are no longer orthogonal. In order to treat this case, the modal efficiency will be defined in the next section.

8.4 Modal Efficiency

If losses are included in the matching network the power radiated by a certain characteristic mode is no longer identical to the power this mode carries. This can be accounted for by defining a modal efficiency:

$$\eta_n = \frac{P_{\text{rad},n}}{P_n} = \frac{1}{2Z_{F0}} \iint_{S' \rightarrow \infty} |\mathbf{E}_n|^2 dS , \quad (8.17)$$

The modal efficiency η_n is defined as the ratio of the radiated power $P_{\text{rad},n}$ of the n -th characteristic mode to the total power P_n this mode carries. According to the normalization used in the TCM, each mode carries a constant unit power of $P_n=1$:

$$\frac{1}{2} \langle \mathbf{J}_n, \text{Re}\{\mathbf{Z}_S\} \mathbf{J}_n \rangle = P_n = 1 , \quad (8.18)$$

The entire efficiency of the system can be written in the following equation:

8. Reactive Loading in the TCM

$$\eta = \frac{P_{\text{rad}}}{P_{\text{rad}} + P_{\text{loss}}} , \quad (8.19)$$

where P_{loss} is the total dissipated power of the overall system. The entire radiated power P_{rad} can be decomposed into its modal contributions according to

$$\begin{aligned} P_{\text{rad}} &= \frac{1}{2Z_{F0}} \iint_{S' \rightarrow \infty} \mathbf{E} \cdot \mathbf{E}^* dS = \frac{1}{2Z_{F0}} \iint_{S' \rightarrow \infty} \sum_{n=1}^{\infty} a_n \mathbf{E}_n \cdot \sum_{m=1}^{\infty} a_m^* \mathbf{E}_m^* dS \\ &= \sum_{n=1}^{\infty} \sum_{m=1}^{\infty} a_n \sqrt{\eta_n} a_m^* \sqrt{\eta_m} \rho_{n,m} . \end{aligned} \quad (8.20)$$

As the modal far fields are not orthogonal to each other in case of losses, we have to include the envelope correlation $\rho_{n,m}$ of the modes in (8.20) with

$$\rho_{n,m} = \frac{\iint_{S' \rightarrow \infty} \mathbf{E}_n \cdot \mathbf{E}_m^* dS}{\sqrt{\iint_{S' \rightarrow \infty} |\mathbf{E}_n|^2 dS} \sqrt{\iint_{S' \rightarrow \infty} |\mathbf{E}_m|^2 dS}} , \quad (8.21)$$

Substituting (8.20) into (8.19) yields

$$\eta = \sum_{n=1}^{\infty} \sum_{m=1}^{\infty} b_n \sqrt{\eta_n} b_m^* \sqrt{\eta_m} \rho_{n,m} , \quad (8.22)$$

In (8.22), b_n is the normalized coefficient of the n -th mode, given by

$$b_n = \frac{a_n}{P_{\text{rad}} + P_{\text{loss}}} = \frac{a_n}{\frac{1}{2} \text{Re} \{ \langle \mathbf{J}^* , \mathbf{Z}_S \mathbf{J} \rangle \}} , \quad (8.23)$$

In order to illustrate the applicability of the decomposition, the initial dipole antenna with an additional lossy network located at the feed port (please see Fig. 8-12) is discussed.

8.5 Example

The matching network is of Π -topology and an additional resistor is used to represent the losses of the system (see Fig. 8-13). The values of the components (L_1 , L_2 and C) are selected to match the input impedance of the center fed dipole at 2.2 GHz.

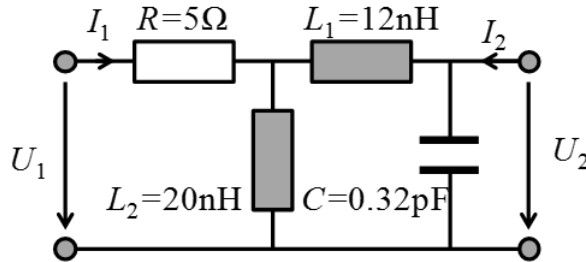


Fig. 8-13 Impedance matching network with a Π -topology and an additional resistor. © IEEE 2015 [Saf15].

The matching network in Fig. 8-13 is included in the eigenvalue analysis, as explained in Chapter 8.3. An illustration of the four most significant characteristic modes at 2.2 GHz is shown in Fig. 8-14. The conspicuously strong deformation of the surface current distribution of mode \mathbf{J}_1 reveals a high correlation to modes $\mathbf{J}_{3,4}$.

The eigenvalue of the modified modes is shown in Fig. 8-15. It can be observed that the eigenvalue λ_1 changes drastically above 1 GHz compared to the initial configuration without the matching network. The high magnitude of this eigenvalue makes it difficult to excite mode \mathbf{J}_1 at the desired frequency of $f = 2.2$ GHz. It is interesting to note that modes \mathbf{J}_2 and \mathbf{J}_4 show almost identical behavior with a resonance at $f_{\text{res};2,4} = 2.375$ GHz (please see Fig. 8-15). Hence, a good impedance matching can be obtained around the desired frequency range (please see Fig. 8-17). The new mode \mathbf{J}_4 improves the impedance behavior, because its resonance appears near the desired frequency, and its frequency

8. Reactive Loading in the TCM

behavior exhibits a small gradient.

The modal efficiency η_n and the entire radiation efficiency η are shown in Fig. 8-18. A frequency-dependent modal efficiency of modes $\mathbf{J}_{1,3,4}$ can be observed, while the modal efficiency of mode \mathbf{J}_2 is high in the entire frequency range. Because of this behavior, along with the fact that the eigenvalue λ_2 is less affected, we can conclude that the matching network has no significant influence on mode \mathbf{J}_2 because of the position of the matching network.

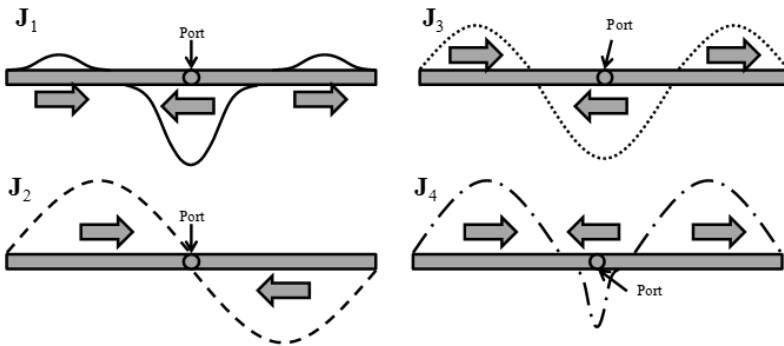


Fig. 8-14 Four characteristic modes of a dipole with an impedance matching network at the center. The lines denote the magnitude and the arrows denote the direction of the modal surface current distribution at 2.2 GHz. © IEEE 2015 [Saf15].

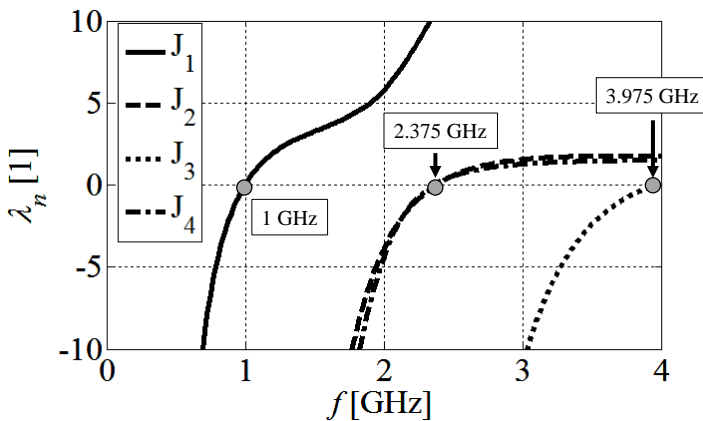


Fig. 8-15 Eigenvalue of four characteristic modes of a dipole with a matching network. © IEEE 2015 [Saf15].

TABLE 8-1
 FAR FIELD CORRELATION OF THE FOUR CHARACTERISTIC MODES OF A DIPOLE IN THE PRESENCE
 OF A MATCHING NETWORK AT 2.2 GHz

$ \rho_{n,m} $	\mathbf{J}_1	\mathbf{J}_2	\mathbf{J}_3	\mathbf{J}_4
\mathbf{J}_1	1	0.04	0.32	0.90
\mathbf{J}_2	0.04	1	0.00	0.01
\mathbf{J}_3	0.32	0.00	1	0.10
\mathbf{J}_4	0.90	0.01	0.10	1

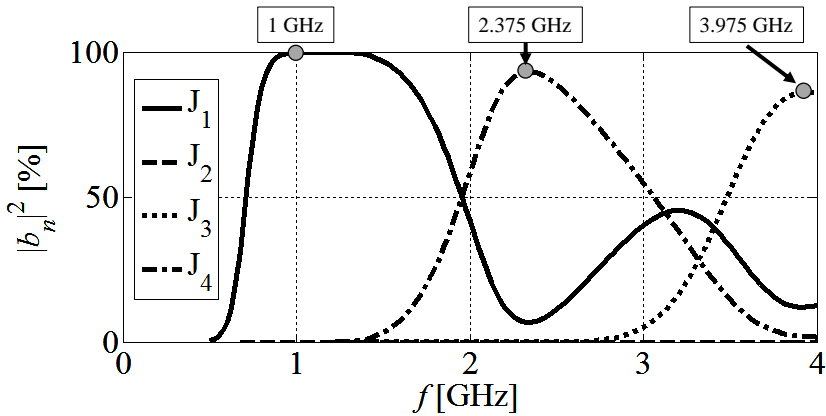


Fig. 8-16 Normalized weight coefficient of a center-fed dipole for four characteristic modes.
 © IEEE 2015 [Saf15].

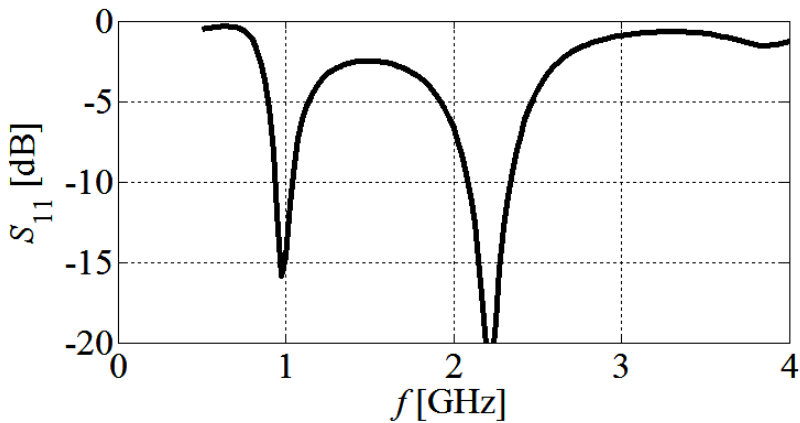


Fig. 8-17 Reflection coefficient of a center-fed dipole in the presence of a matching network.
 © IEEE 2015 [Saf15].

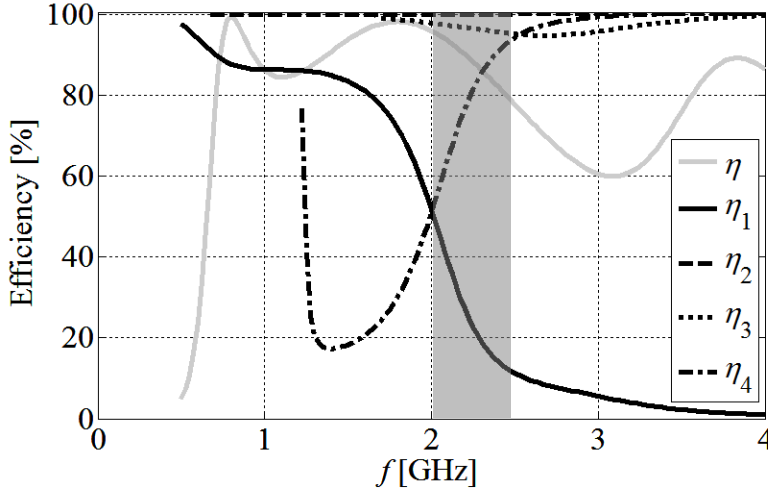


Fig. 8-18 Modal efficiency of four characteristic modes and the radiation efficiency of a dipole with a matching network. © IEEE 2015 [Saf15].

The summation of the normalized coefficients b_n and the modal efficiency η_n yields the radiation efficiency η , as denoted in (8.22) and shown in Fig. 8-18. At 1 GHz, the total efficiency η is equal to the efficiency η_1 of mode \mathbf{J}_1 , as the dipole configuration mainly excites this characteristic mode. At 2.2 GHz, the center-fed dipole excites mainly two modes, \mathbf{J}_1 and \mathbf{J}_4 (please see Fig. 8-16), with a modal efficiency of $\eta_1 = 77\%$ and $\eta_4 = 27\%$. Owing to the high correlation ($\rho_{1,4} = 0.90$) of these modes, the decomposition of the radiation efficiency in (8.22) is investigated. The focus lies on the coupling term between modes \mathbf{J}_1 and \mathbf{J}_4 . The coupling term is

$$b_1(b_4)^* \rho_{1,4} + b_4(b_1)^* \rho_{4,1} = 2|b_1||b_2||\rho_{1,4}| \cos \left(\underbrace{\arg \{b_1 b_4^* \rho_{1,4}\}}_{44^\circ} \right). \quad (8.24)$$

The phase in (8.24) is affected only by the normalized coefficients $b_{1,4}$ (since $\arg\{\rho_{1,4}\} = 0^\circ$). The total radiation efficiency η is enhanced in such a way that

the losses of the modes $\mathbf{J}_{1,4}$ are compensated around 2.2 GHz. In order to maximize this effect, the excitation of the modes should be modified to minimize the phase difference. As can be observed from Fig. 8-18 the total efficiency η decreases around 3 GHz. This is caused by the low efficiency of mode \mathbf{J}_1 on the one hand, and the additional phase difference between mode $\mathbf{J}_{1,4}$ of 180° in the respective coupling terms on the other hand. Since the antenna is not matched at this frequency, the effect of the phase difference is less significant. However, for a systematic antenna design, this effect should be known and evaluated for the given antenna structure.

Chapter 9

Characteristic Modes for Dielectric Bodies

The challenge to calculate and find an appropriate interpretation of the characteristic modes for dielectric materials has arisen in recent years. Since the introduction of the dielectric characteristic modes by Harrington in [Har72a] the extended theory has not been used for antenna design. Although the theory shows potential for the Dielectric Resonator Antenna (DRA) design, some problems have not been solved yet. The numerical calculation is one challenge that requires a lot of memory and computational effort. Furthermore, the interpretation of the dielectric characteristic modes is the most important challenge that requires more research.

9.1 Dielectric Characteristic Modes Computation

The dielectric mode calculation requires a system matrix with the PMCHWT formulation, as explained in Chapter 3.3 and in Chapter 4.3. Such system matrix is not symmetrical and requires additional modifications, as introduced in [Har72a]. In order to make the system matrix symmetrical, the magnetic current \mathbf{M} (\mathbf{I}_m in (4.14)) and the magnetic field \mathbf{H} (\mathbf{V}_m in (4.14)) is multiplied with the imaginary unit j . The dielectric characteristic mode \mathbf{W}_n in (4.16) consists of the electric current \mathbf{J}_n and the magnetic current \mathbf{M}_n , which has a constant

9. Characteristic Modes for Dielectric Bodies

phase shift of 90° due to the imaginary unit j .

The total surface current \mathbf{W} , which is represent by the electric current \mathbf{J} and the magnetic current \mathbf{M} , is superimposed with the dielectric characteristic modes with:

$$\mathbf{W} = \sum_{n=1}^{\infty} \mathbf{W}_n = \sum_{n=1}^{\infty} \begin{bmatrix} \mathbf{J}_n \\ j\mathbf{M}_n \end{bmatrix}. \quad (9.1)$$

The calculation of the dielectric characteristic modes with the PMCHWT formulation requires the usage of the RWG basis function for the electric current \mathbf{J} and the magnetic current \mathbf{M} . If a simple homogeneous dielectric material is considered, the same mesh is used for both currents. Since the number of unknowns is doubled, the size of the system matrix \mathbf{T} is four times larger than in the PEC case. The matrix element calculation requires additional numerical techniques suitable for the EFIE and MFIE. Hence, the time required to calculate the overall matrix is larger. In addition to the matrix calculation the eigenvalue decomposition with the available program libraries requires more time and more memory to save the data.

The common eigenvalue decomposition (4.15) has another important aspect related to the general mode interpretation. The eigenvalue calculation with (4.15) reveals the internal modes of the cavity and the external modes, which are usually of interest. The internal modes do not radiate power in free space, but they represent the complex field distribution within the objects and they are needed to describe the internal fields. In [Che15], a method is presented to simplify the eigenvalue equation and to exclude those internal modes from the mode calculation. Since the internal modes provide less information for the antenna design, they are not desired in the TCM analysis.

9.2 Problem of the Physical Interpretation of the Eigenvalue

The problem of the physical interpretation of the eigenvalue has been mentioned by Harrington in [Har72a] and is discussed further in [Che15]. The eigenvalue λ_n in (4.15) is not related to the reactive power of the overall system, as was the case for PEC bodies. Hence, this parameter cannot be used to determine the resonance of modes. In order to explain this issue, the active and reactive power of the equivalent surface problem is discussed. The real part of the system matrix \mathbf{T} can be used to determine the active power — respectively, the radiated power — if no loss is assumed. The real part can be understood as:

$$\begin{aligned} \operatorname{Re} \left\{ \begin{bmatrix} \mathbf{I}_e \\ j\mathbf{I}_m \end{bmatrix}^H \cdot \mathbf{T} \cdot \begin{bmatrix} \mathbf{I}_e \\ j\mathbf{I}_m \end{bmatrix} \right\} &= \operatorname{Re} \left\{ \begin{bmatrix} \mathbf{I}_e \\ j\mathbf{I}_m \end{bmatrix}^H \cdot \begin{bmatrix} \mathbf{V}_e \\ j\mathbf{V}_m \end{bmatrix} \right\} \\ &= \operatorname{Re} \left\{ \iint_S (\mathbf{J}^* \mathbf{E} + \mathbf{M}^* \mathbf{H}) dS \right\}. \end{aligned} \quad (9.2)$$

Next, the real part is separated with:

$$\begin{aligned} &\operatorname{Re} \left\{ \iint_S (\mathbf{J}^* \mathbf{E} + \mathbf{M}^* \mathbf{H}) dS \right\} \\ &= \frac{1}{2} \left(\iint_S (\mathbf{J}^* \mathbf{E} + \mathbf{M}^* \mathbf{H}) dS + \left(\iint_S (\mathbf{J}^* \mathbf{E} + \mathbf{M}^* \mathbf{H}) dS \right)^* \right) \\ &= \frac{1}{2} \left(\iint_S (\mathbf{J}^* \mathbf{E} + \mathbf{M}^* \mathbf{H}) dS + \iint_S (\mathbf{J} \mathbf{E}^* + \mathbf{M} \mathbf{H}^*) dS \right) \\ &= \frac{1}{2} \left(\iint_S (\mathbf{J}^* \mathbf{E} + \mathbf{M} \mathbf{H}^*) dS + \iint_S (\mathbf{J} \mathbf{E}^* + \mathbf{M}^* \mathbf{H}) dS \right) \\ &= \operatorname{Re} \left\{ \iint_S (\mathbf{J}^* \mathbf{E} + \mathbf{M} \mathbf{H}^*) dS \right\} = P_{\text{rad}} + P_{\text{Loss}}. \end{aligned} \quad (9.3)$$

9. Characteristic Modes for Dielectric Bodies

From (9.3), it is evident that the real part of the operation (9.2) gives the active power of the system. Hence, the same principle holds for the dielectric characteristic modes.

The imaginary part of the operation (9.2) is:

$$\begin{aligned} \text{Im} \left\{ \begin{bmatrix} \mathbf{I}_e \\ j\mathbf{I}_m \end{bmatrix}^H \cdot \mathbf{T} \cdot \begin{bmatrix} \mathbf{I}_e \\ j\mathbf{I}_m \end{bmatrix} \right\} &= \text{Im} \left\{ \begin{bmatrix} \mathbf{I}_e \\ j\mathbf{I}_m \end{bmatrix}^H \cdot \begin{bmatrix} \mathbf{V}_e \\ j\mathbf{V}_m \end{bmatrix} \right\} \\ &= \text{Im} \left\{ \iint_S (\mathbf{J}^* \mathbf{E} + \mathbf{M}^* \mathbf{H}) dS \right\}. \end{aligned} \quad (9.4)$$

By applying the same principle, the imaginary part of (9.4) is separated into:

$$\begin{aligned} &\text{Im} \left\{ \iint_S (\mathbf{J}^* \mathbf{E} + \mathbf{M}^* \mathbf{H}) dS \right\} \\ &= \frac{1}{2} \left(\iint_S (\mathbf{J}^* \mathbf{E} + \mathbf{M}^* \mathbf{H}) dS - \left(\iint_S (\mathbf{J}^* \mathbf{E} + \mathbf{M}^* \mathbf{H}) dS \right)^* \right) \\ &= \frac{1}{2} \left(\iint_S (\mathbf{J}^* \mathbf{E} - \mathbf{M} \mathbf{H}^*) dS - \iint_S (\mathbf{J} \mathbf{E}^* - \mathbf{M}^* \mathbf{H}) dS \right) \\ &= \text{Im} \left\{ \iint_S (\mathbf{J}^* \mathbf{E} - \mathbf{M} \mathbf{H}^*) dS \right\} \\ &\neq P_{\text{react}}. \end{aligned} \quad (9.5)$$

From (9.5), it becomes obvious that the imaginary part of the operation (9.4) is not related to the reactive power due to the minus sign inside the surface integral. Hence, the eigenvalue is not related to the reactive power of modes, as was the case for PEC bodies. This fact harms the physical interpretation of the modes and the way in which they are used for the antenna design. This issue becomes more critical if lossy materials are included in the system matrix \mathbf{T} . The real part of the operation (9.2), which is used to diagonalize the real

part of the system matrix, does not reveal orthogonal radiation pattern, since

$$\begin{aligned}
 \operatorname{Re} \left\{ \begin{bmatrix} \mathbf{J}_n \\ j\mathbf{M}_n \end{bmatrix}^H \cdot \mathbf{T} \cdot \begin{bmatrix} \mathbf{J}_n \\ j\mathbf{M}_n \end{bmatrix} \right\} &= \operatorname{Re} \left\{ \iint_S (\mathbf{J}_n^* \mathbf{E}_n + \mathbf{M}_n \mathbf{H}_n^*) dS \right\} \\
 &= \operatorname{Re} \left\{ \frac{1}{2} \iint_S \mathbf{E}_n \times \mathbf{H}_n^* dS \right\} + \iiint_V \sigma |E_n|^2 dV \quad (9.6) \\
 &= P_{\text{rad},n} + P_{\text{Loss},n}
 \end{aligned}$$

is valid for the n -th mode. If a mode has high loss the correlation to the other modes increases, and can be unity in the worst case. In common antenna design concepts, the orthogonal property is used to find the optimal antenna placement on the chassis. Such concepts are aimed on low mutual coupling of the feeding ports. The dielectric mode theory is, because of to the facts mentioned, impracticable. However, although the orthogonality is lost, if lossy materials are included, the eigenvalue can still be used to find the resonance of modes, even though the reactive power is not related with the eigenvalue. In (9.5) the reactive power can be determined for a single case. If the terms $(\mathbf{J}_n^* \mathbf{E}_n)$ and $(\mathbf{M}_n^* \mathbf{H}_n)$ in (9.5) are zero the imaginary part of the operation (9.2) — and, hence, the eigenvalue — determine the reactive power and, therefore, the resonance of modes:

$$\operatorname{Im} \left\{ \iint_S \begin{pmatrix} \mathbf{J}^* \mathbf{E} + \mathbf{M}^* \mathbf{H} \\ 0 \quad 0 \end{pmatrix} dS \right\} = P_{\text{react}} = 0 \quad (9.7)$$

Although the eigenvalue is not related to the reactive power the resonance can still be found in this special case. From that point of view, the dielectric characteristic modes for a Dielectric Resonator Antenna (DRA) are investigated in the next section.

9.3 Validation of the Dielectric Characteristic Modes with DRA

The Dielectric Resonator Antennas (DRAs) have been investigated for decades now, and they are used in many applications. The main advantage of the DRA is the low form factor, low cost and high gain. For the cylindrical DRA, the analytic mode decomposition is available in literature, e.g., cylindrical DRA antenna [Mon94]. The Characteristic Mode Theory — as presented in Chapter 3.3 and 4.3 — is used to calculate the modes. The eigenvalue is used to determine the resonance of a mode. Although the eigenvalue is not directly related to the reactive power, as explained previously, the resonance can still be found.

Four DRA modes are investigated, as shown in Fig. 9-1.

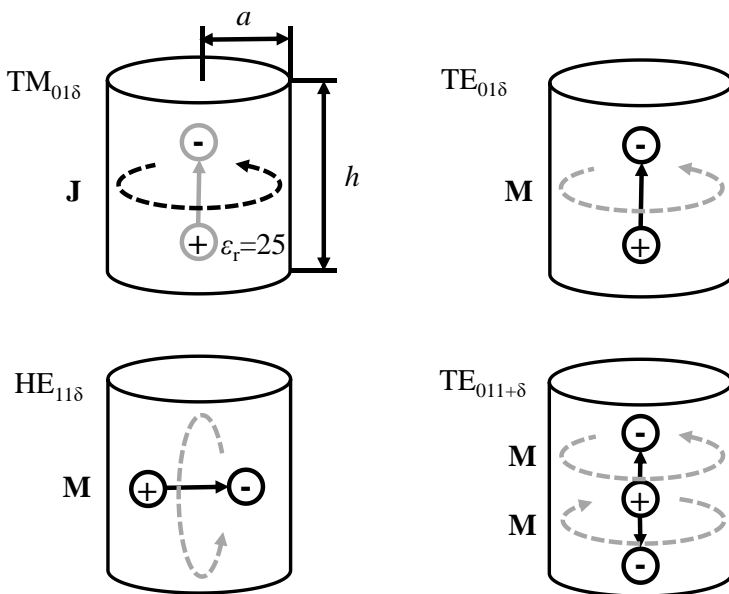


Fig. 9-1 Cylindrical modes of a DRA. The radius of the cylinder is $a = 0.3$ m and the height is $h = 0.6$ m. The cylinder is filled with a lossless homogeneous material with a relative permittivity of $\epsilon_r = 25$. The plus and minus denote a polarization of the electric current \mathbf{J} and magnetic current \mathbf{M} .

The TM and TE modes in Fig. 9-1 are the dipole and quadrupole modes along the extension of the cylinder. The HE mode is the horizontal dipole mode of the magnetic polarization M. For all four DRA modes, the resonance frequencies are available in closed form in [Mon94]:

$$f_{\text{res, TM-01}\delta} = \frac{c_0}{2\pi a} \frac{2.327}{\sqrt{\epsilon_r + 2}} \sqrt{3.83^2 + \left(\frac{\pi a}{h}\right)^2}, \quad (9.8)$$

$$f_{\text{res, TE-01}\delta} = \frac{c_0}{2\pi a} \frac{2.327}{\sqrt{\epsilon_r + 1}} \left(1 + 0.2123 \left(\frac{2a}{h}\right) - 0.00898 \left(\frac{2a}{h}\right)^2 \right), \quad (9.9)$$

$$f_{\text{res, HE-11}\delta} = \frac{c_0}{2\pi a} \frac{6.324}{\sqrt{\epsilon_r + 2}} \left(0.27 + 0.36 \left(\frac{a}{h}\right) + 0.02 \left(\frac{a}{h}\right)^2 \right), \quad (9.10)$$

$$f_{\text{res, TE-011}+\delta} = \frac{c_0}{2\pi a} \frac{2.208}{\sqrt{\epsilon_r + 1}} \left(1 + 0.7013 \left(\frac{2a}{h}\right) - 0.002713 \left(\frac{2a}{h}\right)^2 \right). \quad (9.11)$$

The same four modes, as shown in Fig. 9-1, can be identified by the electric and magnetic surface current distribution on the equivalent surface. In Fig. 9-2, the eigenvalues of these four characteristic modes are shown. The resonance frequency of the modes is determined by the zero eigenvalue point ($\lambda_n = 0$). A comparison of the respective resonance frequencies between the analytic solutions and the modal analysis is summarized in Table 9-1. It can be observed that the resonance frequencies show good agreement. Therefore, it can be concluded that the characteristic modes calculated from the eigenvalue equation (4.15) give similar modes, as known from the DRA.

At first appearance, it is not clear why this special case is valid at the natural resonances of the characteristic modes. In order to investigate this fact in more detail, the system matrix \mathbf{T} is reformulated to enable the computation of the

9. Characteristic Modes for Dielectric Bodies

reactive power and, therefore, the computation of all natural resonances.

TABLE 9-1
RESONANCE FREQUENCY OF THE CHARACTERISTIC MODES OF A DRA.

From [Mon94]	TCM
$f_{\text{res,TM-01}\delta} \approx 126 \text{ MHz}$	$f_{\text{res,J1}} \approx 122 \text{ MHz}$
$f_{\text{res,TE-01}\delta} \approx 87 \text{ MHz}$	$f_{\text{res,J2}} \approx 88 \text{ MHz}$
$f_{\text{res,HE-11}\delta} \approx 88 \text{ MHz}$	$f_{\text{res,J3}} \approx 88 \text{ MHz}$
$f_{\text{res,TE-011}+\delta} \approx 117 \text{ MHz}$	$f_{\text{res,J4}} \approx 117 \text{ MHz}$

The following formulation is introduced for the reactive power computation:

$$\begin{bmatrix} \mathbf{V}_e \\ -\mathbf{V}_m \end{bmatrix} = \underbrace{\begin{bmatrix} \mathbf{Z}_1 + \mathbf{Z}_2 & \mathbf{K}_1 + \mathbf{K}_2 \\ \mathbf{K}_1 + \mathbf{K}_2 & -(\mathbf{Y}_1 + \mathbf{Y}_2) \end{bmatrix}}_{\mathbf{T}_{\text{reac}}} \cdot \begin{bmatrix} \mathbf{I}_e \\ -\mathbf{I}_m \end{bmatrix}. \quad (9.12)$$

The modified system matrix \mathbf{T}_{reac} in (9.12) is used to determine the reactive power of the modes calculated with the initial system matrix \mathbf{T} . The eigenvalues and the reactive power of the first two modes (TE and TM) are shown in Fig. 9-3. It can be observed that the respective two curves intersect at the zero eigenvalue point, where the resonance of the modes can be found. Furthermore, from Fig. 9-3, it can be concluded that the reactive power is dominated by either the $(\mathbf{J}^* \mathbf{E})$ term or the $(\mathbf{M}^* \mathbf{H})$ term in (9.7). Near the resonance, a clear dominance of the electric or the magnetic current can be found. This fact is valid for the first resonance of the dielectric modes, but might be invalid for the resonances at the higher frequencies. Furthermore, the modified system matrix \mathbf{T}_{reac} can give more resonance frequencies, compared with the eigenvalue λ_n curves (please see TE₀₁ δ -Mode in Fig. 9-3). However, the eigenvalue can still be used to determine the first resonance frequency of the dielectric

modes. This parameter may be sufficient for the first guess on the DRA antenna design.

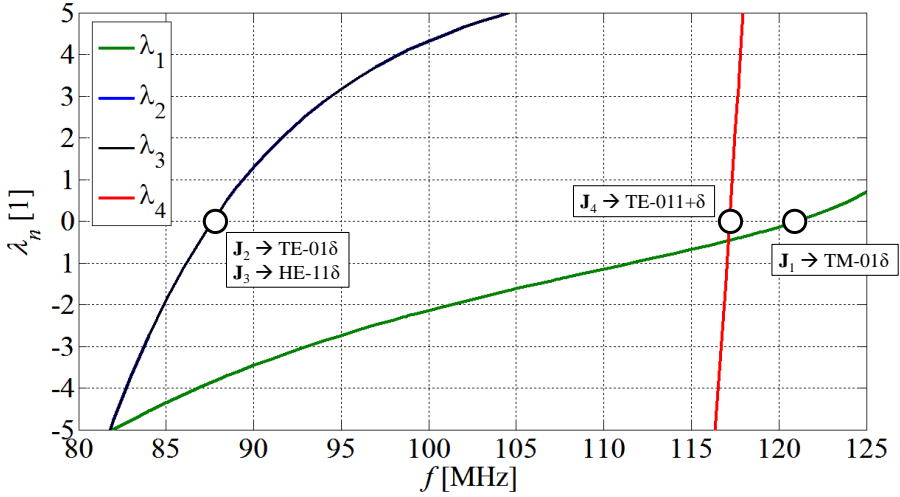


Fig. 9-2 Eigenvalue of four dielectric characteristic modes of a DRA.

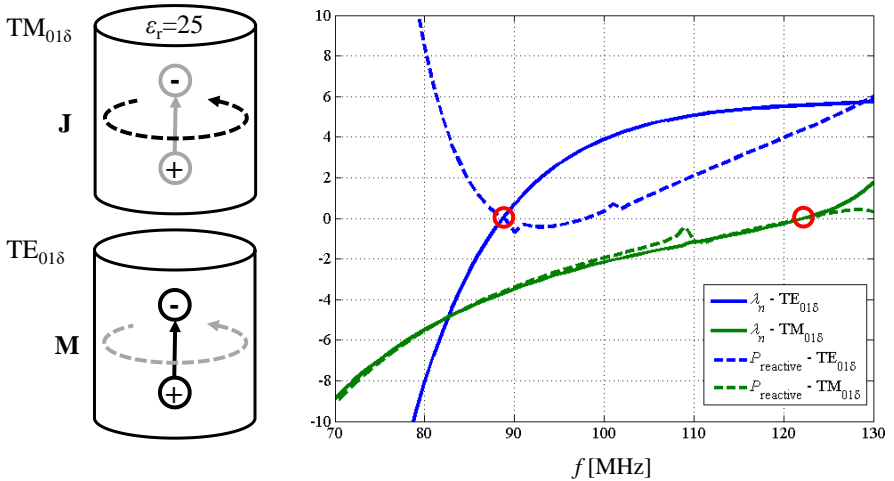


Fig. 9-3 Eigenvalue and the reactive power of the TM and TE modes of a DRA. The red circles denote the intersection of the respective curves and hence the resonance.

9.4 Influence of a Plastic Chassis on the Characteristic Modes of a Handheld Device.

The dielectric characteristic modes are difficult to understand and the numerical evaluation requires high computational effort due to the high complexity of the integral representation of the scattering problem. This could be the reason why the dielectric mode decomposition has not been widely used in the small antenna design so far. Even for the DRAs, this mode decomposition technique is not common till now. Many efforts have been made till now to overcome the problems mentioned and to make the technique more meaningful for the antenna design.

In this section, the influence of a plastic casing is investigated on a small terminal with the proposed concept. A small ground plane (the PCB made of PEC) is enclosed by a lossy dielectric material (here a plastic casing, $\epsilon_r = 4$ and $\sigma = 0.001$ S/m) as denoted in Fig. 9-4. The resonance of the ground plane without the casing is compared with the dielectric mode.

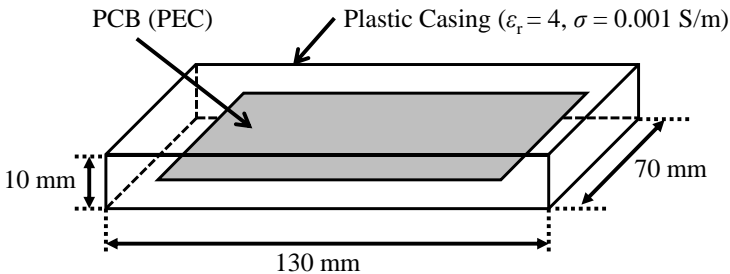


Fig. 9-4 Rectangular PCB (120 mm × 60 mm) surrounded by a plastic casing.

The eigenvalues of the first two modes of PEC ground plane and of the dielectric casing are shown in Fig. 9-5. Although the modes of the two problems are different in general, a similarity of the surface current on the PCB can be found. Hence the PEC modes on the PCB can be identified in the dielectric material

case. In Fig. 9-5, it can be seen that eigenvalues of the modes show similar curves, but with a small frequency shift. The resonance frequency of the first mode \mathbf{J}_1 (dipole mode in horizontal direction) is shifted $\Delta f = 150$ MHz down the frequency. The resonance shift of the second mode \mathbf{J}_2 (dipole mode in vertical direction) is higher, and is around $\Delta f = 700$ MHz.

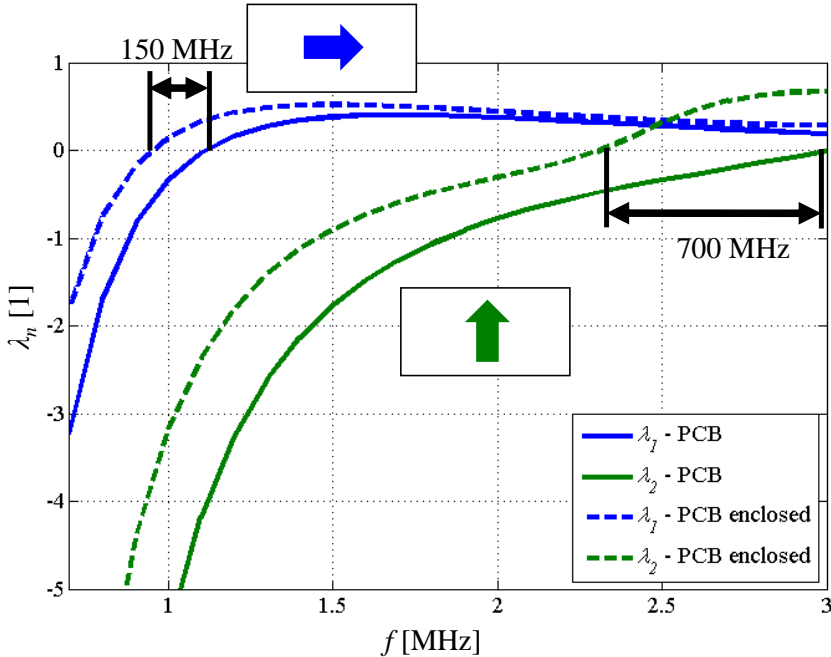


Fig. 9-5 Eigenvalues of the PEC modes and the eigenvalues of the dielectric modes.

A resonance shift caused by the presence of a dielectric casing is not surprising for the antenna designer. This fact has been known for many years, and is taken into account during the design steps. The TCM for dielectric materials can be used to estimate the possible resonance shift, which can be seen in the input impedance of a located feeding port on the PCB. Although this mode decomposition technique offers some interesting views inside the complex antenna

9. Characteristic Modes for Dielectric Bodies

design procedure, more effort and research is required to make this theory suitable for the designer.

Chapter 10

Application on the TCM

Since the introduction of the TCM in the 1970s, many antenna applications have benefited from the orthogonal property of the characteristic modes. The first known application that exploits the resonances of the modes was the automotive application in the 1990s [Mur94, Aus98]. The modes have been used to find the optimal antenna location on the vehicle body. In recent years, the TCM has been used to understand the radiation principle of the small antennas placed on a finite size ground plane, e.g., mobile phone [Mar11a, Mar11b, Mar12]. In the recent decades, the MIMO antenna design has grown rapidly due to the demand of the mobile phone market to serve high data rates. In [Mar14], a three-port antenna system has been integrated into a small chassis with a good isolation and impedance matching in the LTE frequency bands (E-UTRA Band 7, $2.5 \leq f [\text{GHz}] \leq 2.7$). The selective excitation of the orthogonal modes, with inductive coupling elements, has been developed and evaluated. In [Had14], this concept is extended toward the massive MIMO antenna array to reach extremely high data rate of 50 Gbits/s at $f = 7.25$ GHz.

In this chapter, the TCM is used to design a two-port antenna system for a

small hand-held device and for the automotive application. In both applications, the same concept of the combined mode excitation is used. A reconfigurable impedance matching network is designed and evaluated for both applications.

10.1 2-Port Antenna Concept for Small Terminal

The common way to integrate two antennas into a finite size ground plate is described in, e.g., [Mar11a]. The antennas are placed on the PCB in such a way that each port excites different modes within the frequency band aimed. This selective excitation concept requires more than one coupling element to excite the desired modes with a high purity. Such concept requires separate feeding network, including an impedance matching network at each port. The time to design each feeding network separately can be reduced significantly, if a single feeding network is used for all ports. The coupling elements must be placed with respect to the given symmetry of the finite size ground plane. It is clear that such a configuration will excite the same modes and a decoupling of the feeding ports might be unreachable. However, if the excitation phase of the modes is chosen well a high decoupling can, in principle, be reached. This combined excitation of the modes is described and validated with in the following.

Four capacitive coupling elements (CCE) are used in the MIMO antenna design concept, as denoted in Fig. 10-1. These coupling elements are predestined for a wide band impedance matching rather than the inductive coupling elements as described in [Mar11b, Mar11c]. Two CCEs are fed simultaneously with a feeding network, as denoted in the blue and yellow colors in Fig. 10-1. A power divider (PD) and a constant phase shifter (PS) of 180° are used to impress the electric current in the denoted orientation. The feeding networks

in the left and right sides are identical, and excite the same characteristic modes, but with a specific phase difference. This phase difference of 180° results into a de-correlated MIMO antenna system.

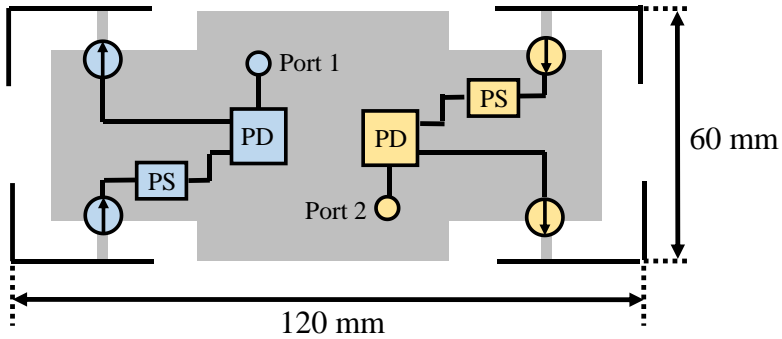


Fig. 10-1 MIMO antenna concept for a small terminal. Power divider (PD) and phase shifter (PS) with a constant phase shift of 180° are used in the feeding network.

In order to explain the influence of the phases in this concept a simplified case is investigated, where two modes are excited by the proposed configuration. Let us assume two modes $J_{4,5}$ (shown in Fig. 10-2), which are excited with equal magnitudes. The resonance frequencies of the two modes are not far away from each other (please compare Table 4-1) and the modal surface current is high at the respective feeding positions. These conditions facilitate the strong excitation of these two modes by the configuration.

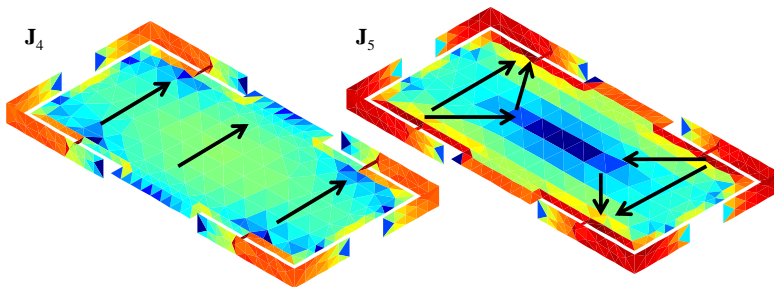


Fig. 10-2 Two significant characteristic modes of the small terminal which are excited by the given configuration.

10. Application on the TCM

Next, the envelope correlation is calculated by the normalized coefficient of modes ($b_{4,n}$ mode \mathbf{J}_4 excited by the n^{th} feeding port, $b_{5,n}$ mode \mathbf{J}_5 excited by the n^{th} feeding port) and, as explained in Chapter 6, are used to calculate the correlation between the two feeding ports. The correlation is, in this special case, as follows:

$$\begin{aligned}\rho_{1,2} &= b_{4,1}b_{4,2} + b_{5,1}b_{5,2} \\ &= e^{j180^\circ} \left| b_{4,1} \right| \left| b_{4,2} \right| + \left| b_{5,1} \right| \left| b_{5,2} \right| .\end{aligned}\quad (10.1)$$

The surface current direction of mode \mathbf{J}_4 shows opposite direction on the left and right side of the chassis (please compare Fig. 10-2). For this reason a 180° phase term is added in (10.1) and the correlation is reasonably close to zero.

$$\rho_{1,2} = e^{j180^\circ} \left| b_{4,1} \right| \left| b_{4,2} \right| + \left| b_{5,1} \right| \left| b_{5,2} \right| \approx 0 .\quad (10.2)$$

Although the correlation is not exactly zero and more modes are excited in general, especially at the higher frequency range, this principle holds for the proposed antenna configuration.

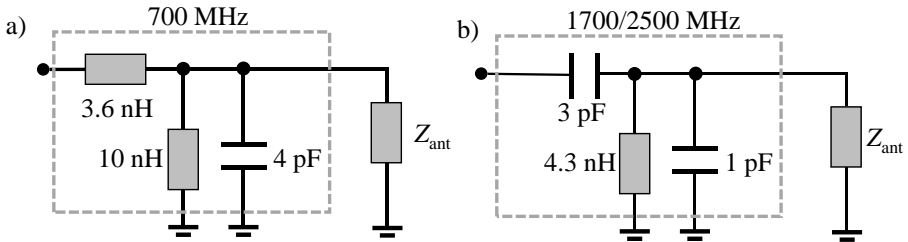


Fig. 10-3 Two impedance matching networks for the combined excitation of the characteristic modes. The network in a) match the antenna impedance around $f = 700$ MHz and the network in b) match the impedance at $f = 1.7$ GHz and $f = 2.5$ GHz.

This concept is used to fabricate a prototype and to demonstrate the capability of the combined mode excitation. The size of the CCE requires an impedance matching network to match the antenna, especially at the low frequency band.

In order to ensure the impedance matching at all desired frequency bands, a tuneable impedance matching is designed, as shown in Fig. 10-3 a) and b). A GaAs-Switch is used to toggle between the two networks depending on the operation frequency band aimed.

Each feeding network consists of a power divider, the tuneable impedance matching network — which is used for each CCE — and a transmission line for the phase difference of 180° (please see Fig. 10-4). The transmission line is the simplest possible way to realize a phase shift. The length of the transmission line is chosen to have a 180° phase shift at $f = 2.6$ GHz. This length is optimized for the combined mode excitation in the frequency bands desired. Although the length is not optimal for the, e.g., low frequency band, the proposed concept gives a reasonable result.

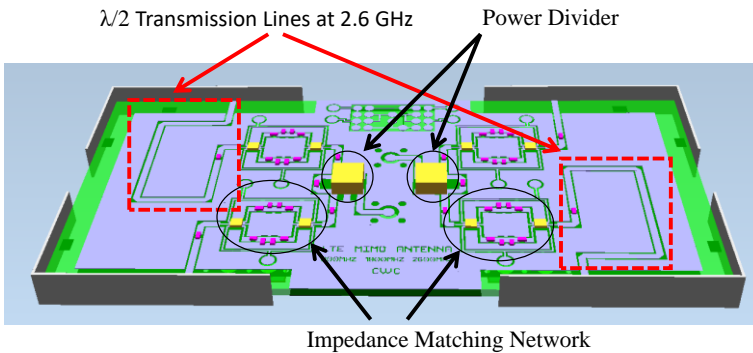


Fig. 10-4 3D model of the combined excitation concept for a small terminal.

In Fig. 10-5 a) and b), the top and the bottom views of the fabricated prototype are respectively shown. In Fig. 10-6, in Fig. 10-7 and in Fig. 10-8, the measured scattering parameter of the combined excitation concept is shown. It can be observed that a reasonable impedance matching ($|S_{ii}| \leq -6$ dB) and decoupling ($|S_{ij}| \leq -17$ dB) is reached in the frequency bands desired. The tree plots

10. Application on the TCM

shows the scattering parameters for different states of the reconfigurable impedance matching networks.

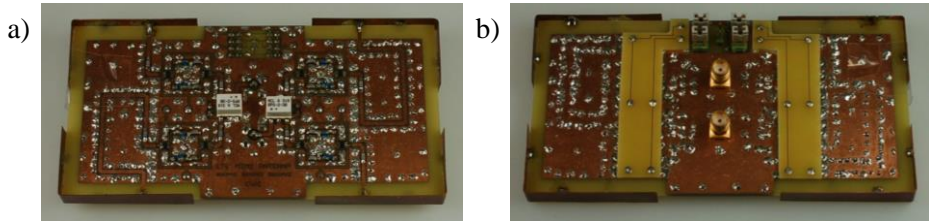


Fig. 10-5 Fabricated prototype in top view a) and bottom view b).

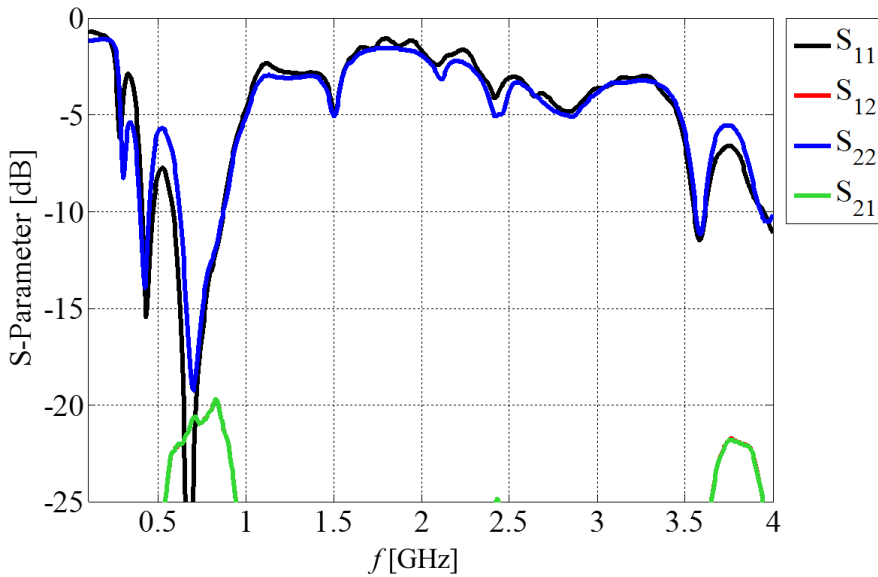


Fig. 10-6 Scattering parameter of the two-port antenna system at low state at $f = 700$ MHz.

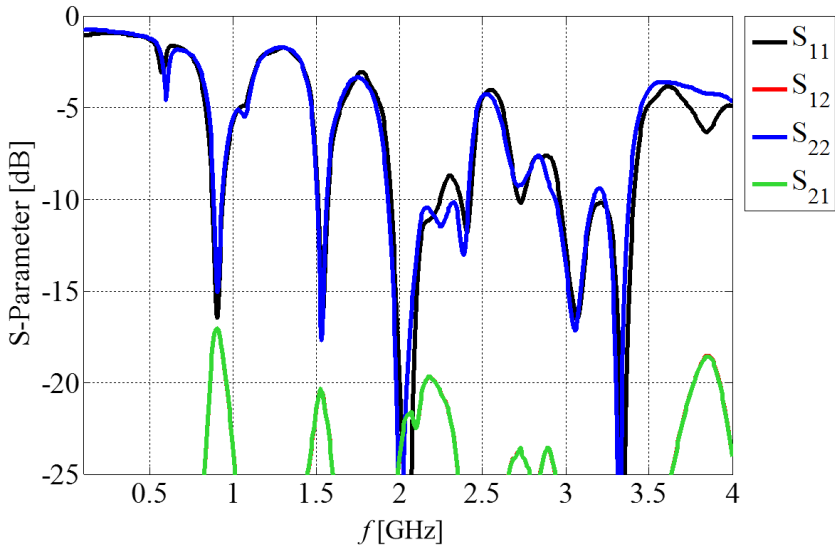


Fig. 10-7 Scattering parameter of the two-port antenna system at middle and high state ($f = 1.7/2.5$ GHz).

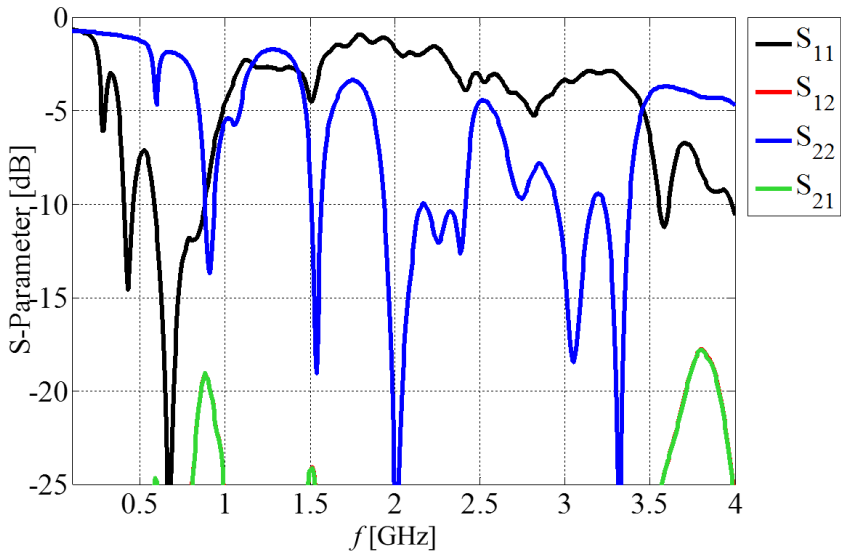


Fig. 10-8 Scattering parameter of the two-port antenna system at all states. The first port is matched around $f = 700$ MHz and the second port is matched at $f = 1.7$ GHz and $f = 2.5$ GHz.

10. Application on the TCM

The proposed combined mode excitation with the design feeding network and impedance matching network shows good results. However, the overall efficiency is less than $\eta < 20\%$ in the low frequency range. The reason for the high loss is founded in the transmission line which is designed to have a phase shift of 180° at a single frequency point. This transmission line causes standing waves, which reduce the overall efficiency. In order to overcome this problem, a 180° hybrid-power divider can be used to set a constant phase shift over a wide frequency range. This modification is used in the next application to design a two-port MIMO antenna in a rearview mirror of a vehicle with the combine excitation of characteristic modes.

10.2 2-Port Antenna Concept for Automotive Application

The combined mode excitation — as proposed in the previous section — is used to design and to integrate a two-port MIMO antenna system in a rearview mirror of a vehicle. The same principle, as explained for the small terminal, is used here, as shown in Fig. 10-9. The chassis and the CCEs are rescaled to fit into the rearview mirror of a vehicle.

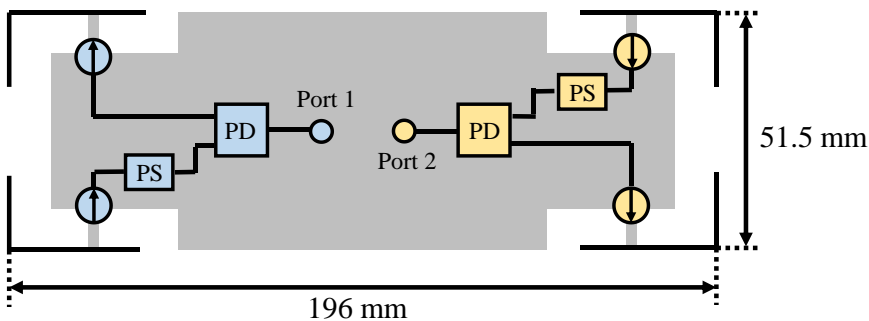


Fig. 10-9 MIMO antenna concept for a small terminal. Power divider (PD) and phase shifter (PS) with a constant phase shift of 180° are used in the feeding network.

Based on the experiences gathered from the small antenna design, a modification of the feeding network is applied to increase the overall efficiency. First, the phase shift and the power divider are combined into a single component, a 180° hybrid power divider. Second, the tuneable impedance matching network is located close to the excitation position of the respective CCEs. The impedance matching network contains lumped SMD components and a tuneable inductor, as denoted in Fig. 10-10. Four states are supported by the tuneable inductor having the value $L = \{3.5, 5, 6, 7.5 \text{ nH}\}$.

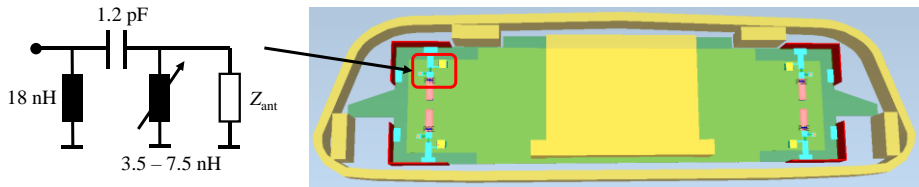


Fig. 10-10 3D model of the rearview mirror including the PCB with the four CCEs and the tuneable impedance matching network.

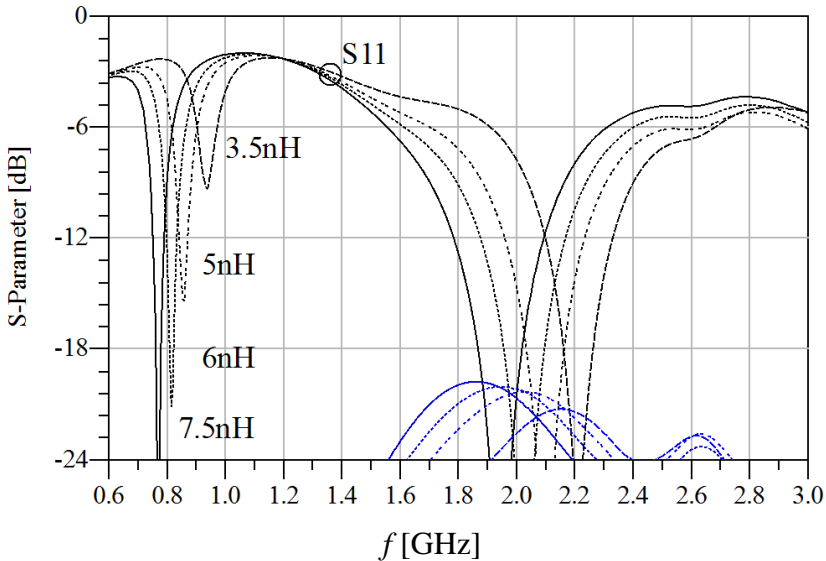


Fig. 10-11 Scattering parameter of the combined modes excitation integrated into a rearview mirror of a car.

10. Application on the TCM

The impedance matching of the feeding ports is shown in Fig. 10-11. In the desired LTE frequency ranges, a reasonable impedance matching is reached ($|S_{ii}| \leq -6$ dB), and decoupling ($|S_{ij}| \leq -20$ dB). The tuneable inductor is mainly used to reach a narrow band tuning of the low LTE frequency band ($725 \leq f$ [MHz] ≤ 970). The higher bands are less influenced by the tuning of the inductor. The overall efficiency of the proposed concept is around $\eta \approx 50\%$.

The radiation patterns of the integrated MIMO antenna system into the rear-view mirror are shown in Fig. 10-12 for three different frequencies a)–c). It can be observed that the main radiation for the $f = 800$ MHz and $f = 1800$ MHz frequency range is in the driving direction, while the radiation of the higher frequency band ($f = 2600$ MHz) is toward the sky. Furthermore, the radiation pattern of the high frequency band reveals a spiky form, which is typical known from the automotive antenna design.

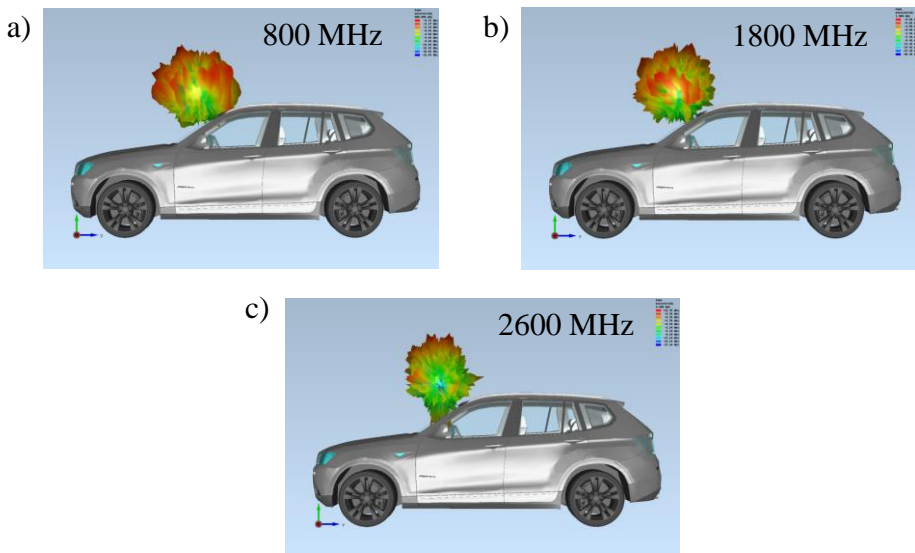


Fig. 10-12 Radiation pattern of a MIMO antenna system integrated into a rearview mirror of a vehicle.

Chapter 11

Conclusion

This thesis contributes new numerical methods and concepts for small antenna design with the Theory of Characteristic Modes. The problem of tracking the eigenvalue over a wide frequency range is investigated. The degenerated mode effect on the common tracking algorithm is discussed, and a new algorithm is presented to improve the tracking. The capability and limitations of the new algorithm are discussed and tested for generic examples. The new algorithm provides a new opportunity to generate differentiable eigenvalue curves and, hence, other important parameters for the design of small antennas.

The modal source reconstruction is another interesting method to predict the mode contribution on a complex structure, based on a simplified structure. This method is a robust and powerful concept which allows to include other, not Method of Moment based, tools into the modal analysis. The theory for the reconstruction is presented and evaluated for simple examples and the popular iPhone4. Two similar algorithms are derived and tested. This method can be used as an additional validation process to evaluate the antenna performance, even for small terminals.

The influence of typical impedance matching techniques and the reactive

11. Conclusion

lumped elements are investigated intensively in this thesis. For this the modal admittance and impedance are introduced, based on the early published investigations. The convergence of the series expansion is investigated and a new equivalent circuit model is presented to estimate the remaining part resulting from the bad convergence issue. The model is tested for the inductive and capacitive coupling elements as a profound investigation for more complex antenna shapes. Hereinafter, the influence of lumped networks on the characteristic modes is investigated, and the resonance displacement is analyzed. It is shown that the concentrated network changes the modal surface current distribution on the chassis. The modal efficiency is introduced in case of lossy components.

The dielectric mode theory has been available for many decades but, till now, has been barely used in antenna design due to the problem of useful interpretation of the modes and their eigenvalues. This problem is discussed, and a single case is presented, where the eigenvalue gives the natural resonance of the modes. This is evaluated and compared for the dielectric resonator antenna, since analytic solutions are available for this case.

Finally, the combined mode excitation concept is introduced and a two-port MIMO antenna system is designed and integrated into a small terminal. A prototype is fabricated, and the overall performance evaluated. Based on this concept, the combined mode excitation is developed further and integrated into a rearview mirror of a vehicle. The influence of the vehicle's body is investigated and the radiation patterns are presented. The overall efficiency and the impedance matching are improved compared with the small terminal concept.

Appendix A

A1 Integral Equation

The calculation of the electromagnetic field within the media, requires a solution of the Maxwell's equations in frequency domain. For that, the media are assumed to be linear, homogeneous and isotropic. The complex permittivity and permeability of the i -th media, respectively, can be written with:

$$\varepsilon_i = \varepsilon_0 \varepsilon_{r,i} + \frac{\sigma_i}{j\omega}, \quad (\text{A1.1})$$

$$\mu_i = \mu_0 \mu_{r,i} + \frac{\sigma_{m,i}}{j\omega}. \quad (\text{A1.2})$$

In (A1.1) $\varepsilon_{r,i}$, σ_i , $\mu_{r,i}$ and $\sigma_{m,i}$ are the relative permittivity, electric conductivity, relative permeability and magnetic conductivity of the i -th media, respectively.

Any solution of the complex scattering field must satisfied the Maxwell's equations:

$$\nabla \times \mathbf{E}_s(\mathbf{r}) = -\mathbf{M}(\mathbf{r}) - j\omega\mu_i \mathbf{H}_s(\mathbf{r}), \quad (\text{A1.3})$$

$$\nabla \times \mathbf{H}_s(\mathbf{r}) = \mathbf{J}(\mathbf{r}) + j\omega\varepsilon_i \mathbf{E}_s(\mathbf{r}). \quad (\text{A1.4})$$

Furthermore, the tangential components between two media must be continuous:

$$\mathbf{n} \times \mathbf{E}(\mathbf{r}) = -\frac{1}{2} \mathbf{M}(\mathbf{r}), \quad (\text{A1.5})$$

$$\mathbf{n} \times \mathbf{H}(\mathbf{r}) = \frac{1}{2} \mathbf{J}(\mathbf{r}). \quad (\text{A1.6})$$

In order to derive the integral representation of the equations (A1.3) and (A1.4), the curl operator is used:

$$\nabla \times \nabla \times \mathbf{E}_s(\mathbf{r}) = -\nabla \times \mathbf{M}(\mathbf{r}) - j\omega\mu_i \nabla \times \mathbf{H}_s(\mathbf{r}), \quad (\text{A1.7})$$

$$\nabla \times \nabla \times \mathbf{H}_s(\mathbf{r}) = \nabla \times \mathbf{J}(\mathbf{r}) + j\omega\varepsilon_i \nabla \times \mathbf{E}_s(\mathbf{r}). \quad (\text{A1.8})$$

With the vector identity ($\nabla \times \nabla \times \mathbf{A} = \nabla[\nabla \cdot \mathbf{A}] - \nabla^2 \mathbf{A}$) these equations can be rewritten into:

$$\nabla^2 \mathbf{E}_s(\mathbf{r}) - \nabla[\nabla \cdot \mathbf{E}_s(\mathbf{r})] = \nabla \times \mathbf{M}(\mathbf{r}) + \underbrace{j\omega\mu_i \nabla \times \mathbf{H}_s(\mathbf{r})}_{(\text{A1.4})}, \quad (\text{A1.9})$$

$$\nabla^2 \mathbf{H}_s(\mathbf{r}) - \nabla[\nabla \cdot \mathbf{H}_s(\mathbf{r})] = -\nabla \times \mathbf{J}(\mathbf{r}) - \underbrace{j\omega\varepsilon_i \nabla \times \mathbf{E}_s(\mathbf{r})}_{(\text{A1.3})}. \quad (\text{A1.10})$$

Substituting (A1.4) and (A1.3) in (A1.9) and (A1.10) the following equations can be found:

$$\nabla^2 \mathbf{E}_s(\mathbf{r}) + k^2 \mathbf{E}_s(\mathbf{r}) = \nabla \times \mathbf{M}(\mathbf{r}) + j\omega\mu_i \mathbf{J}(\mathbf{r}) + \nabla[\nabla \cdot \mathbf{E}_s(\mathbf{r})], \quad (\text{A1.11})$$

$$\nabla^2 \mathbf{H}_s(\mathbf{r}) + k^2 \mathbf{H}_s(\mathbf{r}) = -\nabla \times \mathbf{J}(\mathbf{r}) + j\omega\varepsilon_i \mathbf{M}(\mathbf{r}) + \nabla[\nabla \cdot \mathbf{H}_s(\mathbf{r})]. \quad (\text{A1.12})$$

In (A1.11) and (A1.12), k_i is the complex wavenumber of the i -th media ($k_i^2 = \omega^2 \varepsilon_i \mu_i$).

The divergence of the electric and magnetic field is related to the electric and magnetic charge density ($\rho_e = \varepsilon_i [\nabla \cdot \mathbf{E}_s]$, $\rho_m = \mu_i [\nabla \cdot \mathbf{H}_s]$), respectively. Following this concept, we can derive:

$$\nabla^2 \mathbf{E}_s(\mathbf{r}) + k_i^2 \mathbf{E}_s(\mathbf{r}) = \nabla \times \mathbf{M}(\mathbf{r}) + j\omega\mu_i \mathbf{J}(\mathbf{r}) + \nabla \frac{\rho_e(\mathbf{r})}{\varepsilon_i}, \quad (\text{A1.13})$$

$$\nabla^2 \mathbf{H}_s(\mathbf{r}) + k_i^2 \mathbf{H}_s(\mathbf{r}) = -\nabla \times \mathbf{J}(\mathbf{r}) + j\omega\varepsilon_i \mathbf{M}(\mathbf{r}) + \nabla \frac{\rho_m(\mathbf{r})}{\mu_i}. \quad (\text{A1.14})$$

Equation (A1.13) and (A1.14) are the inhomogeneous Helmholtz Equation. These source distributions can be reformulated further into:

$$\begin{aligned} \nabla^2 \mathbf{E}_s(\mathbf{r}) + k_i^2 \mathbf{E}_s(\mathbf{r}) = \\ \nabla \times \mathbf{M}(\mathbf{r}) + j\omega\mu_i \mathbf{J}(\mathbf{r}) + \frac{1}{j\omega\varepsilon_i} \nabla [\nabla \cdot \mathbf{J}(\mathbf{r})] \end{aligned} \quad (\text{A1.15})$$

$$\begin{aligned} \nabla^2 \mathbf{H}_s(\mathbf{r}) + k_i^2 \mathbf{H}_s(\mathbf{r}) = \\ -\nabla \times \mathbf{J}(\mathbf{r}) + j\omega\varepsilon_i \mathbf{M}(\mathbf{r}) + \frac{1}{j\omega\mu_i} \nabla [\nabla \cdot \mathbf{M}(\mathbf{r})] \end{aligned} \quad (\text{A1.16})$$

The scattering field (\mathbf{E}_s , \mathbf{H}_s) can be constructed out of superposition of distributed point sources placed in the media. For that, the Green's function of the problem is used to superimpose the solution. If the point sources are placed in a homogeneously filled space, the Green's function is known, and the scattering field can be constructed with an integration over the point sources placed within a given volume V . The scattering field \mathbf{E}_s is now

$$\begin{aligned} \mathbf{E}_s(\mathbf{r}) = \int_V G_i(\mathbf{r}, \mathbf{r}') \nabla \times \mathbf{M}(\mathbf{r}') dV' \\ + \int_V G_i(\mathbf{r}, \mathbf{r}') \left[j\omega\mu_i \mathbf{J}(\mathbf{r}') + \frac{1}{j\omega\varepsilon_i} \nabla [\nabla \cdot \mathbf{J}(\mathbf{r}')] \right] dV' \end{aligned} \quad (\text{A1.17})$$

and the magnetic scattering field \mathbf{H}_s

$$\begin{aligned}
 \mathbf{H}_s(\mathbf{r}) = & -\int_V G_i(\mathbf{r}, \mathbf{r}') \nabla \times \mathbf{J}(\mathbf{r}') dV' \\
 & + \int_V G_i(\mathbf{r}, \mathbf{r}') \left[j\omega\epsilon_i \mathbf{M}(\mathbf{r}') + \frac{1}{j\omega\mu_i} \nabla [\nabla \cdot \mathbf{M}(\mathbf{r}')] \right] dV' .
 \end{aligned} \tag{A1.18}$$

Finally, these equation can be rewritten into a more convenient form:

$$\begin{aligned}
 \mathbf{E}_s(\mathbf{r}) = & \int_V G_i(\mathbf{r}, \mathbf{r}') \nabla \times \mathbf{M}(\mathbf{r}') dV' \\
 & + j\omega\mu_i \int_V \mathbf{J}(\mathbf{r}') G_i(\mathbf{r}, \mathbf{r}') dV' + \frac{1}{j\omega\epsilon_i} \nabla \int_V \nabla \cdot \mathbf{J}(\mathbf{r}') G_i(\mathbf{r}, \mathbf{r}') dV'
 \end{aligned} \tag{A1.19}$$

$$\begin{aligned}
 \mathbf{H}_s(\mathbf{r}) = & -\int_V G_i(\mathbf{r}, \mathbf{r}') \nabla \times \mathbf{J}(\mathbf{r}') dV' \\
 & + j\omega\epsilon_i \int_V \mathbf{M}(\mathbf{r}') G_i(\mathbf{r}, \mathbf{r}') dV' + \frac{1}{j\omega\mu_i} \nabla \int_V \nabla \cdot \mathbf{M}(\mathbf{r}') G_i(\mathbf{r}, \mathbf{r}') dV'
 \end{aligned} \tag{A1.20}$$

These Equations (A1.19) and (A1.20) are valid within a media, but not on the interface between two media. A modification is required to enable the treat of the source on the interface. Form the boundary condition (A1.5) and (A1.6), the general valid formulations can be achieved with the cross product of the surface normal \mathbf{n} .

$$\begin{aligned}
 \mathbf{n} \times \mathbf{E}_s(\mathbf{r}) = & \mathbf{n} \times \int_{\partial V} G_i(\mathbf{r}, \mathbf{r}') \nabla \times \mathbf{M}(\mathbf{r}') dS' - \frac{1}{2} \mathbf{M}(\mathbf{r}) \delta_s(\mathbf{r}) + \\
 & \mathbf{n} \times \left[j\omega\mu_i \int_{\partial V} \mathbf{J}(\mathbf{r}') G_i(\mathbf{r}, \mathbf{r}') dS' \right] + \\
 & \mathbf{n} \times \left[\frac{1}{j\omega\epsilon_i} \nabla \int_{\partial V} \nabla \cdot \mathbf{J}(\mathbf{r}') G_i(\mathbf{r}, \mathbf{r}') dS' \right]
 \end{aligned} \tag{A1.21}$$

$$\begin{aligned}
 \mathbf{n} \times \mathbf{H}_s(\mathbf{r}) = & -\mathbf{n} \times \int_{\partial V} G_i(\mathbf{r}, \mathbf{r}') \nabla \times \mathbf{J}(\mathbf{r}') dS' + \frac{1}{2} \mathbf{J}(\mathbf{r}) \delta_s(\mathbf{r}) + \\
 & \mathbf{n} \times \left[j\omega \varepsilon_i \int_{\partial V} \mathbf{M}(\mathbf{r}') G_i(\mathbf{r}, \mathbf{r}') dS' \right] + \\
 & \mathbf{n} \times \left[\frac{1}{j\omega \mu_i} \nabla \int_{\partial V} \nabla \cdot \mathbf{M}(\mathbf{r}') G_i(\mathbf{r}, \mathbf{r}') dS' \right]
 \end{aligned} \tag{A1.22}$$

In (A1.21) and (A1.22) δ_s is the Kroneker function defined with:

$$\delta_s(\mathbf{r}) = \begin{cases} 1, & r \in \partial V \\ 0, & r \notin \partial V \end{cases} . \tag{A1.23}$$

Since the integration is performed over the boundary of a volume equation (A1.21) and (A1.22) can be simplified into the final form:

$$\begin{aligned}
 \mathbf{n} \times \mathbf{E}_s(\mathbf{r}) = & \mathbf{n} \times \int_{\partial V} \nabla' G_i(\mathbf{r}, \mathbf{r}') \times \mathbf{M}(\mathbf{r}') dS' - \frac{1}{2} \mathbf{M}(\mathbf{r}) \delta_s(\mathbf{r}) + \\
 & \mathbf{n} \times \left[j\omega \mu_i \int_{\partial V} \mathbf{J}(\mathbf{r}') G_i(\mathbf{r}, \mathbf{r}') dS' \right] + \\
 & \mathbf{n} \times \left[\frac{1}{j\omega \varepsilon_i} \nabla \int_{\partial V} \nabla \cdot \mathbf{J}(\mathbf{r}') G_i(\mathbf{r}, \mathbf{r}') dS' \right]
 \end{aligned} \tag{A1.24}$$

$$\begin{aligned}
 \mathbf{n} \times \mathbf{H}_s(\mathbf{r}) = & -\mathbf{n} \times \int_{\partial V} \nabla' G_i(\mathbf{r}, \mathbf{r}') \times \mathbf{J}(\mathbf{r}') dS' + \frac{1}{2} \mathbf{J}(\mathbf{r}) \delta_s(\mathbf{r}) + \\
 & \mathbf{n} \times \left[j\omega \varepsilon_i \int_{\partial V} \mathbf{M}(\mathbf{r}') G_i(\mathbf{r}, \mathbf{r}') dS' \right] + \\
 & \mathbf{n} \times \left[\frac{1}{j\omega \mu_i} \nabla \int_{\partial V} \nabla \cdot \mathbf{M}(\mathbf{r}') G_i(\mathbf{r}, \mathbf{r}') dS' \right]
 \end{aligned} \tag{A1.25}$$

The first Equation (A1.24) is called the EFIE and the second Equation (A1.25)

Appendix A

is called the MFIE. Both equations give the scattering field (\mathbf{E}_s and \mathbf{H}_s) if the source distributions (\mathbf{J} and \mathbf{M}) are known. They are general valid and widely used in the MoM. In the special case, if a PEC body is under study, no magnetic sources exist, and these two equations can be simplified into the well-known formulations:

$$\begin{aligned} \mathbf{n} \times \mathbf{E}_s(\mathbf{r}) = & \mathbf{n} \times \left[j\omega\mu_i \int_{\partial V} \mathbf{J}(\mathbf{r}') G_i(\mathbf{r}, \mathbf{r}') dS' \right] + \\ & \mathbf{n} \times \left[\frac{1}{j\omega\epsilon_i} \nabla \int_{\partial V} \nabla \cdot \mathbf{J}(\mathbf{r}') G_i(\mathbf{r}, \mathbf{r}') dS' \right], \end{aligned} \quad (\text{A1.26})$$

$$\mathbf{n} \times \mathbf{H}_s(\mathbf{r}) = -\mathbf{n} \times \int_{\partial V} \nabla' G_i(\mathbf{r}, \mathbf{r}') \times \mathbf{J}(\mathbf{r}') dS' + \frac{1}{2} \mathbf{J}(\mathbf{r}) \delta_S(\mathbf{r}). \quad (\text{A1.27})$$

Appendix B

B1 Barycentric Subdivision

The numerical integration over a source region in the MoM requires a suitable segmentations of the basis function. The Barycentric subdivision [Mak02, Kam98] is a simple technique to generate nine sampling points ($\mathbf{r}_1, \dots, \mathbf{r}_9$) for the numerical evaluation of the integral equations. This technique is applied typically for the integration over a scalar function, e.g., the Green's function $G(\mathbf{r}, \mathbf{r}')$ of the free space, as explained for the EFIE in Chapter 2.1.

All three corners of the triangular patch are divided with the factor 3 and connected into equal sub-triangles, as sketched in Fig. B1-1. Each of the nine triangles have the same area A_i , which is:

$$A_i = \frac{1}{9} A, \tag{B1.1}$$

where A is the total area of the triangle.

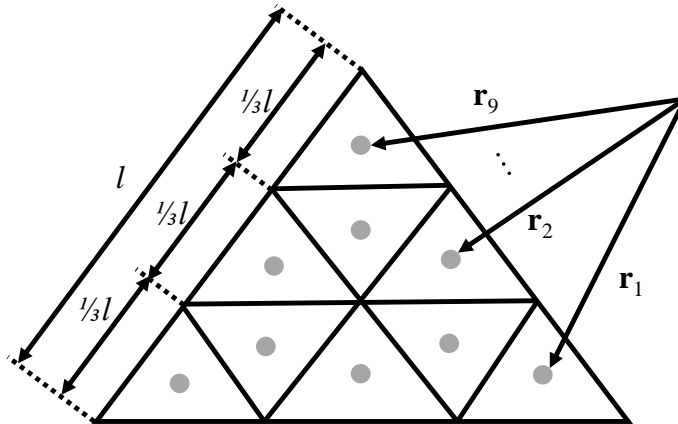


Fig. B1-1 Division of a triangular patch into nine sampling points (gray points).

Appendix B

The integration over the entire triangular domain is divided now into the integrations over nine sub-triangles. The scalar function $G(\mathbf{r}, \mathbf{r}')$ is assumed to be constant within the sub-triangles. Therefore, the integration can be approximated with

$$\frac{1}{A} \iint_A G(\mathbf{r}, \mathbf{r}') dS' \approx \frac{1}{9} \sum_{i=1}^9 G(\mathbf{r}, \mathbf{r}_i). \quad (\text{B1.2})$$

The same technique can be used to evaluate the gradient of the Green's function, which is required for the MFIE formulation in the MoM.

$$\frac{1}{A} \iint_A \text{grad}'(G(\mathbf{r}, \mathbf{r}')) dS' \approx \frac{1}{9} \sum_{i=1}^9 \text{grad}'(G(\mathbf{r}, \mathbf{r}_i)) \quad (\text{B1.3})$$

The presented technique is not suitable for the numerical evaluation of the integral terms in the presented form. In case of $\mathbf{r} \approx \mathbf{r}'$, the Green's function tends to infinity. Therefore, the use of the numerical technique, in combination with the singularity extraction technique (see Appendix B2 and B3), is recommended.

B2 Singularity Extraction

The singularity extraction technique has been introduced first in [Eib95], and extended in [Yoi03]. The premise of this technique is to extract the singularity from the kernel into a separate term and to integrate analytically over the singularity in an additional step. This technique can be applied on the Green's function, the gradient and the rotation of the Green's function, respectively.

In case of the Green's function of the free space, the singularity is located in the real part of the function:

$$G(\mathbf{r}, \mathbf{r}') = \frac{e^{-jk_0|\mathbf{r}-\mathbf{r}'|}}{4\pi|\mathbf{r}-\mathbf{r}'|} = \frac{\cos(-k_0|\mathbf{r}-\mathbf{r}'|)}{4\pi|\mathbf{r}-\mathbf{r}'|} + j \frac{\sin(-k_0|\mathbf{r}-\mathbf{r}'|)}{4\pi|\mathbf{r}-\mathbf{r}'|}. \quad (\text{B2.1})$$

The imaginary part of (B2.1) converge towards:

$$\lim_{|\mathbf{r}-\mathbf{r}'| \rightarrow 0} j \frac{\sin(-k_0|\mathbf{r}-\mathbf{r}'|)}{4\pi|\mathbf{r}-\mathbf{r}'|} = -\frac{jk_0}{4\pi}. \quad (\text{B2.2})$$

The real part of (B2.1) diverge and the numerical integration becomes difficult. In order to overcome the problem, to integrate over the singularity, the real part of (B2.1) is extended with:

$$\frac{\cos(-k_0|\mathbf{r}-\mathbf{r}'|)}{4\pi|\mathbf{r}-\mathbf{r}'|} = \underbrace{\frac{\cos(-k_0|\mathbf{r}-\mathbf{r}'|) - 1}{4\pi|\mathbf{r}-\mathbf{r}'|}}_{\text{numeric}} + \underbrace{\frac{1}{4\pi|\mathbf{r}-\mathbf{r}'|}}_{\text{analytic}}. \quad (\text{B2.3})$$

The real part of (B2.1) is now separated into two terms. The first term in (B2.3) tends toward zero, if $|\mathbf{r}-\mathbf{r}'| \rightarrow 0$, and can be evaluated with the Barycentric subdivision method as explained in Appendix B1. The second term in (B2.3) can be integrated analytically in closed form with some effort (please see Appendix B3).

Appendix B

The first part in (B2.3) has a discontinuous derivation at $|\mathbf{r}-\mathbf{r}'|=0$ and the numerical integration can be difficult. A smooth differential function is required for the accurate calculation of the result. For that, the basic extraction can be extended with an additional term to:

$$\frac{\cos(-k_0|\mathbf{r}-\mathbf{r}'|)}{4\pi|\mathbf{r}-\mathbf{r}'|} = \underbrace{\frac{\cos(-k_0|\mathbf{r}-\mathbf{r}'|)-1}{4\pi|\mathbf{r}-\mathbf{r}'|} + \frac{k_0^2}{8\pi}|\mathbf{r}-\mathbf{r}'|}_{\text{numeric}} + \underbrace{\frac{1}{4\pi|\mathbf{r}-\mathbf{r}'|} - \frac{k_0^2}{8\pi}|\mathbf{r}-\mathbf{r}'|}_{\text{analytic}} \quad (\text{B2.4})$$

The extended first term in (B2.4) is now continuous and can be evaluated numerically with less effort, with the Barycentric method as explained in Appendix B1. The gradient of the numerical part of (B2.4) is continuous and reveals a smooth derivation, which enable a numerical integration, even for the MFIE formulation in the MoM. The second term of the extended extraction can still be integrated analytical in closed form (please see Appendix B3).

B3 Analytic Integration over the Singularity

The numerical evaluation of the impedance matrix in the MoM requires the analytic integration over the singular terms, as described in Appendix B2. In this section the formulas are summarized for the integration over the singularity, and the gradient of the singularity. More details can be found in, e.g., [Yoi03].

For the calculation of the matrix elements with the EFIE and MFIE, the following integration terms have to be solved analytically:

$$K_1^n = \iint_A R^n dS' \quad (\text{B3.1})$$

$$\mathbf{K}_2^n = \iint_A R^n (\mathbf{r}' - \mathbf{q}) dS' \quad (\text{B3.2})$$

$$\mathbf{K}_3^n = \iint_A \nabla R^n dS', \quad \mathbf{r} \notin A \quad (\text{B3.3})$$

$$\mathbf{K}_4^n = \iint_A \nabla R^n \times (\mathbf{r}' - \mathbf{q}) dS', \quad \mathbf{r} \notin A \quad (\text{B3.4})$$

with

$$R = |\mathbf{r} - \mathbf{r}'|. \quad (\text{B3.5})$$

In the above equations \mathbf{q} is the edge vertex of the triangle with respect to RWG basis function:

$$\mathbf{r}' - \mathbf{q} = \boldsymbol{\rho}^\pm, \quad (\text{B3.6})$$

A is the entire area of the triangle and $n = -1, 1, 3, \dots$

Appendix B

The result of the integration of (B3.1)-(B3.4) can be summarized into the following equations:

$$K_1^n = \begin{cases} \frac{1}{n+2} \sum_{i=1}^3 t_i^0 I_i^n, & w_0 = 0 \\ \frac{1}{n+2} \left(n w_0^2 K_1^{n-2} + \sum_{i=1}^3 t_i^0 I_i^n \right), & w_0 \neq 0 \end{cases} \quad (\text{B3.7})$$

$$\mathbf{K}_2^n = \frac{1}{n+2} \mathbf{I}_m^{n+2} + (\boldsymbol{\rho} - \mathbf{q}) K_1^n \quad (\text{B3.8})$$

$$\mathbf{K}_3^n = n w_0 \mathbf{n} K_1^{n-2} - \frac{w_0}{|w_0|} \mathbf{I}_m^n \quad (\text{B3.9})$$

$$\mathbf{K}_4^n = -(\mathbf{r} - \mathbf{q}) \times \mathbf{K}_3^n \quad (\text{B3.10})$$

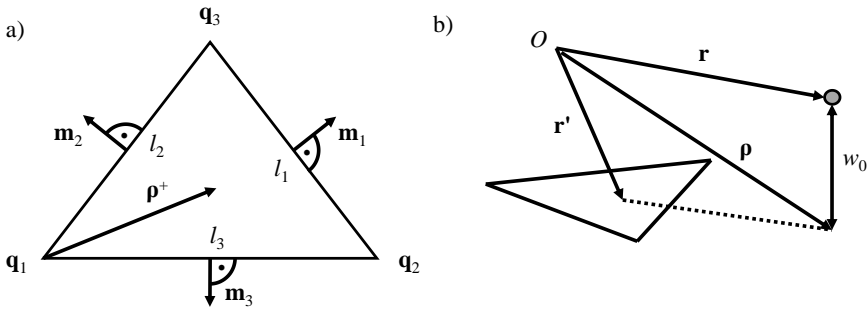


Fig. B3-1 Notations for the analytic integration. A similar figure can be found in [Yoi03].

The solution of the terms in (B3.7)-(B3.10) requires the following results:

$$I_i^{-1} = \ln \left(\frac{R_i^+ + s_i^+}{R_i^- + s_i^-} \right) \quad (\text{B3.11})$$

$$w_0 K_1^{-3} = \begin{cases} 0, & w_0 = 0 \\ \frac{w_0}{|w_0|} \sum_{i=1}^3 \beta_i, & w_0 \neq 0 \end{cases} \quad (\text{B3.12})$$

$$\beta_i = \text{artan} \left(\frac{t_i^0 s_i^+}{(R_i^0)^2 + |w_0| R_i^+} \right) - \text{artan} \left(\frac{t_i^0 s_i^-}{(R_i^0)^2 + |w_0| R_i^-} \right) \quad (\text{B3.13})$$

$$I_i^n = \frac{1}{n+1} \left(s_i^+ (R_i^+)^n - s_i^- (R_i^-)^n + n (R_i^0)^2 I_i^{n-2} \right) \quad (\text{B3.14})$$

$$\mathbf{I}_m^n = \sum_{i=1}^3 \mathbf{m}_i I_i^n \quad (\text{B3.15})$$

With the notation in Fig. B3-1 and the following definitions, a solution for the integral terms can be found.

$$\mathbf{u} = \frac{\mathbf{q}_2 - \mathbf{q}_1}{l_3} \quad (\text{B3.16})$$

$$\mathbf{n} = \frac{(\mathbf{q}_2 - \mathbf{q}_1) \times (\mathbf{q}_3 - \mathbf{q}_2)}{|(\mathbf{q}_2 - \mathbf{q}_1) \times (\mathbf{q}_3 - \mathbf{q}_2)|} \quad (\text{B3.17})$$

$$\mathbf{v} = \mathbf{n} \times \mathbf{u} \quad (\text{B3.18})$$

$$\boldsymbol{\rho} = \mathbf{r} - w_0 \mathbf{n} \quad (\text{B3.19})$$

$$w_0 = (\mathbf{r} - \mathbf{q}_1) \cdot \mathbf{n} \quad (\text{B3.20})$$

$$v_0 = (\mathbf{r} - \mathbf{q}_1) \cdot \mathbf{v} \quad (\text{B3.21})$$

$$u_0 = (\mathbf{r} - \mathbf{q}_1) \cdot \mathbf{u} \quad (\text{B3.22})$$

$$u_3 = (\mathbf{q}_3 - \mathbf{q}_1) \cdot \frac{(\mathbf{q}_2 - \mathbf{q}_1)}{l_3} \quad (\text{B3.23})$$

$$v_3 = \frac{2A}{l_3} \quad (\text{B3.24})$$

$$s_1^- = -\frac{(l_3 - u_0)(l_3 - u_3) + v_0 v_3}{l_1} \quad (\text{B3.25})$$

$$s_2^- = -\frac{u_3(u_3 - u_0) + v_3(v_3 - v_0)}{l_2} \quad (\text{B3.26})$$

$$s_3^- = -u_0 \quad (\text{B3.27})$$

$$s_1^+ = s_1^- + l_1 \quad (\text{B3.28})$$

$$s_2^+ = s_2^- + l_2 \quad (\text{B3.29})$$

$$s_3^+ = s_3^- + l_3 \quad (\text{B3.30})$$

$$t_1^0 = \frac{v_0(u_3 - l_3) + v_3(l_3 - u_0)}{l_1} \quad (\text{B3.31})$$

$$t_2^0 = \frac{u_0 v_3 - v_0 u_3}{l_2} \quad (\text{B3.32})$$

$$t_3^0 = v_0 \quad (\text{B3.33})$$

$$R_1^+ = R_2^- = |\mathbf{r} - \mathbf{q}_3| \quad (\text{B3.34})$$

$$R_2^+ = R_3^- = |\mathbf{r} - \mathbf{q}_1| \quad (\text{B3.35})$$

$$R_3^+ = R_1^- = |\mathbf{r} - \mathbf{q}_2| \quad (\text{B3.36})$$

$$R_i^0 = \sqrt{(l_i^0)^2 + w_0^2} \quad (\text{B3.37})$$

The presented equations give more accurate results of the respective integrals. However, the analytic solution can diverge, if the observation point is on the extension of the edge corners. In this special case, the edge vertices ($\mathbf{q}_1, \mathbf{q}_2, \mathbf{q}_3$) must be permuted.

Appendix C

C1 Matrix Calculation for the EFIE

The matrix calculation with the EFIE requires the testing of the equations with a testing function — in our case the RWG basis function. The following terms are evaluated numerically:

$$\left\langle \mathbf{f}_{\text{RWG},m}, j\omega\mu_i \iint_S \mathbf{f}_{\text{RWG},n} G(\mathbf{r}, \mathbf{r}') dS' \right\rangle, \quad (\text{C1.1})$$

$$\left\langle \mathbf{f}_{\text{RWG},m}, \nabla \frac{1}{j\omega\epsilon_i} \iint_S \nabla \cdot \mathbf{f}_{\text{RWG},n} G(\mathbf{r}, \mathbf{r}') dS' \right\rangle. \quad (\text{C1.2})$$

The first term (C1.1) can be used directly for the numerical evaluation of the integral term in the sense of the MoM. The second term requires a modification for numerical treatment. Using the gradient relation:

$$\iint_S \mathbf{v} \cdot \nabla w dS = \iint_S \nabla \cdot (w\mathbf{v}) dS - \iint_S w \nabla \cdot \mathbf{v} dS, \quad (\text{C1.3})$$

the term (C1.2) can be rewritten into:

$$\begin{aligned} & \left\langle \mathbf{f}_{\text{RWG},m}, \nabla \frac{1}{j\omega\epsilon_i} \iint_S \nabla \cdot \mathbf{f}_{\text{RWG},n} G(\mathbf{r}, \mathbf{r}') dS' \right\rangle = \\ & - \left\langle \nabla \cdot \mathbf{f}_{\text{RWG},m}, \frac{1}{j\omega\epsilon_i} \iint_S \nabla \cdot \mathbf{f}_{\text{RWG},n} G(\mathbf{r}, \mathbf{r}') dS' \right\rangle. \end{aligned} \quad (\text{C1.4})$$

The modified term (C1.4) contains now the divergence of the n -th and m -th RWG basis function, respectively. The term (C1.4) can be evaluated numerically with the aid of the well-known divergence in (3.2).

Substituting the Green's function and the RWG basis function in (C1.1), the

following terms are evaluated:

$$j\omega\mu_i \frac{l_n l_m}{36} \boldsymbol{\rho}_m^\pm \cdot \sum_{u=1}^9 \boldsymbol{\rho}_n^\pm(\mathbf{r}_u) G_i(\mathbf{r}_n^\pm, \mathbf{r}_u) \quad (\text{C1.5})$$

and

$$-\frac{l_n l_m}{j\omega\varepsilon_i 9} (\pm 1) \sum_{u=1}^9 G_i(\mathbf{r}_n^\pm, \mathbf{r}_u) . \quad (\text{C1.6})$$

In (C1.5) and (C1.6) \mathbf{r}_n^\pm is the middle point of the plus and minus triangle, respectively. The sign in (C1.6) depends on the divergence of the n -th and m -th RWG basis function. The sign is positive, if the plus or the minus triangle is used for both the n -th and m -th basis function. If the plus or the minus triangle is used, the sign in (C1.6) is set negative.

As explained in Appendix B, the numerical integration over the Green's function is difficult to evaluate, if the observation and the source point are close to each other. For this, the singularity is extracted and an analytical integration in closed form is used to improve the sampling of the Green's function. With the aid of the Singularity Extraction Method the evaluation of the Green's function becomes:

$$\begin{aligned} \boldsymbol{\rho}_m^\pm \cdot \frac{1}{9} \sum_{u=1}^9 \boldsymbol{\rho}_n^\pm(\mathbf{r}_u) G_i(\mathbf{r}_n^\pm, \mathbf{r}_u) = \\ \boldsymbol{\rho}_m^\pm \cdot \left(\frac{1}{9} \sum_{u=1}^9 \boldsymbol{\rho}_n^\pm(\mathbf{r}_u) \left(\frac{e^{-jk_i R_u} - 1}{4\pi R_u} + \frac{k_i^2}{8\pi} R_u \right) + \frac{1}{A_n^\pm} \iint_{A_n^\pm} \boldsymbol{\rho}_n^\pm \left(\frac{1}{R} - \frac{k_i^2}{8\pi} R \right) dS' \right) \end{aligned} \quad (\text{C1.7})$$

and

$$\begin{aligned} \frac{1}{9} \sum_{u=1}^9 G_i(\mathbf{r}_n^\pm, \mathbf{r}_u) = \\ \frac{1}{9} \sum_{u=1}^9 \left(\frac{e^{-jk_i R_u} - 1}{4\pi R_u} + \frac{k_i^2}{8\pi} R_u \right) + \frac{1}{A_n^\pm} \iint_{A_n^\pm} \left(\frac{1}{R} - \frac{k_i^2}{8\pi} R \right) dS, \end{aligned} \quad (\text{C1.8})$$

with

$$R_u = |\mathbf{r}_n^\pm - \mathbf{r}_u| \quad (\text{C1.9})$$

and

$$R = |\mathbf{r} - \mathbf{r}'|. \quad (\text{C1.10})$$

The derived formulations (C1.7) and (C1.8) are long and complex in evaluation. The calculation time can be reduced significant, if the analytic integration terms are calculated once and the results are used at other frequencies. For that, is required to split the integration terms and to separate the k_i -dependency. This steps can save computation time in a predefine frequency range, but requires more memory.

C2 Matrix Calculation for the MFIE

The matrix calculation for the MFIE requires the same methods (singularity extraction and analytic integration) as it was the case in the EFIE. The main problem arising from the MFIE is the numerical evaluation of the gradient of the Green's function. The numerical integration is more critical and requires a more careful treatment. The extended singularity extraction technique and the analytic solution presented in Appendix B can be used to improve the computation. The following terms are required to be evaluated the MFIE:

$$\left\langle \mathbf{f}_{\text{RWG},m}, -\mathbf{n} \times \iint_S \nabla' G_i(\mathbf{r}, \mathbf{r}') \times \mathbf{f}_{\text{RWG},n} dS' \right\rangle + \frac{1}{2} \langle \mathbf{f}_{\text{RWG},m}, \mathbf{f}_{\text{RWG},n} \rangle. \quad (\text{C2.1})$$

The numerical evaluation of the second part of (C2.1) is obvious, since no Green's function can be found. The integration of this term has to be taken into account, if the source and observation triangle are the same. Otherwise, this term is ignore.

Following the above described procedure in Appendix C1, the first term in (C2.1) can be evaluated with:

$$\begin{aligned} \boldsymbol{\rho}_m^\pm \cdot \mathbf{n} \times \frac{1}{9} \sum_{u=1}^9 \nabla' G_i(\mathbf{r}_n^\pm, \mathbf{r}_u) \times \boldsymbol{\rho}_n^\pm(\mathbf{r}_u) = \\ \boldsymbol{\rho}_m^\pm \cdot \mathbf{n} \times \left(\frac{1}{9} \sum_{u=1}^9 \nabla' \left(\frac{e^{-jk_i R_u} - 1}{4\pi R_u} + \frac{k_i^2}{8\pi} R_u \right) \times \boldsymbol{\rho}_n^\pm(\mathbf{r}_u) \right) + \\ \boldsymbol{\rho}_m^\pm \cdot \mathbf{n} \times \frac{1}{A_n^\pm} \iint_{A_n^\pm} \nabla' \left(\frac{1}{R} - \frac{k_i^2}{8\pi} R \right) \times \boldsymbol{\rho}_n^\pm dS'. \end{aligned} \quad (\text{C2.2})$$

The solution of the analytical term in (C1.2) is available in Appendix B3.

The gradient of the numerical part in (C1.2) with respect to the source point \mathbf{r}' can be derived analytically. The solution is:

$$\begin{aligned} \nabla' \left(\frac{e^{-jk_i R} - 1}{4\pi R} + \frac{k_i^2}{8\pi} R \right) = \\ (jkR + 1) \frac{e^{-jk_i R}}{4\pi R^2} \frac{|\mathbf{r} - \mathbf{r}'|}{R} - \frac{|\mathbf{r} - \mathbf{r}'|}{4\pi R^3} - \frac{k_i^2}{8\pi} \frac{|\mathbf{r} - \mathbf{r}'|}{R}. \end{aligned} \quad (\text{C2.3})$$

The derivation of the term in (C1.3) with respect to the observation point \mathbf{r} is similar, but contains a negative sign

$$\nabla \cdot \left(\frac{e^{-jk_i R} - 1}{4\pi R} + \frac{k_i^2}{8\pi} R \right) = -\nabla \cdot \left(\frac{e^{-jk_i R} - 1}{4\pi R} + \frac{k_i^2}{8\pi} R \right). \quad (\text{C2.4})$$

C3 Excitation Vector Calculation for the EFIE and MFIE

The excitation vector calculation of the electric and the magnetic field is similar, and can be evaluated without any specific techniques. The integration is a simple summation of the contribution of the plus and minus triangle

$$\langle \mathbf{f}_{\text{RWG},m}, \mathbf{E}_{\text{inc}}(\mathbf{r}) \rangle = \frac{l_m}{2} (\boldsymbol{\rho}_m^+ \cdot \mathbf{E}_{\text{inc}}^+ + \boldsymbol{\rho}_m^- \cdot \mathbf{E}_{\text{inc}}^-), \quad (\text{C3.1})$$

where $\mathbf{E}_{\text{inc}}^+$ and $\mathbf{E}_{\text{inc}}^-$ is the electric field in the center of the plus and minus observation triangle, respectively. The same procedure can be used for the magnetic field \mathbf{H}_{inc} .

The excitation with a concentrated voltage source is more complex, but can be included with less modifications. Following the procedure explained in [Mak03], the impressed electric field across the m -th edge element is

$$\left\langle \mathbf{f}_{\text{RWG},m}, \frac{\mathbf{E}_{\text{Port}}}{\Delta} \right\rangle \Big|_{\Delta \rightarrow 0} = U_{\text{Port}} l_m, \quad (\text{C3.2})$$

where U_{Port} is the voltage across the m -th edge element as denoted in Fig. C3-1.

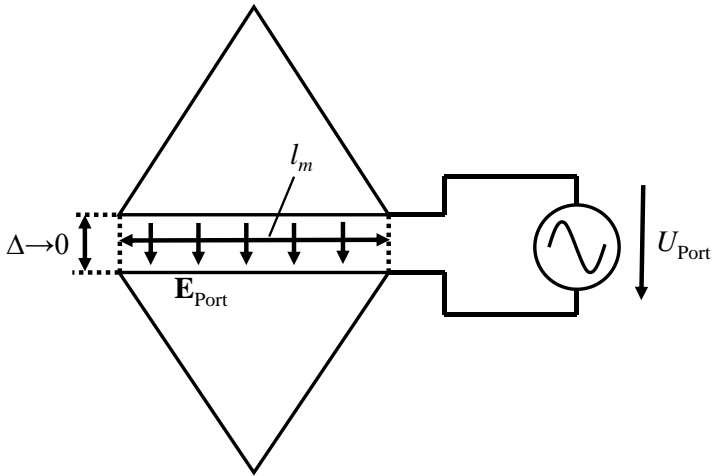


Fig. C3-1 Delta voltage across a RWG basis function. A similar figure can be found in [Mak03].

Bibliography

- [Ada13] J. J. Adams and J. T. Bernhard, "Broadband Equivalent Circuit Models for Antenna Impedances a Fields Using Characteristic Modes," *Antennas and Propagation, IEEE Transactions on*, Volume 61, Issue 8, pp. 3985-3994, August 2013.
- [Ald85] R. T. H. Alden and F. Qureshy, "Eigenvalue Tracking Due to Parameter Variation," *Automatic Control, IEEE Transaction on*, Volume 30, Issue. 9, pp. 923-925, September 1985.
- [Arn51] W. E. Arnoldi, "The Principle of Minimized Iterations in the Solution of the Matrix Eigenvalue Problem," *Quarterly of Applied Mathematics*, Volume 9, Number 17, pp. 17-29, 1951.
- [ARP] ARPACK website [Online] Available: <http://www.caam.rice.edu/software/ARPACK/>
- [Aus98] B. A. Austin and K. P. Murray, "The Application of Characteristic Modes Techniques to Vehicle-Mounted NVIS Antennas," *Antennas and Propagation Magazine, IEEE*, Volume 40, Issue 1, pp. 7-21, February 1998.
- [Bai56] L. L. Bailin and S. Silver, "Exterior Electromagnetic Boundary Value Problems for Spheres and Cones," *Antennas and Propagation, IRE Transaction on*, Volume 4, Issue 1, pp. 5-16, January 1956.
- [Bal89] C. A. Balanis, *Advanced Engineering Electromagnetics*, Hoboken, NJ, USA: Wiley, 1989.
- [Bal05] C. A. Balanis, *Antenna Theory – Analysis and Design*, 3rd ed. Hoboken, NJ, USA: Wiley, 2005.
- [Bjö91] J. Björkberg, "Current Distribution on a Perfectly Conducting Elliptic Disk," *Antennas and Propagation, IEEE Transaction on*, Volume 39, Issue 3, pp. 318-326, March 1991.
- [Bla07] Jean Van Bladel, *Electromagnetic Fields*, second edition, IEEE Press Series on Electromagnetic Wave Theory, John Wiley & Sons, Inc., Publication, 2007.
- [Bow69] J. J. Bowman, T. B. A. Senior, and P. L. E. Uslenghi (ed.), *Electromagnetic and acoustic scattering by simple shapes*, North-Holland Publishing Co., Amsterdam, 1969.

Bibliography

- [Cab07] M. Cabedo, "The Theory of Characteristic Modes Revisited: A Contribution to the Design of Antennas for Modern Applications," *Antennas and Propagation Magazine, IEEE*, Volume 49, Issue 5, pp. 52-68, October 2007.
- [Can91] F. X. Canning, "Protecting EFIE-Based Scattering Computations from Effects of Interior Resonances," *Antennas and Propagation, IEEE Transaction on*, Volume 39, Issue 11, pp. 1545-1552, November 1991.
- [Cap11] M. Capec, P. Hazdra, P. Hamouz, and J. Eichler, "A Method for Tracking Characteristic Modes and Vectors," *Progress In Electromagnetics Research B*, Volume 33, pp. 115-134, 2011.
- [Cha77] Y. Chang and R. F. Harrington, "A Surface Formulation for Characteristic Modes of Material Bodies," *Antennas and Propagation, IEEE Transactions on*, Volume 25, Issue 6, pp. 789-795, November 1977.
- [Cha14] J. Chalas, K. Sertel, and J. L. Volakis, "NVIS Synthesis for Electrical Small Aircraft Using Characteristic Modes," in *2014 IEEE International Symposium on Antennas and Propagation and USNC-URSI National Radio Science Meeting*, Memphis, TN, July 6-12, 2014.
- [Che14a] Y. Chen, R. Martens, R. Valkonen and D. Manteuffel, "A Varactor-Based Tuneable Matching Network for a Non-Resonant Mobile Terminal Antenna," *Antennas and Propagation (EUCAP), 2014, 8th European Conference on*, The Hague, The Netherlands, pp. 2225-2229, 6-11 April, 2014.
- [Che14b] Y. Chen and C.-F. Wang, "Chipboard NVIS Radiation System Design Using the Theory of Characteristic Modes," in *2014 IEEE International Symposium on Antennas and Propagation*, Memphis, TN, pp. 852-853, July 2014.
- [Che15] Yikai Chen and Chao-Fu Wang, *Characteristic Modes – Theory and Applications in Antenna Engineering*, John Wiley & Sons, Inc., Hoboken, New Jersey, USA, 2015.
- [Cri68] J. W. Crispin and K. M. Siegel (eds.), *Methods of radar cross-section analysis*, Academic Press, Inc., New York, 1968.
- [Eib95] T. F. Eibert and V. Hansen, "On the Calculation of Potential Integrals for Linear Source Distribution on Triangular Domain," *Antennas and Propagation, IEEE Transactions on*, Volume 43, Issue 12, pp. 1499-1502, December 1995.
- [EMP] Empire XPU (2015) website [Online] Available: <http://www.empire.de>
- [Erg05] Ö. Ergül and L. Gürel, "Solid-Angle Factor in the Magnetic-Field Integral Equation," *Microwave and Optical Technology Letters*, Volume 45, Issue 5, pp. 452-456, June 2005.
- [Gar65] R. J. Garbacz, "Modal Expansions for Resonance Scattering Phenomena," *Proceedings of the IEEE*, Volume 53, Issue 8, pp. 856-864, August 1965.
- [Gar68] R. J. Garbacz, "A Generalized Expansion for Radiated and Scattered Fields," Ph.D. dissertation, USA, Ohio State University, Columbus, 1968.

- [Gar71] R. J. Garbacz and R. Turpin, "A Generalized Expansion for Radiated and Scattered Fields," *Antennas and Propagation, IEEE Transactions on*, Volume 19, Issue 3, pp. 348-358, May 1971.
- [Gca08] C. Gómez-Calero, L. González, and R. Martínez, "Tri-band Compact Antenna Array for MIMO User Mobile Terminals at GSM 1800 and WLAN Bands," *Microwave Optical Technology Letter*, 2008, Volume 50, No. 7, pp. 1914-1918, July 2008.
- [Had15] T. Hadamik, R. Martens, and D. Manteuffel, "A Design Concept for Massive MIMO Indoor Base Station Using the Theory of Characteristic Modes," *Antennas and Propagation (EUCAP), 2015, 9th European Conference on*, Lisbon, Portugal, 12-17 April, 2015.
- [Har68] R. F. Harrington, *Field Computation by Method of Moments*, New York: Macmillan, 1968.
- [Har71a] R. F. Harrington and J. R. Mautz, "Theory of Characteristic Modes for Conducting Bodies," *Antennas and Propagation, IEEE Transactions on*, Volume 19, Issue 5, pp. 622-628, September 1971.
- [Har71b] R. F. Harrington and J. R. Mautz, "Computation of Characteristic Modes for Conducting Bodies," *Antennas and Propagation, IEEE Transactions on*, Volume 19, Issue 5, pp. 629-639, September 1971.
- [Har72a] R. F. Harrington, J. R. Mautz, and Y. Chang, "Characteristic Modes for Dielectric and Magnetic Bodies," *Antennas and Propagation, IEEE Transactions on*, Volume 20, Issue 2, pp. 194-198, March 1972.
- [Har72b] R. F. Harrington and J. R. Mautz, "Control of Radar Scattering by Reactive Loading," *Antennas and Propagation, IEEE Transactions on*, Volume 20, Issue 4, pp. 446-454, July 1972.
- [Har93] R. F. Harrington, *Field Computation by Method of Moments*, IEEE Press Series on Electromagnetic Waves, 1993.
- [Hel93] M. M. Helaly and H. M. Fahmy, "Combined-Field Integral Equation," *Electronic Letters*, Volume 29, Issue 19, pp. 1678-1679, September 1993.
- [Hu14] Jun Hu, Yu-Ke Li, Z. Nie, and H. Zhao, "Modal Characteristic Basis Function Method for Solving Scattering From Multiple Conducting Bodies of Revolution," *Antennas and Propagation, IEEE Transaction on*, Volume 62, Issue 2, pp. 870-877, February 2014.
- [Jam89] J. R. James and P. S. Hall, *Handbook of Microstrip Antennas*, vol. 1 Exeter, U.K.: Short Run Press Ltd, 1989.
- [Jor04] E. Jorgensen, J. L. Volakis, P. Meincke, and O. Breinbjerg, "Higher Order Hierarchical Legendre Basis Functions for Electromagnetic Modeling," *Antennas and Propagation, IEEE Transaction on*, Volume 52, Issue 11, pp. 2985-2995, November 2004.
- [Kab87a] K. Y. Kabalan, R. F. Harrington, J. R. Mautz, and H. A. Auda, "Characteristic Modes for Slots in a Conducting Plane, TE case," *Antenna and Propagation, IEEE Transaction on*, Volume 35, Issue 2, pp. 162-168, February 1987.

Bibliography

- [Kab87b] K. Y. Kabalan, A. El-Haji, and R. F. Harrington, "Characteristic Modes for Slots in a Conducting Plane, TM case," *Antenna and Propagation, IEEE Transaction on*, Volume 35, Issue 3, pp. 331-335, March 1987.
- [Kal81] R. Kalaba, K. Spingarn, and L. Tesfatsion, "Individual Tracking of an Eigenvalue and Eigenvector of a Parametrized Matrix," *Nonlinear Analysis, Theory, Methods & Applications*, Volume 5, Number 4, pp. 337-340, 1981.
- [Kam98] Y. Kamen and L. Shirman, "Triangle Rendering Using Adaptive Subdivision," *Computer Graphics and Applications, IEEE*, Volume 18, Issue 2, pp. 95-103, March 1998.
- [Kar04] M. Karaboikis, C. Soras, G. Tsachtsiris, and V. Makios, "Compact Dual-Printed Inverted-F Antenna Diversity Systems for Portable Wireless Devices," *Antennas Wireless Propagation Letter, IEEE*, Volume 3, Issue 1, pp. 9-14, December 2004.
- [Kre12] A. Krewski, W. Schroeder, and K. Solbach, "MIMO LTE Antenna Design for Laptops Based on Theory of characteristic Modes," *Antennas and Propagation (EUCAP), 2012, 6th European Conference on*, Prague, Czech Republic, 26-30 March, 2012.
- [Kre14] A. Krewski and W. L. Schroeder, "General Application of Characteristic Mode Equivalent Circuit Models in Antenna Design," *Antennas and Propagation Society International Symposium (APSURSI), 2014 IEEE*, Memphis, USA, 6-11 July, 2014.
- [LAP] LAPACK website [Online] Available: <http://www.netlib.org/lapack/>
- [Led15] R. Ledig (geb. Martens), "Coupling Element Antennas for Small Terminal Based on the Characteristic Modes," Ph.D. dissertation, Germany, University of Kiel, Kiel, 2015.
- [Lud14] D. J. Lüdick, J. v. Tonder, and U. Jakobus, "A Hybrid Tracking Algorithm for Characteristic Modes Analysis," *2014 International Conference on Electromagnetics in Advanced Applications (ICEAA)*, 3-8 August, 2014.
- [Maa08] R. Maaskant, R. Mittra and A. Tijhuis, "Fast Analysis of Large Antenna Arrays Using the Characteristic Basis Function Method and the Adaptive Cross Approximation Algorithm," *Antenna and Propagation, IEEE Transaction on*, Volume 56, Issue 11, pp. 3440-3451, November 2008.
- [Mak02] Sergey N. Makarov, *Antenna and EM Modeling with MATLAB*, Hoboken, N.J., USA: Wiley, 2002.
- [Man01] D. Manteuffel, A. Bahr, D. Heberling, and I. Wolf, "Design Considerations for Integrated Mobile Phone Antennas," *11th International Conference on Antennas and Propagation*, Manchester, UK, 17-20 April, 2001.
- [Mar11a] R. Martens, E. Safin, and D. Manteuffel, "A Concept for MIMO Antennas on Small Terminal Based on Characteristic Modes," *IWAT 2011 – International Workshop of antennas Technology 2011*, Hong Kong, China, 7-9 March, 2011.

- [Mar11b] R. Martens, E. Safin, and D. Manteuffel, "Selective Excitation of Characteristic Modes on Small Terminals," *Antennas and Propagation (EUCAP), 2011, 5th European Conference on*, Rom, Italy, 11-15 April, 2011.
- [Mar11c] R. Martens, E. Safin, and D. Manteuffel, "Inductive and Capacitive Excitation of the Characteristic Modes of Small Terminal," *LAPC 2011 – Loughborough Antennas and Propagation Conference*, Loughborough University, UK, November 2011.
- [Mar12] R. Martens and D. Manteuffel, "Multiple Antenna Integration in Small Terminals," *In ISAP 2012 – International Symposium on Antennas and Propagation 2012*, Nagoya, Japan, October/November, 2012.
- [Mar14] R. Martens and D. Manteuffel, "Systematic Design Method of a Mobile Multiple Antenna System Using the Theory of Characteristic Modes," *IET Microwaves, Antennas & Propagation*, Volume 8, Issue 12, pp. 887-893, September 2014.
- [MAT] MATLAB (R2015a) website [Online] Available: <http://www.mathworks.de>
- [Mau73] J. R. Mautz and R. F. Harrington, "Modal Analysis of Loaded N-Port Scatters," *Antennas and Propagation, IEEE Transaction on*, Volume 21, Issue 2, pp. 188-199, March 1973.
- [Max10] R. T. Maximov, C. L. Zekios, and G. A. Kyriacou, "MIMO Antenna Design Exploiting the Characteristic Mode Eigenanalysis," *in 32nd ESA Antenna Workshop on Antennas for Space Applications*, Noordwijk, the Netherlands, 5-8 October, 2010.
- [Mie1908] G. Mie, "Beiträge zur Optik trüber Medien, speziell kolloidaler Metallösungen," *Annalen der Physik*, Vierte Folge, Band 25, pp. 25-37, 1908.
- [Mie13] Z. Miers, L. Hui, L. Buon Kiong, "Design of Bandwidth-Enhanced and Multi-band MIMO Antennas Using Characteristic Modes," *Antennas and Wireless Propagation Letters, IEEE*, Volume 12, pp. 1696-1699, November 2013.
- [Mie15] Z. Miers and B. K. Lau, "Wideband Characteristic Mode Tracking Utilizing Far-Field Patterns," *Antennas and Wireless Propagation Letters, IEEE*, Volume 14, pp. 1658-1661, March 2015.
- [Mit08] R. Mittra and K. Du, "Characteristic Basis Function Method for Iteration-Free Solution of Large Method of Moments Problems," *Progress in Electromagnetic Research B*, Volume 6, pp. 307-336, 2008.
- [Mon94] R. K. Mongia and P. Bhartia, "Dielectric Resonator Antennas – A Review and General Design Relations for Resonant Frequency and Bandwidth," *International Journal of Microwave and Millimeter-Wave Computer-Aided Engineering*, Volume 4, Issue 3, pp. 230-247, July 1994.
- [Mur94] K. P. Murray and B. A. Austin, "Synthesis of Vehicular NVIS Radiation Patterns Using the Method of Characteristic Modes," *Microwave Antennas and Propagation, IEEE Proceedings*, Volume 141, Issue 3, pp. 151-154, June 1994.

Bibliography

- [Nai09] N. V. Nair and B. Shanker, "An Accurate and Low-Frequency Stable Discretization Scheme for the Electric Field Integral Equation using the Generalized Method of Moments," *Antennas and Propagation Society International Symposium, APSURSI '09, IEEE*, Charleston, South Carolina, USA, 1-5 June, 2009.
- [New79] E. H. Newman, "Small Antenna Location Synthesis Using Characteristic Modes," *Antennas and Propagation, IEEE Transaction on*, Volume 21, Issue 6, pp. 530-531, July 1979.
- [Ozg07] E. Ozgur and L. Gurel, "Linear-Linear Basis function for MLFMA Solutions of Magnetic-Field and Combined-Field Integral Equations," *Antennas and Propagation, IEEE Transaction on*, Volume 55, Issue 4, pp. 1103-1110, April 2007.
- [Pet90] A. F. Peterson, "The Interior Resonance Problem Associated with Surface Integral Equations of Electromagnetics: Numerical Consequences and a Survey of Remedies," *Electromagnetics*, Volume 10, Issue 3, pp. 293-312, 1990.
- [Pra01] V. S. Prakash and R. Mittra, "Dual-Surface Combined-Field Integral Equation for Three-Dimensional Scattering," *Microwave and Optical Technology Letters*, Volume 29, Issue 5, pp. 293-296, June 2001.
- [Pra03] V. V. S. Prakash and R. Mittra, "Characteristic Basis Function Method: A New Technique for Efficient Solution of Method of Moments Matrix Equation," *Microwave and Optical Technology Letters*, Volume 36, Issue 2, pp. 95-100, January 2003.
- [Rai11] B. D. Raines and R. G. Rojas, "Wideband Tracking of Characteristic Modes," *Antennas and Propagation (EUCAP), 2011, 5th European Conference on*, Rome, Italy, 11-15 April, 2011.
- [Rao80] S. M. Rao, "Electromagnetic Scattering and Radiation of Arbitrary Shaped Surfaces by Triangular Patch Modeling," Ph.D. dissertation, USA, The University of Mississippi, 1980.
- [Rao82] S. M. Rao, D. R. Wilton, and A. W. Glisson, "Electromagnetic Scattering by Surfaces of Arbitrary Shape," *Antennas and Propagation, IEEE Transaction on*, Volume 30, Issue 3, pp. 409-418, May 1982.
- [Rao90] S. M. Rao, D. R. Wilton, and A. W. Glisson, "E-Field, H-Field and Combined Filed Solution for Arbitrary Shaped Three-Dimensional Dielectric Bodies," *Electromagnetics*, Volume 10, Issue 4, pp. 407-421, 1990.
- [Saf12] E. Safin, R. Martens, and D. Manteuffel, "Modal Source Reconstruction Based on Radiated Far-Field for Antenna Design," *Antennas and Propagation (EUCAP), Proceedings of the 6th European Conference on*, Prague, Czech Republic, pp. 1645-1649, 26-30 March 2012.
- [Saf13] E. Safin and D. Manteuffel, "Reconstruction of the Characteristic Modes on an Antenna Based on the Radiated Far Field," *Antennas and Propagation, IEEE Transaction on*, Volume 61, Issue 6, pp. 2964-2971, June 2013.

- [Saf15] E. Safin and D. Manteuffel, "Manipulation of Characteristic Wave Modes by Impedance Loading," *Antennas and Propagation, IEEE Transaction on*, Volume 63, Issue 4, pp. 1756-1764, April 2015.
- [Saf16] E. Safin and D. Manteuffel, "Advanced Eigenvalue Tracking of Characteristic Modes," *Antennas and Propagation, IEEE Transaction on*, Volume 64, Issue 7, pp. 2628-2636, July 2016.
- [Sav96] J. S. Savaga and A. F. Peterson, "Quadrature Rules for Numerical Integration over Triangles and Tetrahedra," *Antenna and Propagation Magazine, IEEE*, Volume 38, Issue 3, June 1996.
- [Sch84] D. H. Schaubert, D. R. Wilton, and A. W. Glisson, "A Tetrahedral Modeling Method for Electromagnetic Scattering by Arbitrary Shaped Inhomogeneous Dielectric Bodies," *Antennas and Propagation, IEEE Transaction on*, Volume 32, Issue 1, pp. 77-85, January 1984.
- [Ser99] L. G. K. Sertel and I. K. Sendur, "On the Choice of Basis Functions to Model Surface Electric Current Densities in Computational Electromagnetics," *Radio Science*, Volume 34, Number 6, pp. 1373-1387, November-December 1999.
- [Shu13] Z. Shuai, Z. Kun, Z. Ying, and S. He, "Adaptive Quad-Element Multi-Wideband Antenna Array for User-Effective LTE MIMO Mobile Terminals," *Antennas and Propagation, IEEE Transactions on*, Volume 61, Issue 8, pp. 4275-4283, August 2013.
- [Uma86] K. Umashankar, A. Taflove, and S. M. Rao, "Electromagnetic Scattering by Arbitrary Shaped Three-Dimensional Homogeneous Lossy Dielectric Objects," *Antennas and Propagation, IEEE Transaction on*, Volume 34, Issue 6, pp. 758-766, June 1986.
- [Vai02] P. Vainikainen, J. Ollikainen, O. Kivekas, and I. Kelder, "Resonator-based analysis of the combination of mobile handset antenna and chassis," *Antennas and Propagation, IEEE Transactions on*, Volume 50, Issue 10, pp. 1433-1444, October 2002.
- [Vol08] C. Volmer, J. Weber, R. Stephan, K. Blau, and M. A. Hein, "An Eigen-Analysis of Compact Antenna Arrays and Its Application to Port Decoupling," *Antennas and Propagation, IEEE Transaction on*, Volume 52, Issue 2, pp. 360-370, February 2008.
- [Wat02] A. M. van de Water, "Integral Equation for Scattering by 3D-objects of Arbitrary Shape," Ph.D. dissertation, Netherlands, Faculteit Elektrotechniek Capaciteitsgroep TTE Leerstoelgebied Elektromagnetisme, Eindhoven, February 2002.
- [Yee73] A. O. Yee and R. J. Garbacz, "Self- and Mutual-Admittance of Wire Antennas in Term of Characteristic Modes," *Antennas and Propagation, IEEE Transactions on*, Volume 21, Issue 6, pp. 868-871, November 1973.
- [YOi03] P. Ylä-Oijala and M. Taskinen, "Calculation of the CFIE Impedance Matrix Elements With RWG and nx RWG Function," *Antennas and Propagation, IEEE Transaction on*, Volume 51, Issue 8, pp. 1837-1846, August 2003.

Bibliography

- [Zha13] S. Zhang, A. A. Glazunov, Z. Ying, and S. He, "Reduction of the Envelope Correlation Coefficient With Improved Total Efficiency for Mobile LTE MIMO Antenna Arrays: Mutual Scattering Mode," *Antennas and Propagation, IEEE Transactions on*, Volume 61, Issue 6, pp. 3280-3291, June 2013.

Curriculum Vitae

Personal Details

Name: Eugen Safin
Date of Birth: 5th December, 1984 in Orenburg (Russia)
Nationality: German

Education

2006 – 2011 Diploma in Electrical Engineering and Information Technology, Kiel University (10 Semester), Germany
2011 – 2016 Ph.D. candidate in the Kiel University, Germany

Additional Qualifications

2012 Winning of the 3rd price in best paper award on the European Conference on Antennas and Propagation (EuCAP 2012), Czech Republic, Prague
2012 Participate the ESoA (European School of Antennas) course (Advanced Mathematics for Antenna Analysis), Croatia, Dubrovnik, 12-17 May
2013 STSM (Short Term Scientific Mission) of one week with the Technical University of Prague, Czech Republic, Prague, 7-11 January

